Slow-to-Fast Deformation in Mafic Fault Rocks on an Active Low-Angle Normal Fault, Woodlark Rift, SE Papua New Guinea

Marcel Mizera[1], Timothy Little[2], Carolyn Boulton[2], David John Prior[3], Emma Jane Watson[4], James B. Biemiller[5], Joseph White[6], and Norio Shigematsu[7]

[1]Utrecht University
[2]Victoria University of Wellington
[3]University of Otago
[4]GNS Science
[5]University of Texas at Austin
[6]University of New Brunswick
[7]Geological Survey of Japan, National Institute of Advanced Industrial Science and Technology

November 25, 2022

Abstract

Slip on the active Mai'iu low-angle normal fault in Papua New Guinea that dips 15–24° at the surface has exhumed in its footwall a single, continuous fault surface across a >25 km-wide dome. Derived from a metabasaltic protolith, the fault zone consists of a [?]3 m-thick zone of gouges and cataclasites that overprint a structurally underlying carapace of extensional mylonites. Detailed microstructural and geochemical data, combined with chlorite-based geothermometry, reveal changing deformation processes and conditions in the Mai'iu fault rocks as they were exhumed. The microstructure of non-plastically deformed actinolite grains inherited from the fine-grained (6–35 μm) basaltic protolith indicate that shearing at depth was controlled by diffusion creep accompanied by grain-boundary sliding of these grains together with chlorite neo-crystallization at T[?]270–370°C. In a foliated cataclasite unit at shallower crustal levels (T[?]150–270degC), fluid-assisted mass transfer and metasomatic reactions accommodated aseismic, distributed shearing; pseudotachylites and ultracataclasites in the same unit indicate that such creep was punctuated by episodes of seismic slip—after which creep resumed. At the shallowest levels (T[?]150degC), gouges contain abundant saponite, a frictionally weak mineral that promotes creep on the shallowest-dipping ([?]24deg), most poorly oriented part of the Mai'iu fault. Our field, microstructural and geochemical data of freshly exhumed fault rocks support geodetic, seismological, and geomorphic evidence for mixed seismic-to-aseismic slip on this active low-angle normal fault.

Slow-to-Fast Deformation in Mafic Fault Rocks on an Active Low-Angle Normal Fault, Woodlark Rift, SE Papua New Guinea

M. Mizera[1], T. Little[2], C. Boulton[2], D. Prior[3], E. Watson[4], J. Biemiller[5], J. White[6], Norio Shigematsu[7]

[1]Faculty of Geosciences, Utrecht University, Utrecht, The Netherlands.

[2]School of Geography, Environment and Earth Sciences, Victoria University of Wellington, Wellington, New Zealand.

[3]Department of Geology, University of Otago, Dunedin, New Zealand.

[4]GNS Science, Lower Hutt, New Zealand.

[5]Institute for Geophysics, Jackson School of Geosciences, University of Texas at Austin, Austin, Texas, USA.

[6]Department of Earth Sciences, University of New Brunswick, Fredericton, Canada.

[7]Research Institute Eathquake and Volcano Geology, Geological Survey of Japan, AIST

Corresponding author: Marcel Mizera (m.mizera@uu.nl)

Key Points:

- Fault rock microstructures reveal slow-to-fast slip on an active detachment fault that dips 15–24° at the Earth's surface
- Pseudotachylites, foliated cataclasites, and ultracataclasites developed in a zone of mixed mode, seismic-to-aseismic slip behavior
- Frictionally weak saponite in fault gouge promotes slip on the most poorly oriented, surficial part (<24°) of the Mai'iu fault.

Abstract

Slip on the active Mai'iu low-angle normal fault in Papua New Guinea that dips 15–24° at the surface has exhumed in its footwall a single, continuous fault surface across a >25 km-wide dome. Derived from a metabasaltic protolith, the fault zone consists of a <3 m-thick zone of gouges and cataclasites that overprint a structurally underlying carapace of extensional mylonites. Detailed microstructural and geochemical data, combined with chlorite-based geothermometry, reveal changing deformation processes and conditions in the Mai'iu fault rocks as they were exhumed. The microstructure of non-plastically deformed actinolite grains inherited from the fine-grained (6–35 μm) basaltic protolith indicate that shearing at depth was controlled by diffusion creep accompanied by grain-boundary sliding of these grains together with chlorite neo-crystallization at T>270–370°C. In a foliated cataclasite unit at shallower crustal levels (T≈150–270°C), fluid-assisted mass transfer and metasomatic reactions accommodated aseismic, distributed shearing; pseudotachylites and ultracataclasites in the same unit indicate that such creep was punctuated by episodes of seismic slip—after which creep resumed.

At the shallowest levels (T<150°C), gouges contain abundant saponite, a frictionally weak mineral that promotes creep on the shallowest-dipping (≤24°), most poorly oriented part of the Mai'iu fault. Our field, microstructural and geochemical data of freshly exhumed fault rocks support geodetic, seismological, and geomorphic evidence for mixed seismic-to-aseismic slip on this active low-angle normal fault.

1 Introduction

Domal normal faults (or detachments) that today dip <30° are key structures accommodating lithospheric extension in both the continents and oceans. Bounding metamorphic core complexes (MCCs), such faults typically have slip magnitudes of tens of kilometres, sufficient to exhume mid-crustal mylonitic rocks in their footwall that have been derived from below the brittle-ductile transition (BDT; e.g., Whitney et al., 2013; Platt et al., 2015). The current low dip of these faults (<30°) near the Earth's surface appears at odds with conventional fault mechanical theory: Anderson-Byerlee frictional fault mechanics predict that normal faults should initiate and slip at dips of 60–75° and frictionally lock-up at dips <30–45° (e.g., Anderson, 1951; Sibson, 1985; Lister & Davis, 1989; Collettini & Sibson, 2001; Axen, 2004, 2007; Collettini, 2011; Collettini et al., 2019). This expectation is supported by the rarity of moderate-to-large magnitude historic earthquakes attributable to normal faults with dips <30° (Jackson, 1987; Jackson & White, 1989; Abers et al., 1997; Collettini et al., 2019). Yet, a small number of normal faults are active at low angles (dips <30°) as indicated by continuous global positioning system (GPS) data for active faults (e.g., Hreinsdóttir & Bennett, 2009; Wallace et al., 2014), and by the alignment of microseismic foci near active faults to depths of up to ~16 km (e.g., Rigo et al., 1996; Chiaraluce et al., 2007, 2014). This apparent contradiction is known as the low-angle normal fault (LANF) mechanical paradox.

One way to explain slip on a LANF (or other highly misoriented faults) is that the constituent fault rocks acquire a very low frictional resistance as their fabrics and mineralogy evolve in the brittle crust (e.g., Collettini et al., 2009; Smith et al., 2011). Two main hypotheses allowing sliding at low resolved shear stresses have been suggested: (1) fluid overpressure reduces the effective normal stress (Etheridge et al., 1984; Rice, 1992; Sleep & Blanpied, 1992); or (2) weak minerals such as talc, montmorillonite, saponite and other phyllosilicates lower the coefficient of friction to well below "Byerlee" values (μ=0.6–0.85; Byerlee, 1978; Collettini et

al., 2009; Collettini, 2011; Richard et al., 2014). At the onset of grain-scale brittle deformation near the BDT, fluid influx may cause alteration reactions in the protolith rock, leading to the formation of new phyllosilicates or other minerals that are weaker than the original reactant phases (reaction softening; e.g., Wintsch et al., 1995; Wintsch & Yeh, 2013). Such metasomatic reactions together with fluid-assisted diffusive mass transfer (e.g., Rutter & Mainprice, 1979; Rutter, 1983) may promote the development of interconnected networks of weak phases that can reduce the long-term frictional strength of the fault rock to sub-"Byerlee" friction values (textural softening; e.g., Jefferies et al., 2006) leading to mixed frictional-viscous behavior (Bos & Spiers, 2002).

Shear zone weakening may also be promoted by grain-size reduction to activate grain-size-sensitive deformation mechanisms (Warren & Hirth, 2006; Herwegh et al., 2011; Kilian et al., 2011; Bercovici & Ricard, 2012; Montési, 2013; Platt, 2015; Viegas et al., 2016; Stenvall et al., 2019). The latter weakening mechanism can be isochemical, without necessarily requiring presence of a fluid (e.g., Sternvall et al., 2019). A third suggested mechanism for low-angle slip involves rotation of the principal stress axes to "non-Andersonian" orientations to allow slip on an otherwise seemingly misoriented fault; such rotations can arise through a local stress refraction across an interface into a weak fault zone layer (Faulkner et al., 2006; Healy, 2008); or as a result of topographic loads, lateral density variations, and/or horizontal or vertical shear tractions caused by lower crustal flow (e.g., Spencer & Chase, 1989; Yin, 1989 and related comments by Buck, 1990; Westaway, 2005).

Deformational processes operating at different crustal levels along detachment faults are not well understood (e.g., Collettini, 2011; Smith et al., 2011). Most active continental LANFs are concealed beneath a cover of upper plate rocks (Rigo et al., 1996; Chiaraluce et al., 2014), while ancient ones have commonly been overprinted and obscured by post-activity tectonic tilting, chemical alteration, and erosion (e.g., Axen & Bartley, 1997; Axen, 2004; Collettini, 2011; Whitney et al., 2013). The Mai'iu fault in SE Papua New Guinea is a rare exception—it is one of the best preserved of only a handful of known continental LANFs on Earth that are demonstrably active today (e.g., Spencer, 2010). Dip slip on this fault at ~10 mm/yr for the past 3–4 Myrs (Wallace et al., 2014; Webber et al., 2018; Österle, 2019) has exhumed a >29 km width of little-eroded fault surface in its footwall. Along—and immediately beneath—this now abandoned fault surface, freshly exhumed microstructures in the metabasaltic footwall are well-preserved and can be sampled (Little et al., 2019; Mizera et al., 2019). Different types of fault rocks locally crosscut one another, and together they record spatiotemporal changes in the deformation mechanisms accommodating slip as the fault transited through the middle to uppermost crust (Little et al., 2019).

The active Mai'iu fault is an ideal natural laboratory in which to study microstructural and geochemical changes across a wide range of crustal levels. Here, we present data from fault rock samples collected from the exhumed Mai'iu fault. Mostly mafic in bulk composition, the samples comprise pre-extensional non-mylonitic schists (protolith), syn-extensional mylonites, foliated cataclasites, ultracataclasites, and gouges. We combine field observations with mineral phase and elemental composition data of the fault rocks, microstructural imaging and analyses (including grain size and crystallographic-preferred orientation), and chlorite-based estimates of paleotemperatures. By documenting changes in the microstructures and mineralogy of these fault rocks, we derive a syn-exhumational progression of deformation mechanisms and strain rates that accompanied slip on the Mai'iu fault at different structural levels. We also identify processes

(such as metasomatic reactions and grain size reduction) that led to both weakening and transient strengthening of the fault rocks. Our aim is to evaluate: (a) deformation mechanisms accommodating slip on a low-angle normal fault in space and time; and (b) metasomatic changes in the exhuming mafic rocks, in particular those that may have enabled slip on the most highly misoriented part of the fault near the Earth's surface.

2 Tectonic and Geologic Setting of the Mai'iu Fault

The active tectonics of SE Papua New Guinea is governed by the rapid and oblique convergence of the Pacific and Australian plates across an intervening mosaic of microplates (Fig. 1A; Tregoning et al., 1998; Wallace et al., 2004, 2014). The Woodlark-Solomon Sea microplate today rotates counterclockwise at 2–2.7°/Myr relative to the Australian plate about a nearby Euler pole (Wallace et al., 2014). In the active eastern Woodlark Basin, this rotation has resulted in north-south seafloor spreading (Wallace et al., 2004; Eilon et al., 2015). Farther west, the spreading center transitions into a zone of active continental rifting—the Woodlark Rift—which is thought to have initiated at 3.6–8.4 Ma (Fig. 1A; Taylor & Huchon, 2002; Wallace et al., 2014; Cairns et al., 2015).

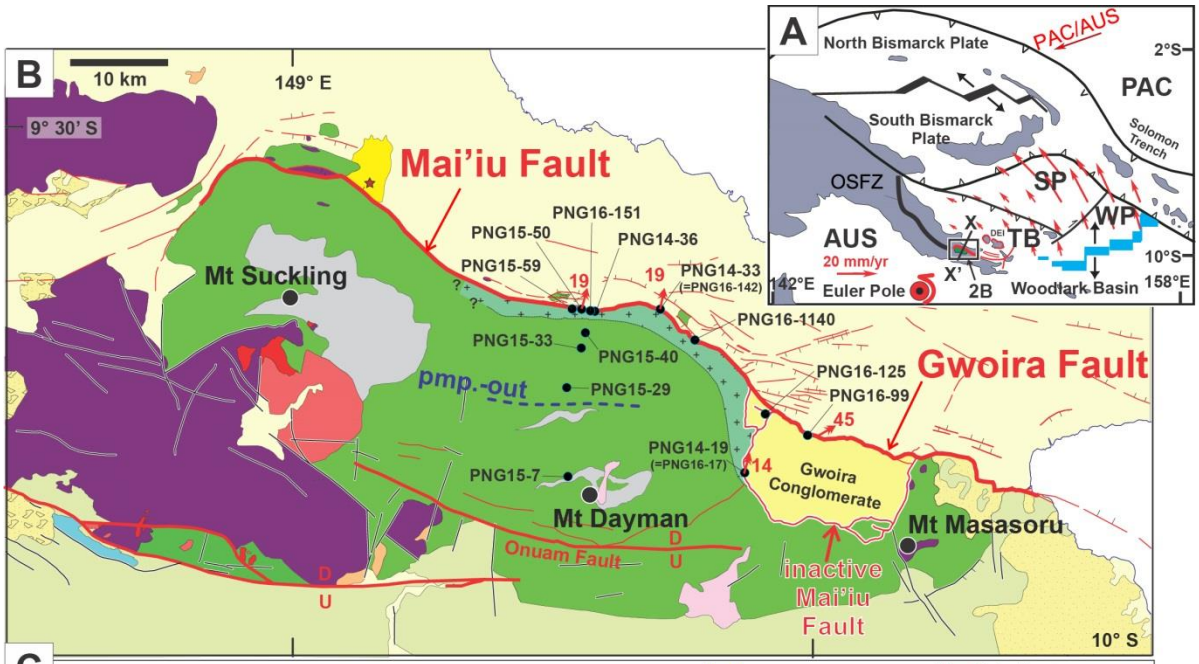
A
North Bismarck Plate
PAC/AUS
2°S
PAC
South Bismarck Plate
Solomon Trench
OSFZ
SP
WP
AUS
20 mm/yr
Euler Pole
TB
10°S
142°E
158°E
Woodlark Basin
X
X'
2B
B
10 km
149° E
9° 30' S
Mai'iu Fault
Mt Suckling
PNG16-151
PNG15-50
PNG14-36
PNG15-59
PNG14-33
(=PNG16-142)
PNG16-1140
PNG15-33
PNG15-40
pmp.-out
PNG15-29
PNG16-125
Gwoira Fault
PNG16-99
45
PNG14-19
(=PNG16-17)
14
Gwoira Conglomerate
PNG15-7
Mt Dayman
Mt Masasoru
Onuam Fault
D
U
inactive Mai'iu Fault
10° S

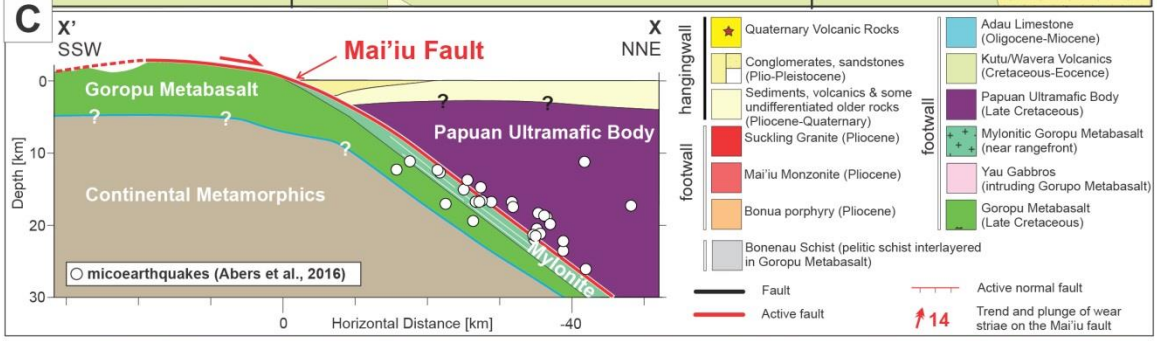
C
X'
SSW
Mai'iu Fault
X
NNE
Goropu Metabasalt
Papuan Ultramafic Body
Continental Metamorphics
Mylonite
micoearthquakes (Abers et al., 2016)
Depth [km]
Horizontal Distance [km]
hangingwall
footwall
Quaternary Volcanic Rocks
Conglomerates, sandstones (Plio-Pleistocene)
Sediments, volcanics & some undifferentiated older rocks (Pliocene-Quaternary)
Suckling Granite (Pliocene)
Mai'iu Monzonite (Pliocene)
Bonua porphyry (Pliocene)
Bonenau Schist (pelitic schist interlayered in Goropu Metabasalt)
Adau Limestone (Oligocene-Miocene)
Kutu/Wavera Volcanics (Cretaceous-Eocence)
Papuan Ultramafic Body (Late Cretaceous)
Mylonitic Goropu Metabasalt (near rangefront)
Yau Gabbros (intruding Gorupo Metabasalt)
Goropu Metabasalt (Late Cretaceous)
Fault
Active fault
Active normal fault
Trend and plunge of wear striae on the Mai'iu fault


D
exhumed fault scarp
active Mai'iu fault trace
~1 km

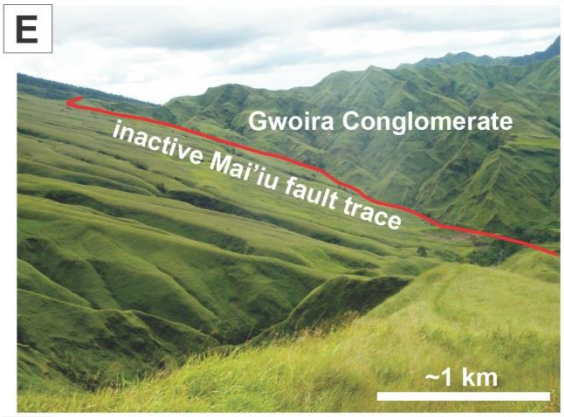
E
Gwoira Conglomerate
inactive Mai'iu fault trace
~1 km


F
exhumed fault surface
50 cm

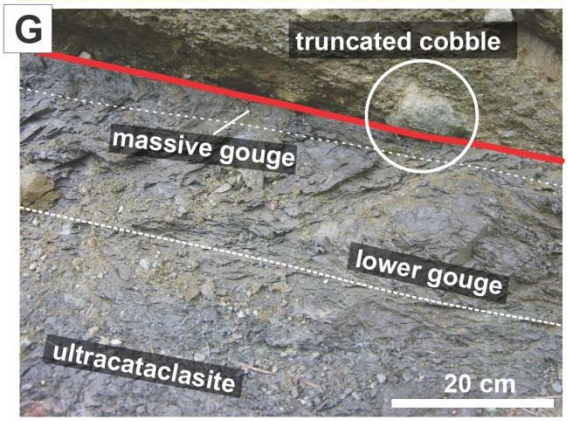
G
truncated cobble
massive gouge
lower gouge
ultracataclasite
20 cm

Figure 1. A) Simplified tectonic map of the Woodlark Rift (after Wallace et al., 2004). Locations of Figure 1B and cross-section X-X' of Figure 1C are shown. B) Geological and structural map of the Suckling-Dayman Metamorphic Core Complex (SDM) with sample locations (after Smith & Davies, 1976; Lindley et al., 2014; Little et al., 2019). C) Tectonic cross-section of the Mai'iu fault (after Daczko et al., 2011; Little et al., 2019). Microearthquake foci are based on Abers et al. (2016). D) Oblique aerial photograph of the active Mai'iu fault rangefront scarp covered in rainforest looking SE. E) Exhumed grassy dip-slopes along the Mai'iu fault where it is inactive and structurally overlain by the Gwoira Conglomerate looking SE. F) Youngest, most recently exhumed surface of the active Mai'iu fault at the base of its scarp. The surface is covered by a dark ~5 cm thick ultracataclasite layer; an overlying soft gouge layer has probably been eroded (site PNG15-50). G) Fault rock sequence of an inactive Mai'iu fault segment preserved beneath the Gwoira Conglomerate (site PNG14-19). Image includes a fault-truncated cobble in the hangingwall (circled). PAC=Pacific plate; AUS=Australian plate; WP=Woodlark plate; SP=Solomon-Sea plate; TB=Trobriand block; DEI=D'Entrecasteaux Islands; OSFZ=Owen-Stanley Fault Zone.

At the southwest margin of the Woodlark Rift (Figs. 1A, 1B), almost all the regional extension is accommodated by slip on the Mai'iu fault. Cosmogenic nuclide studies on the exhumed scarp of this fault indicate a Holocene to present-day dip-slip rate of 11.7±3.5 mm/yr (Webber et al., 2018)—a result that accords with geodetic data indicating a present-day slip-rate of 7.5–9.6 mm/yr (Wallace et al., 2014). The Mai'iu fault is thought to be an extensionally reactivated part of the Owen-Stanley thrust, a major Paleogene thrust fault (Fig. 1A; Davies, 1978; Webb et al., 2008; Daczko et al., 2011; Little et al., 2019). The Owen-Stanley thrust accommodated the southwest-directed obduction of an oceanic and island arc in its upper plate (the Late-Cretaceous Papuan Ultramafic Belt; PUB) over an accreted assemblage of oceanic marginal basin and Australian Plate-derived continental margin rocks (Davies, 1978; Webb et al., 2008; Daczko et al., 2009).

2.1 Geology of the Suckling-Dayman Metamorphic Core Complex

The Mai'iu fault bounds the Suckling-Dayman Metamorphic Core Complex (SDM). The exhumed lower plate of this MCC includes three antiformal culminations that coincide with peaks on the main divide of the Owen Stanley Ranges (Fig. 1B): Mt Suckling (3,576 m), Mt Dayman (2,950 m) and Mt Masasoru (~1,700 m). The footwall of the SDM consists of a >3–4 km thick section of MORB-derived metabasaltic rocks, known as the Goropu Metabasalt, together with minor interbeds of phyllitic metasediments, limestone, and chert, (Smith & Davies, 1976; Österle et al., 2020). The Late Cretaceous metabasalt grades southward into unmetamorphosed equivalents called the Kutu Volcanics, parts of which are Eocene in age (Smith & Davies, 1976). Approximately mid-way up the northern flank of the SDM (Little et al., 2019), a mapped pumpellyite-out isograd probably represents peak temperatures of 350–375°C (Fig. 1B; Beiersdorfer & Day, 1995; Daczko et al., 2009). Farther south, pumpellyite-actinolite facies rocks are exposed as far as the Onuam fault (Fig. 1B), beyond which they transition into prehnite-pumpellyite facies rocks (Davies, 1978) and ultimately the Kutu Volcanics.

Granitoid stocks (e.g., Mai'iu Monzonite, Suckling Granite; Davies & Smith, 1974) intrude the lower plate of the SDM near Mt Suckling and have syn-extensional U-Pb-based zircon crystallisation ages of 1.9–3.7 Ma (Österle et al., 2020). The granitoids record melting of continental crust at depth (Österle et al., 2020). Geophysical surveys (based on seismic travel-times) confirm that the Goropu Metabasalt is underlain by continental crust of felsic to intermediate composition extending to depths of ~32 km near the SDM (Fig. 1C; e.g., Finlayson et al., 1977; Ferris et al., 2006; Eilon et al., 2015; Abers et al., 2016). A relict thrust flap of Papuan Ultramafic Belt (PUB) overlies the Goropu Metabasalt on a southern part of the footwall

of the Mai'iu fault. The PUB is the basement on which the unmetamorphosed alluvial sedimentary rocks of the Gwoira Conglomerate, of Plio-Pleistocene age, were deposited (Fig. 1B; Webber et al., 2020). This latter unit forms much of the hangingwall of the Mai'iu fault, although south of the active Gwoira splay fault, a synformal slice of the Gwoira Conglomerate (former hangingwall rocks) has been captured into the footwall of the SDM (Webber et al., 2020). This slice is floored by a now abandoned, inactive segment of the Mai'iu fault. Outcrops of this inactive segment of the Mai'iu fault provide a complete section through its exhumed fault rocks (Fig. 1B; Little et al., 2019).

Outcrops and dip-slope geomorphic data indicate that the Mai'iu fault dips NNE from 15 to 24° (mostly 20–22°) along its trace at the rangefront (Figs. 1D, 1F; Little et al., 2019; Mizera et al., 2019). Down-dip of this, a linear alignment of microseismicity indicates that the fault steepens to a 30–40° dip in the subsurface below ~12 km depth (Fig. 1C; Abers et al., 2016). Wear striae on the exposed fault surface, including on fault-truncated cobble facets in the hangingwall, trend ~012–015° (Little et al., 2019). The striae are subparallel to the velocity of the Woodlark-Solomon Sea microplate relative to the Australian Plate farther south (Wallace et al., 2014) (Fig. 1A). The striae trend is also subparallel to numerous megacorrugations in the exhumed footwall of the SDM (Spencer, 2010; Daczko et al., 2011; Little et al., 2019; Mizera et al., 2019).

2.2 Fault rock sequence

The immediate footwall of the Mai'iu fault contains a sequence of mostly mafic-composition fault rocks. Figure 2A shows a schematic section of this sequence, which is partly eroded along the active trace of the fault, but fully preserved in outcrops along the inactive segment of the Mai'iu fault (Fig. 1G). The fault sequence includes five units: a) non-mylonitic schist (protolith); b) mylonite; c) foliated cataclasite; d) ultracataclasite; and e) gouge containing the principal displacement surface. Each unit was briefly described in Little et al. (2019), as summarized below:

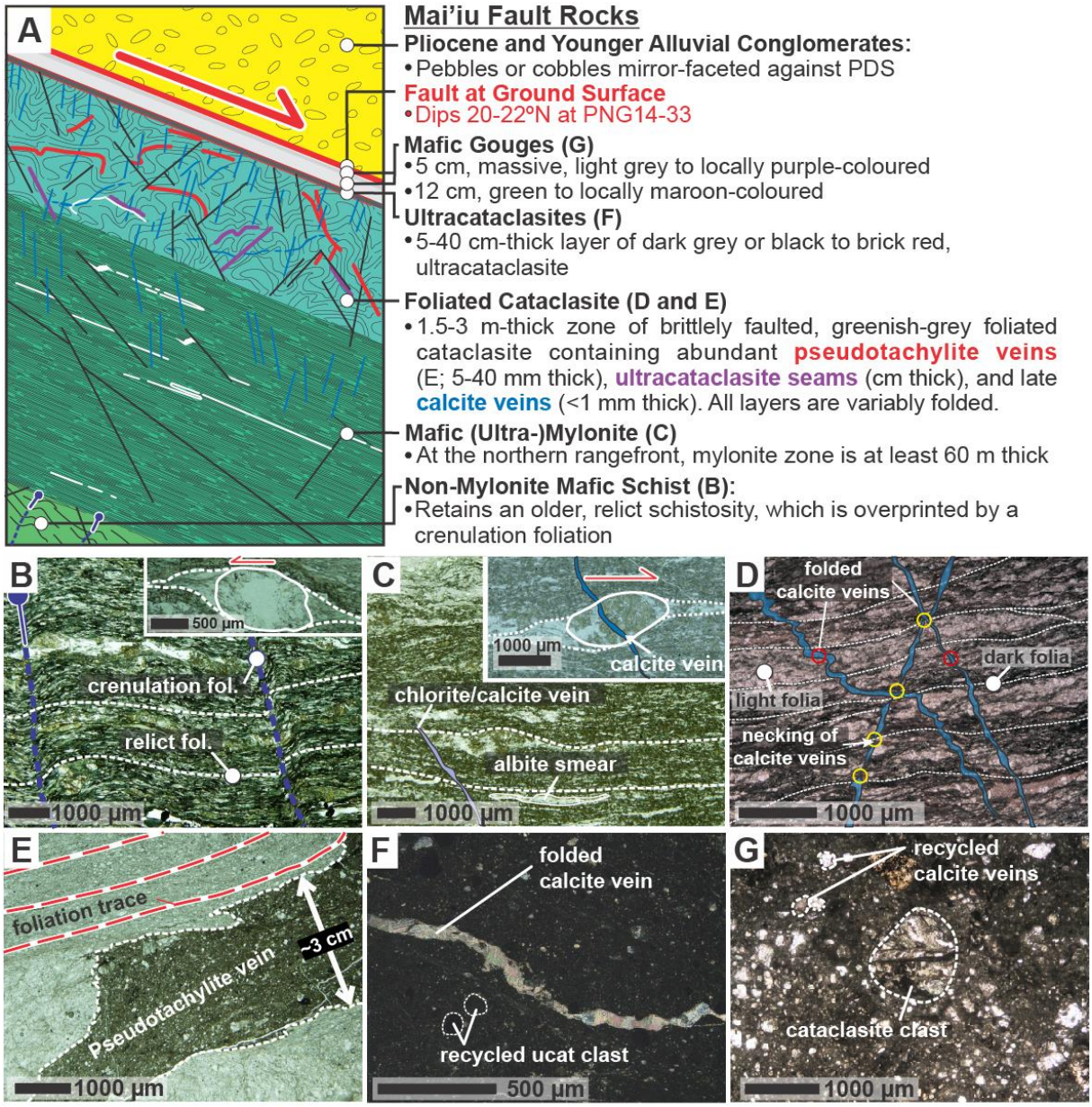

Figure 2. A) Schematic section through the fault rock sequence of the Mai'iu fault based on fully preserved outcrops (modified after Little et al., 2019). B-G) All optical photomicrographs are oriented parallel to the kinematic XZ-direction with down-dip direction to the right. B) Non-mylonitic mafic schist: a spaced crenulation foliation (blue lines) overprints a relict schistosity (white lines; PNG15-7). Inset, asymmetry of strain shadow around epidote porphyroclast indicates top-to-the-SSW shear sense. C) Mafic mylonite: the greenschist facies mineral assemblage defines a LS-tectonite. The rock is cross-cut by several chlorite and calcite veins at a high angle to the foliation. Inset, a strain shadow around an epidote porphyroclast indicates a top-to-the-north (normal) shear sense (PNG14-36). D) Foliated cataclasite: variably deformed calcite veins cross-cut dark and light folia. Note, backward inclined calcite veins (relative to the slip direction) are microfolded (red circles) while forward inclined are necked (yellow circles; PNG16-125B). E) Glassy pseudotachylite vein (~3 cm thick) in a cataclasite sample (PNG14-19). F) Ultracataclasite with folded calcite vein (crossed polarizers; PNG15-50B). Note recycled ultracataclasite (ucat) clasts in the ultrafine-grained matrix. G) Green gouge containing a foliated cataclasite clast and calcite vein fragments (dashed outlines; PNG14-33).

Most of the SDM footwall consists of schistose (non-mylonitic) mafic rocks (Goropu Metabasalt; Fig. 2B) that decrease in metamorphic grade southward (Davies, 1978; Little et al., 2019). On the northern flank of the SDM, greenschist-facies schists contain a fine-grained assemblage of epidote, actinolite, chlorite, albite, titanite, relict clinopyroxene, ±quartz, ±calcite, ±stilpnomelane, ±pyrite, ±mica, ±apatite and ±opaque minerals (Smith & Davies, 1976; Daczko et al, 2009; Little et al., 2019). The mafic schists have a NNW-trending stretching lineation and a top-to-the-SSW (thrust) sense of shear indicated by: (1) asymmetry of strain fringes filled with fibrous quartz ±actinolite or of strain shadows around epidote porphyroclasts filled with blocky chlorite (Fig. 2B, inset); (2) extensional (C') shear bands; and (3) the shape-preferred orientation of actinolite porphyroclasts that have fine-grained, sigmoidal tails of chlorite. These shear fabrics developed during the Paleogene Papuan Orogeny when the Goropu Metabasalt was underthrusted northward beneath the Papuan Ultramafic Belt along the Owen-Stanley thrust (Little et al., 2019).

Extensional mylonitic fabrics are exposed in the footwall within a ~2 km wide band up-dip and to the south of the active fault trace (Fig. 1B). The mylonite unit (mylonites) is at least 60 m-thick along the rangefront; whereas ~2 km up-dip to the south, it narrows to as little as 1.5 m. The mylonites are LS-tectonites with a well-defined NNE-trending stretching lineation and normal-sense shear fabrics (Fig. 2C). Based on pseudosection modelling of the mineral assemblage (epidote, actinolite, chlorite, albite, titanite, ±quartz, ±calcite), the mylonites show peak metamorphic conditions of T=425±50°C and P=5.9–7.2 kbar, reflecting exhumation from ~25±5 km depth (Daczko et al., 2009).

Above the mylonites, a zone of foliated cataclasite, ultracataclasite, and gouge reaching several metres in thickness overprint and rework the mylonites. The foliated cataclasite unit (foliated cataclasites) is 1.5–3 m-thick and hosts multiple generations of pseudotachylite veins (5–40 mm thick; Figs. 2D, 2E). The pseudotachylite matrices are glassy and amorphous in some of the veins, as verified by quantitative X-ray powder diffraction (see Little et al., 2019). More commonly, however, they are devitrified. Five pseudotachylite veins with glassy matrices were dated by $^{40}Ar/^{39}Ar$ geochronology; the derived ages (interpreted as minimum ages for frictional melting) range from 2.24±0.29 Ma to 3.00±0.43 Ma (±2σ; Little et al., 2019).

The foliated cataclasites are structurally overlain by a 5–40 cm-thick dark grey to black (locally brick-red) ultracataclasite unit (ultracataclasite) (Figs. 1F, 2F). Figure 1F shows the smooth top surface of the ultracataclasite. The fault surface is marked by fine wear striae trending NNE. The ultracataclasite is sharply overlain by a gouge unit (gouge) containing one or more layers of incohesive clay-rich gouge that is preserved in inactive fault segment outcrops beneath the Gwoira Conglomerate (Figs. 1B, 1G, 2G; Little et al., 2019). A sharp, planar slip surface (principal displacement surface) places the unmetamorphosed, hangingwall Gwoira Conglomerate against the gouge (Fig. 1G).

3 Methods

3.1 Thin section preparation and analytical methods

The rock samples were collected in 2014, 2015 and 2016 (Fig. 1B; Little et al., 2019). Thin sections were cut parallel to the kinematic XZ-direction—perpendicular to foliation and parallel to mineral lineation or wear striae on the slip surfaces. Fragile fault rocks (e.g., ultracataclasites and gouges) were impregnated with epoxy resin. The mineralogy,

microstructures, and grain sizes of 157 thin-sections were initially described using optical microscopy. From these, we prepared polished thin sections of 47 representative samples for analysis using a field emission gun scanning electron microscope (FEG-SEM) equipped with energy dispersive spectroscopy (EDS), electron backscatter diffraction (EBSD) detectors, and a cold-cathode cathodoluminescence (CL) microscope at the University of Otago. EDS analyses were used to quantify fault rock elemental compositions (see Supporting Information S1 and S2 for detailed EDS maps and descriptions).

Crystallographic orientation data for the phases actinolite, epidote, titanite, albite and quartz were collected by EBSD. The fabric strength of individual phases in the analysed fault rock samples is given by the misorientation index (M-index)—the stronger the fabric, the greater the M-index, which ranges from 0 (random fabric) to 1 (single crystal; Skemer et al., 2005; Mainprice et al., 2015). Estimated mean grain sizes (diameter of a circle with the equivalent area of a given grain, Ø, with errors given at one standard deviation, $\pm 1\sigma$) are based on EBSD-derived phase maps collected in the kinematic XZ plane (two dimensional). The data were collected with 0.4–2 µm step sizes, and processed using the MTEX toolbox for MATLAB (see Supporting Information S3 to S4 for method description, tables with estimated grain sizes and detailed EBSD phase maps). All fault rock images presented are arranged with the normal slip sense of the Mai'iu fault shown top-to-the-right.

In addition, one fault-truncated cobble from the Gwoira Conglomerate with a mirror-like slip surface was subjected to analysis by transmission electron microscope (TEM) at the University of New Brunswick and by SEM with a HITACHI SU-3500 at the Geological Survey of Japan. A further 12 mylonite and foliated cataclasite samples were subjected to electron probe microanalysis (EPMA) at Victoria University of Wellington. A collection of 15 fault rock samples comprising ultracataclasites and gouges were analysed with X-ray powder diffraction (XRD) at the Centre for Australian Forensic Soil Science (CAFSS), in Urrbrae, South Australia (see also Biemiller et al. submitted). Finally, whole rock major element concentrations of four mafic fault rocks including mylonite and gouge were analyzed using X-ray fluorescence (XRF) at the University of Waikato. All these methods are detailed in the Supporting Information S5 to S9.

3.2 Chlorite-based geothermometry

Chlorite is a common mineral in the Mai'iu fault rocks, where it neocrystallized syntectonically in a range of dilational microstructural sites. Although various empirical geothermometers exploit the relationships between the composition and formation temperature of chlorite (see Bourdelle & Cathelineau, 2015), we employ the geothermometer by Cathelineau (1988) because it is best suited to low-grade metamorphic rocks of basaltic composition (e.g., Bevins et al., 1991). This geothermometer is based on the occupancy of $Al^{(IV)}$ in tetrahedral sites of the chlorite structure and was calibrated for mafic rocks from 150–300°C using combined microthermometric data, especially fluid inclusion studies on quartz coexisting with clays (Cathelineau & Nieva, 1985; Cathelineau, 1988).

We obtained chlorite compositions with EPMA from six mylonite and six foliated cataclasite samples (296 measurements; Mizera, 2019). The Windows© program WinCcac by Yavuz et al. (2015) was used to calculate the structural formulae of chlorite based on 14 oxygens and to estimate the formation temperatures by applying the geothermometer of Cathelineau (1988). Because chlorite shows considerable variation in structure at low temperatures, including

the possibility of swelling varieties of trioctahedral structure (mixed-layer clays such as smectite-chlorite), we applied the method by W. Wise as presented in Bettison and Schiffman (1988) to calculate the relative fraction of chlorite to "swelling" component (X), where X=1 represents pure chlorite and X=0 represents pure saponite. Bevins et al. (1991) showed that the Cathelineau (1988) thermometer is applicable for X>0.55.

4 Results: Microstructural Observations and Chlorite Geothermometry of the Mai'iu Fault Rock Sequence

4.1 Microstructural and geochemical analyses

4.1.1 Mylonites

Most mafic mylonites contain a well-dispersed, fine-grained mineral assemblage consisting predominantly of epidote (Ø≈21±13 μm), actinolite (Ø≈17±9 μm), albite (Ø≈18±11 μm), titanite (Ø≈12±4 μm) and chlorite. Porphyroclasts of epidote, actinolite and albite are >50–500 μm in diameter. In comparison, the greenschist-facies non-mylonitic schists (protoliths) have similar grain sizes for epidote (Ø≈21±14 μm), actinolite (Ø≈16±10 μm), albite (Ø≈15±9 μm) and titanite (Ø≈10±5 μm). Unlike the schists, however, the mylonites contain a NNE-trending stretching lineation defined by: a) chlorite strain shadows around epidote porphyroclasts; b) a strong shape-preferred orientation of actinolite and chlorite; and c) smears of albite grains disaggregated from strongly deformed albite-rich veins (Figs. 2C, 3). In addition, the mylonites express a top-to-the-NNE (normal) sense of shear as indicated by extensional C'-shear bands deforming the mylonitic foliation and by the asymmetry of chlorite strain shadows (Fig. 2C, inset). The mylonites are cross-cut by multiple generations of mm-thick chlorite and calcite veins. These are mostly oriented sub-perpendicular to the foliation (Fig. 2C). Less common are mm- to cm-thick veins of albite- and/or quartz that are boudinaged and/or folded within the mylonitic host rock (Figs. 3A, 3D).

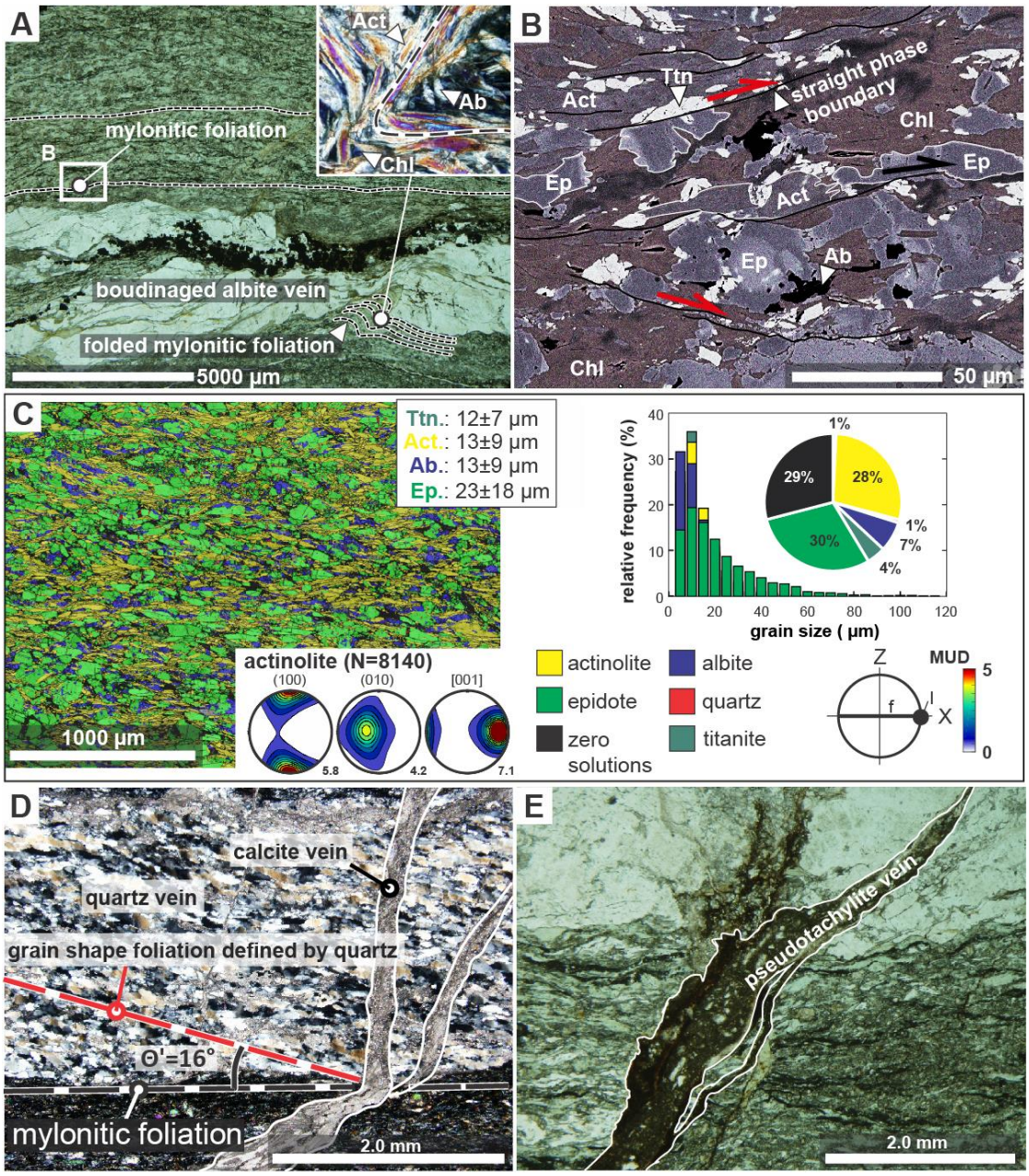

Figure 3. Mafic mylonite samples. A) Optical photomicrograph of a fine-grained mafic mylonite and fragmented boudinaged albite vein (labelled) within the mylonitic host rock (PNG15-59A). Inset, folded mylonitic foliation defined by rotated and fractured actinolite grains. Box denotes area in B. B) Layered elemental image of the mylonite sample in (A) based on EDS analysis. Dark, brick red colors denote chlorite, which we infer to have grown together with the consumption of epidote (purple color) and actinolite (light purple color). Albite grains (black spots) have bulged and irregularly shaped phase boundaries against the other minerals. Thin black lines indicate straight, planar phase boundaries. Grain offsets occur along straight phase boundaries (red arrows). C) Representative EBSD-based phase map, grain-size histogram and phase fraction (%; pie diagram) of mylonite sample PNG16-142C (2 µm step size). Actinolite (100), (010), and [001] pole figures indicate a strong CPO based on one point per grain (N=number of grains). Small numbers next to the pole figures indicate maxima of multiples of uniform distribution (MUD). D) Quartz-rich vein in mylonite PNG16-1BW-E. Elongate quartz grains define a grain-shape foliation oblique (~16°) to the mylonitic foliation with a top-to-the-South (thrust) shear sense. E) Optical photomicrograph of a pseudotachylite vein cross-cutting mylonite PNG15-76.

Epidote, actinolite and titanite are subhedral and variably fragmented or microboudinaged (Figs. 3B, 3C). Fractures and microboudin necks in these minerals are filled with chlorite, ±albite, ±calcite, ±quartz, ±stilpnomelane, and ±iron oxides. Epidote grains show chemical zonation (based on EDS analysis) where the chemistry changes along the rims of these grains, particularly towards crystal tips and fractures (Fig. 3B; Supporting Information Figure S2.1). Actinolite porphyroclasts are fractured along their long axes, in part displaying fracture-parallel dilational offset in the direction of the mylonitic lineation, and/or at a high-angle to it in areas where the mylonitic foliation contains µm- to mm-scale microfolds (Fig. 3A, inset). Albite and chlorite grains infill the dilational saddle reefs of these folded crystals. The fine-grained fractions (6–35 µm) of epidote, actinolite and titanite have straight phase boundaries against another that are sub-parallel to the mylonitic foliation and that can be traced along several grain widths (Fig. 3B). Epidote, actinolite, and titanite grains have been offset along these straight phase boundaries (Fig. 3B). By contrast, albite grains are commonly irregularly curved or bulged along their phase boundaries with the other mafic minerals. Chlorite grains are intergrown with actinolite and epidote grains (Fig. 3B).

EBSD analyses show that actinolite has a strong crystallographic preferred orientation (CPO) in the mylonites (Fig. 3C) with a mean M-index of 0.2±0.1 (1σ). Lower-hemisphere equal area projections (pole figures; parentheses indicate planes (hkl) and square brackets indicate axes [uvw]) show that the long axes of actinolite grains [001] lie sub-parallel to the stretching lineation and fault-slip direction, whereas poles to (010) and (100) planes concentrate sub-parallel to Y and Z, respectively (Fig. 3C). This CPO is weaker in epidote-rich layers (M-index of ~0.09), where fine-grained actinolite grains anastomose around epidote porphyroclasts, and in domains where the mylonitic foliation is microfolded. The strongest actinolite CPOs occur in actinolite-rich layers (M-index of ~0.35). Epidote and titanite in mylonitic samples have random to weak CPOs (M-indices of 0.05–0.06). The weak fabrics in these minerals are defined by a tendency for the poles to (010)-planes to be aligned sub-parallel to the slip-direction, and [001]-axes sub-perpendicular to it. Actinolite, epidote and titanite do not show intragranular microstructures indicative of crystal-plastic deformation (e.g., undulose extinction, subgrain boundaries, deformation lamellae, bulging, etc.). Albite has a random to weak CPO in the matrices of all analyzed fault rocks (Supporting Information S4).

Deformed veins of monophase quartz are usually arranged sub-parallel to the mylonitic foliation (Fig. 3D). Elongated quartz grains within these veins define a grain shape fabric that is oblique to the mylonitic foliation (~16°) and consistently indicate a top-to-the-south (thrust) sense of shear. In the veins, porphyroclastic quartz grains are surrounded by fine, ~5–15 µm-sized quartz grains similar to a “core and mantle” microstructure. Quartz porphyroclasts in these veins have interlobate and bulged grain boundaries at a wavelength similar to the size of the finer quartz grains, suggesting dynamic recrystallization by bulging (e.g., Stipp et al., 2002; Stipp and Kunze, 2008; see also Little et al., 2019).

Mafic mylonites are locally cross-cut by ~0.5–1 mm thick seams of ultrafine-grained (optically irresolvable) rock containing fragments of epidote, albite, quartz, titanite, abundant pyrite and mylonite wall-rock clasts. The seams are mostly discordant to the mylonitic foliation and have strongly indented, intrusive contacts indicating injection (Fig. 3E). We interpret these to be pseudotachylite veins similar to the aforementioned ones hosted by the nearby foliated cataclasite unit.

384 4.1.2 Foliated cataclasites

385 The contact between the mylonites and foliated cataclasites locally coincides with one or
386 more, mm- to cm-thick, anastomosing bands of ultramylonite. The contact zone is also marked
387 by upward increases in the intensity of microfaulting and brecciation and the degree of apparent
388 bleaching of the metabasaltic protolith. The cataclasites contain a mm- to cm-spaced foliation
389 defined by alternating dark- and light-colored folia (Figs. 2D, 4). Darker, phyllosilicate-rich folia
390 anastomose around light-coloured domains and lenticular clasts that consist of albite-rich
391 material. This spaced foliation is distinct from the much finer and more continuous foliation in
392 the mylonites (Figs. 2C, 2D). The spaced foliation is folded at the mm- to cm-scale and is locally
393 cross-cut by (less folded) pseudotachylite veins and abundant, μm- to <1 mm-thick calcite gash
394 veins (Fig. 4A). The calcite veins are typically oriented sub-perpendicular to the foliation.
395 Backward-inclined gash veins (with respect to the sense of shear) are shortened and folded,
396 while forward-inclined ones are stretched and show necking structures (Fig. 2D)—a change in
397 strain type compatible with a normal-sense shearing of the wall rocks. Locally, bands of
398 ultracataclasite cross-cut the folded mylonitic fabric, the calcite veins embedded within it (Fig.
399 4B), and the pseudotachylite veins.

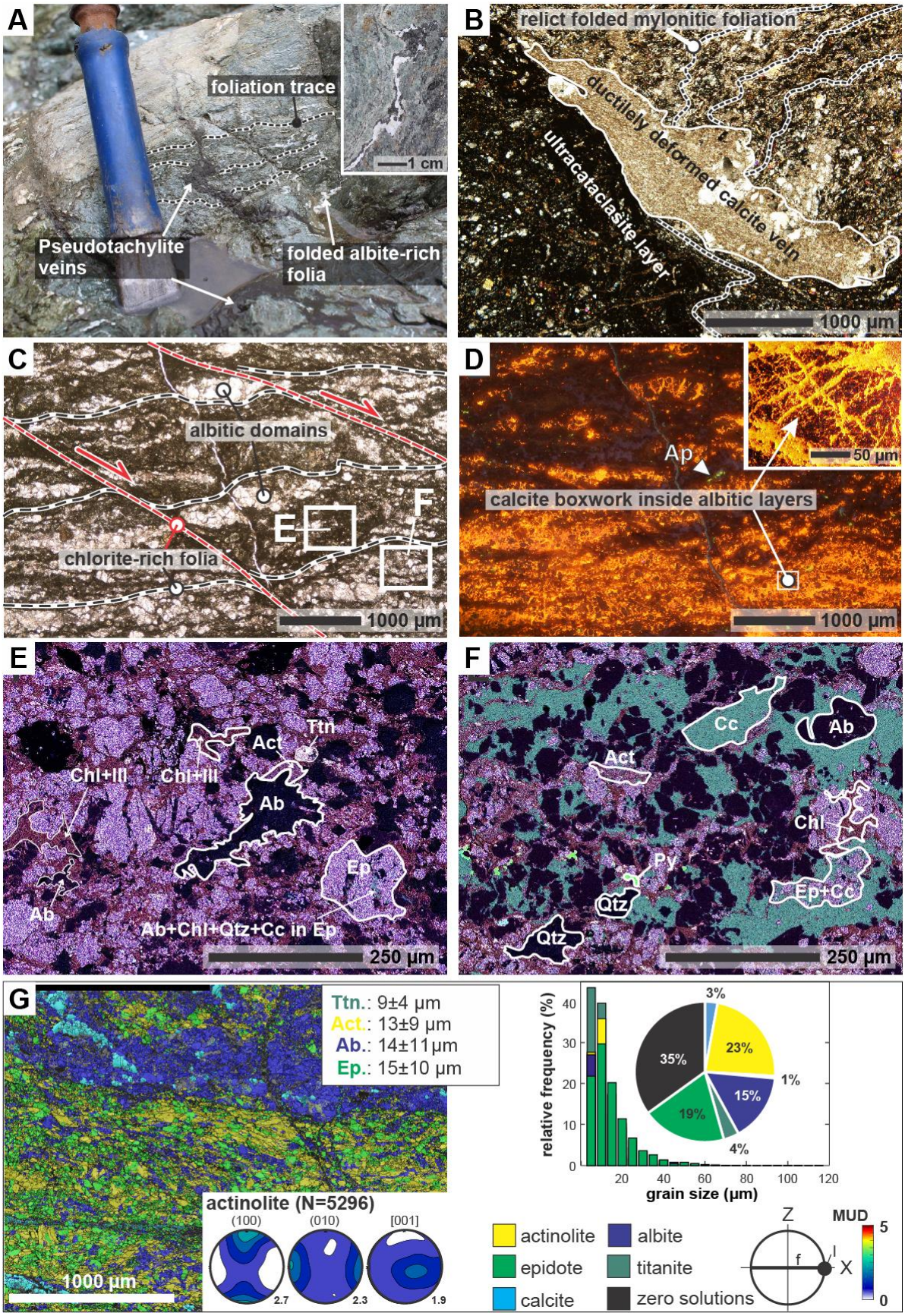
A
foliation trace
1 cm
Pseudotachylite veins
folded albite-rich folia
B
relict folded mylonitic foliation
ductilely deformed calcite vein
ultracataclasite layer
1000 µm
C
albitic domains
E
F
chlorite-rich folia
1000 µm
D
Ap
50 µm
calcite boxwork inside albitic layers
1000 µm
E
Ttn
Act
Chl+Ill
Chl+Ill
Ab
Ep
Ab
Ab+Chl+Qtz+Cc in Ep
250 µm
F
Cc
Ab
Act
Chl
Py
Ep+Cc
Qtz
Qtz
250 µm
G
Ttn.: 9±4 µm
Act.: 13±9 µm
Ab.: 14±11µm
Ep.: 15±10 µm
1000 µm
actinolite (N=5296)
(100)
(010)
[001]
2.7
2.3
1.9
relative frequency (%)
grain size (µm)
3%
23%
1%
15%
4%
19%
35%
actinolite
albite
epidote
titanite
calcite
zero solutions
Z
X
MUD
5
0

400

Figure 4. Foliated cataclasite samples. A) Field photograph of a foliated cataclasite cross-cut by several pseudotachylite veins (dark seams; PNG14-19). Dashed lines indicate foliation trace. Inset, folded calcite and pseudotachylite vein. B) Optical photomicrograph (crossed polarizers) of a foliated cataclasite preserving folded ghosts of the mylonitic foliation (upper right) and ductilely deformed calcite vein (center) cross-cut by an ultracataclasite layer (PNG16-50B). C) Optical photomicrograph of foliated cataclasite PNG16-17D2H. Light layers contain albite, calcite and quartz (Fig. 4F); dark folia (black lines) contain predominantly chlorite±illite, plus minor epidote and actinolite (Fig. 4E). Two dark seams consisting of predominantly chlorite (red line) define an S-C' fabric. D) Optical cathodoluminescence of (C) highlights calcite box-work (orange; inset) inside albite layers. E) Layered elemental image of the dark, chlorite-rich folia in (C) created using EDS analyses. Dark, brick red colors indicate chlorite. We infer that chlorite grew and was passively concentrated during a reaction that consumed epidote (purple color) and actinolite (purple-red color). Epidote is highly fractured and filled with albite, quartz, calcite or chlorite. Relict albite and quartz grains (dark grains) have bulged or irregularly shaped grain boundaries against the other phases. F) Layered elemental image of a light-colored layer in (C) created using EDS analyses. This light layer is dominated by calcite (light green grains) and albite (dark grains). Minor amounts of mafic minerals (epidote, actinolite and chlorite) are also present. G) Representative EBSD-based phase map, grain-size histogram and phase fraction (%; pie diagram) of foliated cataclasite sample PNG16-142E (2 μm step size). Pole figures of (100), (010), and [001] indicate that the CPO of actinolite grains, based on one point per grain (N=number of grains), is weaker than in mylonites and oblique to the kinematic axes. Small numbers next to the pole figures indicate maxima of multiples of uniform distribution (MUD).

Most of the dark folia consist of phyllosilicates (<2 μm in size), with lesser epidote (Ø≈17±9 μm), actinolite (Ø≈12±7 μm) and titanite (Ø≈9±4 μm; Figs. 4C, 4E). EDS and XRD analyses indicate that the phyllosilicates are dominated by chlorite and lesser 1Md and 2M1 illites (Supporting Information S1, S2; also Little et al., 2019). Epidote and actinolite grains typically have indented or truncated phase boundaries in contact with chlorite. Bulging of chlorite inwardly into epidote and actinolite grains suggests growth of chlorite together with dissolution and removal of the neighboring phase (Figs. 4C, 4E). Albite, calcite and quartz are rare in the dark-coloured folia. Where preserved in these folia, the albite grains are either (1) anhedral with interlobate or sutured phase boundaries in contact with the other mafic minerals; or (2) preserved as inclusions inside larger epidote grains together with calcite, quartz and/or chlorite inclusions (Fig. 4E). Based on these observations, we propose the following common mineral reaction responsible for the transformation of epidote and actinolite to chlorite in (sub)greenschist-facies metabasalt (Hashimoto, 1972; Skelton et al., 2000, and references therein):

$$2\ Epidote + 3\ Actinolite + 8\ H_2O + 10\ CO_2 \rightarrow 3\ Chlorite + 14\ Calcite + 21\ Quartz \quad (R.\ 1)$$

If this fluid-driven metasomatic reaction was operative, we would expect calcite and quartz to be formed at the expense of actinolite and epidote.

Indeed, in the light-colored, mm-thick albitic domains, abundant neorecrystallized calcite and quartz occurs in grain-scale dilation sites (Figs. 4C, 4F). Optical cathodoluminescence microphotographs reveal pervasive micro-veining and cementation of the light domains by calcite (Fig. 4D). Albite grains (Ø≈12±9 μm) are usually anhedral, untwinned and cross-cut by either calcite veins or the dark-coloured folia. EPMA analyses of albite porphyroclasts in the mylonite and of albite in the light-coloured foliated cataclasite layers indicate an average composition of An_{05} in both settings, but the albite in the foliated cataclasite shows a wider compositional spread (Fig. 5A).

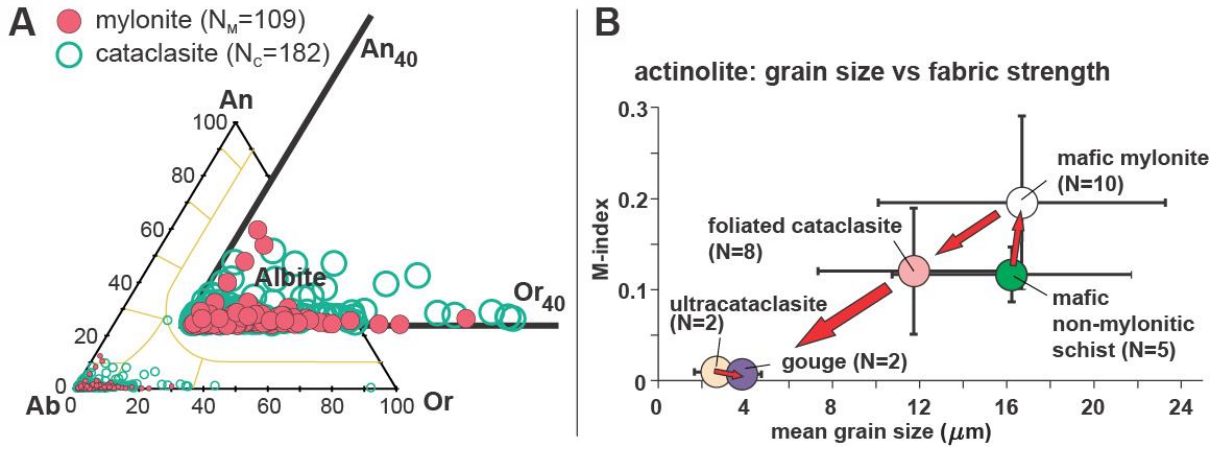

Figure 5. A) Feldspar composition in mafic mylonites and foliated cataclasites. Feldspars are ~95% albite (see also Daczko et al., 2009). B) Grain size vs. M-index plot of actinolite CPOs (averaged values; N=number of samples analysed). The arrowed trend depicts a strong grain-size reduction and weakening of the CPO strength from the mafic mylonites to the foliated cataclasites and ultracataclasites.

Epidote, actinolite and titanite in both the dark and light folia of the foliated cataclasites, show a decrease in grain size, shape preferred orientation and CPO strength relative to the mafic mylonites (Fig. 5B). The average CPO of actinolite in the foliated cataclasites has an M-index of 0.12±0.07 (1σ), compared with an average M-index of 0.2±0.1 (1σ) in the mylonites. While some cataclasite samples have actinolite CPOs similar in strength to mylonites, most are weaker, displaying (010) poles and [001] axes that are diffuse and/or girdled in directions oblique to the kinematic axes (Fig. 4G). Epidote, titanite and albite do not show a CPO in the foliated cataclasites, nor in any of the other overlying fault rocks (M-indices <0.03).

4.1.3 Ultracataclasites

The ultracataclasites are unfoliated and too fine-grained (<2 μm) to be optically resolved in thin section (Fig. 6A). XRD, EDS and EBSD analyses reveal that mafic grains (epidote, actinolite, titanite and albite; all Ø≈2±1 μm), potassium (K-)feldspar, and older (recycled) ultracataclasite lithic fragments are embedded in a much finer-grained (<1 μm), clay-rich matrix (Fig. 6B). Epidote and actinolite porphyroclasts in the ultracataclasite unit are up to 50 μm in diameter, fractured, and show ragged boundaries at the contact with the surrounding clay-rich matrix (Fig. 6E). These epidote and actinolite porphyroclasts are likely to have been reworked from the underlying foliated cataclasite (Fig. 6A).

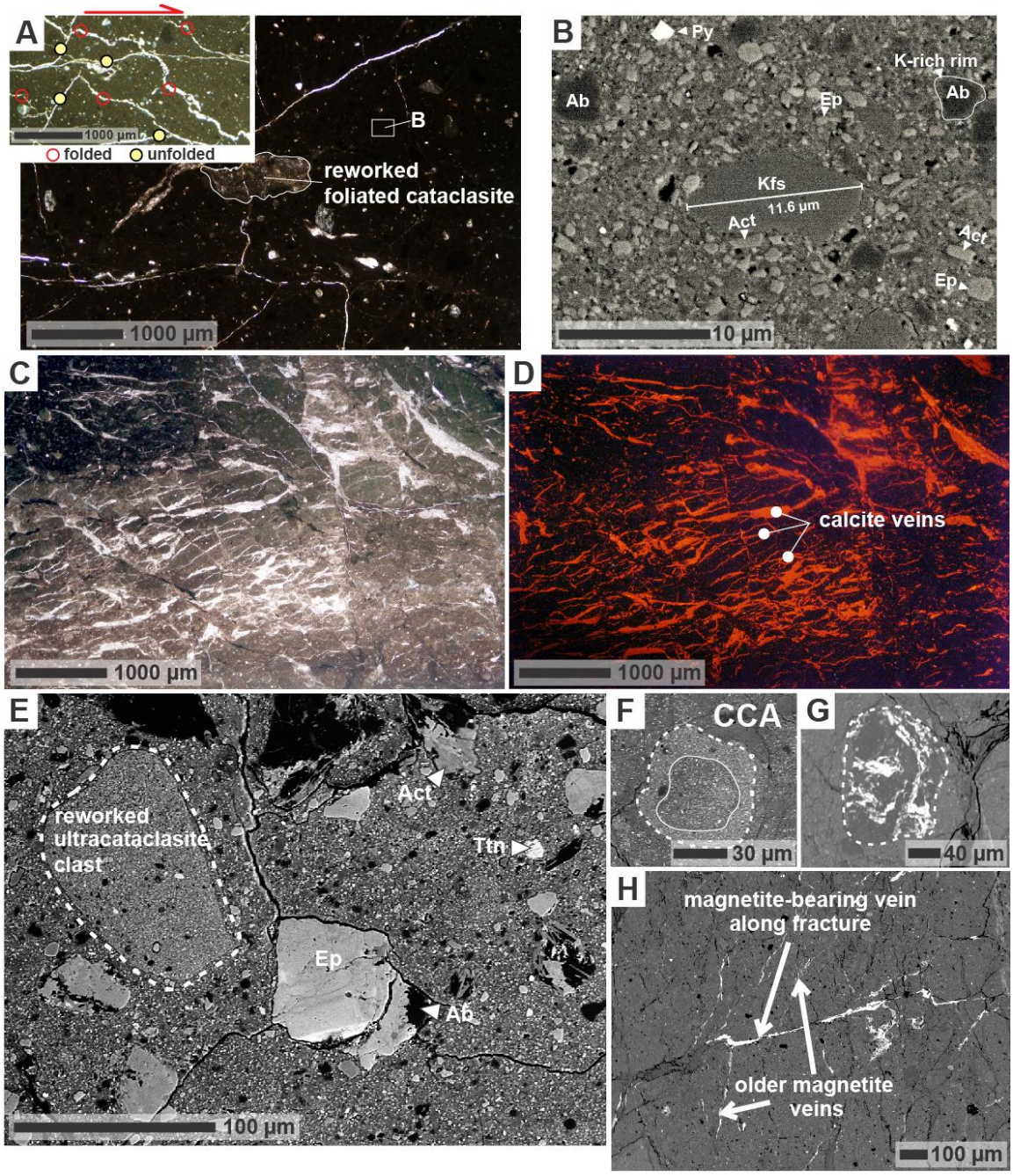

Figure 6. Ultracataclasite samples. A) Optical photomicrograph (plain light) of ultracataclasite sample PNG15-50B. Inset shows microfolding of backward-to-shear-inclined calcite veins (red circles) and necking or lack of folding of forward-inclined veins (yellow circles). B) Backscatter electron image (BSE) of ultracataclasite shown in (A). Note authigenic K-feldspar grain. C) Optical photomicrograph (plain light) of ultracataclasite sample PNG16-142D. Numerous calcite veins (white color) cross-cut the dark-colored, ultrafine-grained clay-rich matrix. D) Optical cathodoluminescence of area in (C) highlights calcite veinlets (orange) cross-cutting the ultracataclasite matrix. E) BSE image of ultracataclasite PNG16-142D. Older ultracataclasite clasts are reworked and show a higher concentration of K relative to the surrounding matrix (Supporting Information Figure S2.4). Mafic mineral clasts are up to 50 µm in diameter. F) BSE image of a clast cortex aggregate (CCA) that occurs locally in ultracataclasite samples (PNG16-142D). G) BSE image of ultracataclasite porphyroclast reworked into younger ultracataclasite PNG16-142D. The fragment contains magnetite-bearing veins (white) swirled into the clast. H) BSE image of mutually cross-cutting magnetite-bearing veins in ultracataclasite PNG16-142D.

Cathodoluminescence microscopy reveals intensive calcite veining in some of the ultracataclasites (Figs. 6C, 6D). Calcite veinlets of <100 μm thickness are mostly unfractured. Instead, they are ductilely deformed in a directionally-dependant manner that resembles calcite veins in the foliated cataclasites. Veinlets that are backwards-inclined with respect to the shear sense are folded, whereas those that are forward-inclined are unfolded and planar (Fig. 6A, inset). This contrasting veinlet geometry suggests that veinlet stress was imposed by normal sense shearing in the weaker, surrounding matrix.

The matrix consists predominantly of corrensite (mixed-layer chlorite-trioctahedral smectite) and/or saponite (trioctahedral smectite; Supporting Information Table S7). The matrix is also enriched in potassium (K-) feldspar relative to the foliated cataclasites and mylonites (Supporting Information Table S1.1). K-feldspar grains are >0.5 μm and up to ~12 μm in diameter, subhedral, unfractured, and in part replace albite (Fig. 6B). The observed increase of K and reduction in Na relative to the underlying foliated cataclasite, and growth of K-feldspar might be related to consumption of albite by the reaction:

$$Albite + K^{+} \rightarrow K\text{-}Fsp + Na^{+}. \quad \text{(R. 2)}$$

We infer that the K-feldspar grains grew authigenically in the ultrafine-grained corrensite- and saponite-rich matrix of the ultracataclasite. The matrix encloses some ultracataclasite clasts that appear to have been derived from other parts of the same unit. The clasts are up to 100 μm in size, rounded and rarely fractured (Fig. 6E), and occasionally coated with an outer cortex (or swirled into the clast) of smectite or magnetite (Figs. 6F, 6G). These inherited fragments of ultracataclasite are generally more K-rich than the surrounding ultracataclasite host rock in which they are embedded (Supporting Information Fig. S2.4).

Some ultracataclasite samples contain distinctive magnetite-bearing clasts and veins (Figs. 6G, 6H). SEM-EDS analysis show that the multiple generations of magnetite-bearing veins (~20–60 μm-thick) cross-cut each other. Some veins contain magnetite ±maghemite grains <1 μm in size (Fig. 6H). Temperature-dependent magnetic susceptibility experiments on one of these ultracataclasite samples exposed just south of the Mai'iu fault trace (Supporting Information S5 for method and results) indicate a magnetic susceptibility of ~13×10^{-6} m^3 kg^{-1} and Curie temperatures between T=580°C and T=645°C for the magnetic fraction of this rock (Fig. 7). These results suggest the presence of cation-deficient magnetite (i.e., magnetite slightly oxidized to maghemite), an inference that also accords with our EDS data (Özdemir & Banerjee, 1984; Dunlop & Özdemir, 1997). Based on the similarity between the heating and cooling curves of the magnetic susceptibility experiment, the Curie temperatures and our EDS analyses, we infer that the principal magnetic mineral in the ultracataclasite is a stable (reversible), single domain (fine grained) magnetite.

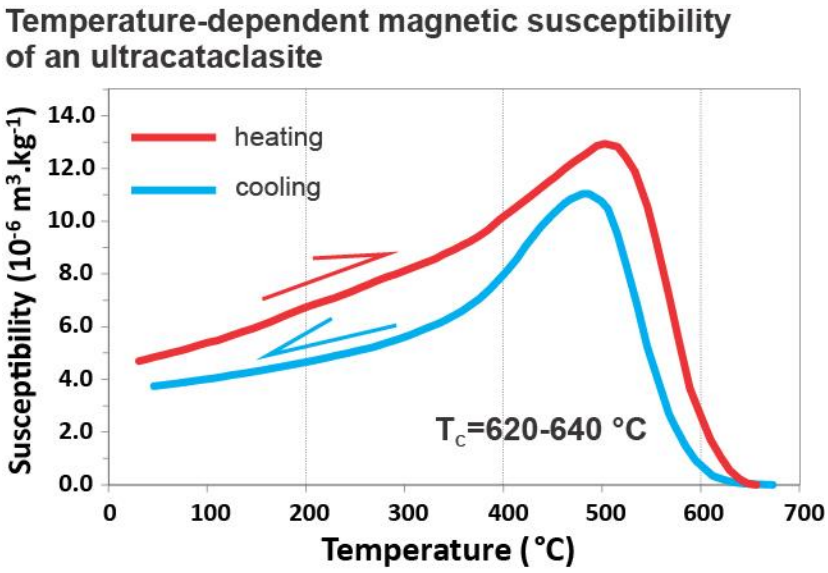

Figure 7. Curves of temperature dependant magnetic susceptibility for ultracataclasite sample PNG16-142D. The red and blue lines denote heating and cooling, respectively, from 40°C to 700°C and vice versa. T_C refers to the Curie temperature. A detailed explanation of the data curves can be found in the Supporting Information S5.

4.1.4 Gouges

In contrast to the underlying fault rock units, all four analysed gouge samples are devoid of calcite veins, although they do contain clasts of calcite or dolomite that were probably reworked from older veins. A foliation is not optically visible in the gouges. The gouge samples contain angular to sub-rounded mono- and polyphase clasts of epidote (Ø≈4±3 µm), actinolite (Ø≈4±3 µm), titanite (Ø≈3±2 µm), and albite (Ø≈3±2 µm), as well as clinopyroxene, quartz and calcite (<2 µm) embedded in a phyllosilicate matrix (Figs. 8A, 8C). Based on XRD and EDS data, the 2 µm fraction of this matrix consists mainly of saponite (Supporting Information Table S7; see also Biemiller et al., submitted). Polyphase clasts are up to 1 cm in diameter and include fragments of mylonite, foliated cataclasite, and fine-grained K-rich fault rocks that resemble the ultracataclasite in texture and composition (Figs. 2G; 8A, 8B, 8D; Supporting Information Tables S1.2, S1.3). Some of the K-rich clasts show an enhanced porosity not seen in the ultracataclasites (Fig. 8D).

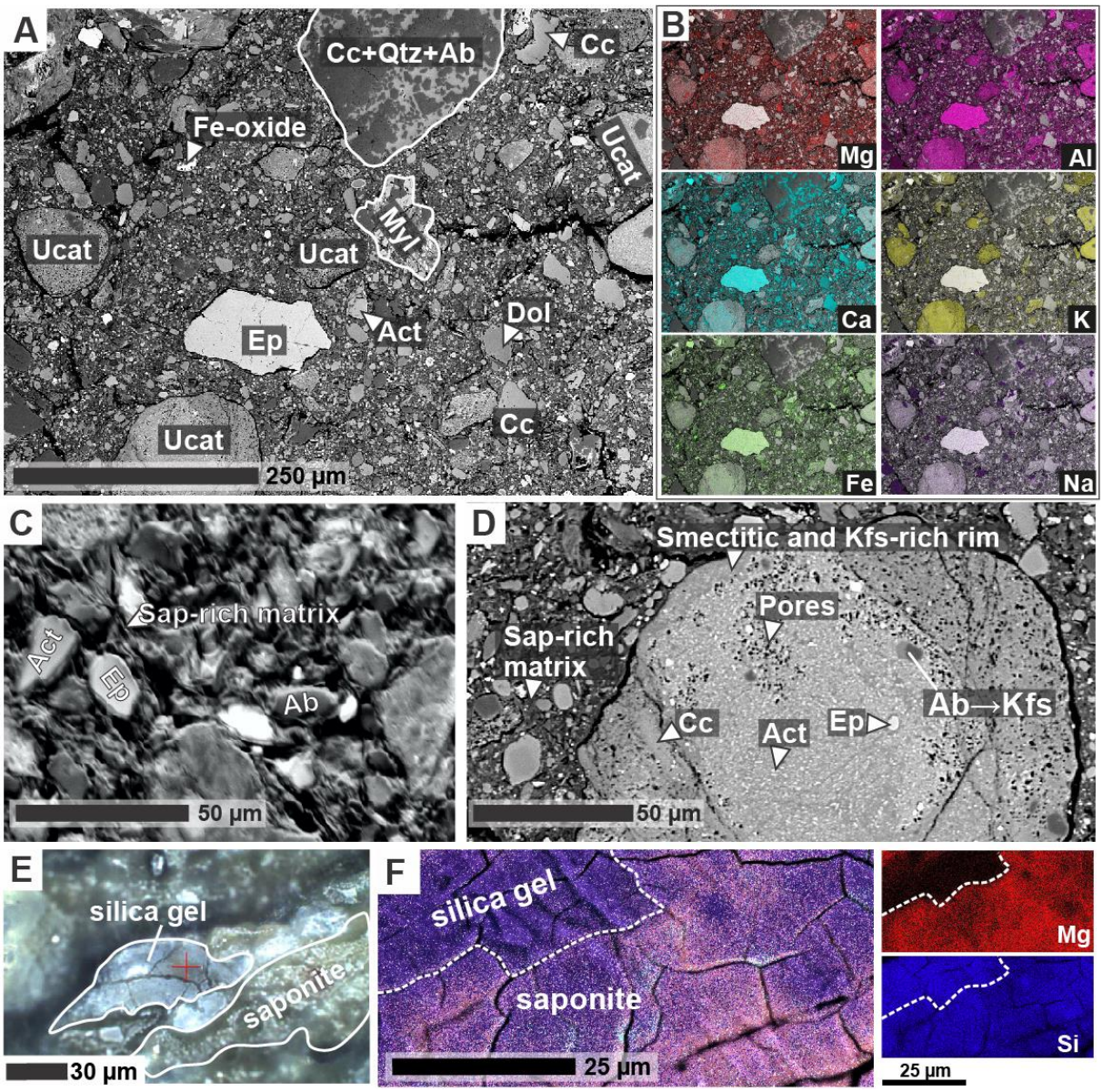

Figure 8. Gouge samples. A) Backscatter electron (BSE) image of gouge sample PNG14-33. This gouge contains reworked fragments of the structurally underlying fault rocks including ultracataclasites (ucat), mylonites (myl) and albitic domains (light colored folia) of the foliated cataclasites. B) Element maps of (E) at reduced scale. The potassium (K) map highlights the K-rich ultracataclasite fragments. The magnesium (Mg) map highlights the saponite-rich gouge matrix . C) Forescatter diode image of the gouge microstructure with mono- and polyphase clasts "floating" in a porous saponite-rich matrix. D) BSE image showing a close-up of a K-rich, porous ultracataclasite clast. The ultracataclasite clast has a smectitic and K-feldspar-rich rim. E) Optical photomicrograph of a silica-rich domain adjacent to saponite (PNG14-19). F) EDS layered elemental map (Si and Mg) highlighting the transition from saponite to the silica-rich domain in PNG14-19.

The gouges contain trace amounts of dolomite and chromite (based on EDS analysis)—two minerals strongly associated with hangingwall ultramafic rocks. Furthermore, XRF analyses show that the gouges contain elevated concentrations of Cr and Ni compared to the mafic schists or mylonites in the footwall of the SDM (Supporting Information Table S8.1). Some gouges contain optically isotropic, tens of µm-thick silica-rich domains or patches (Fig. 8E). Figure 8F show the diffuse nature of the transition from saponite to a silica-rich domain.

These relationships and the proximity of the silica phase to cracks and fractures in the samples suggest that the silica is an alteration product of saponite and/or it has precipitated together with saponite from hydrothermal fluids.

4.1.5 Hangingwall conglomerate and fault faceted cobbles

On the inactive segment of the Mai'iu fault, the principal displacement surface of the Mai'iu fault forms the uppermost contact of the fault rock sequence. This planar, mm-thick contact places unmetamorphosed Gwoira Conglomerate in the hangingwall against the gouges in the footwall. The principal displacement surface truncates cm- to dm-sized clasts in the Gwoira Conglomerate, forming mirror-like facets on those mostly gabbroic clasts. One faceted cobble of dolerite was analyzed by SEM and TEM (Fig. 9). The goal was to describe the composition, thickness and grain-size of the mirror-like surface and its fine striae. The analyzed TEM foil was cut perpendicular to the shiny surface (Fig. 9D).

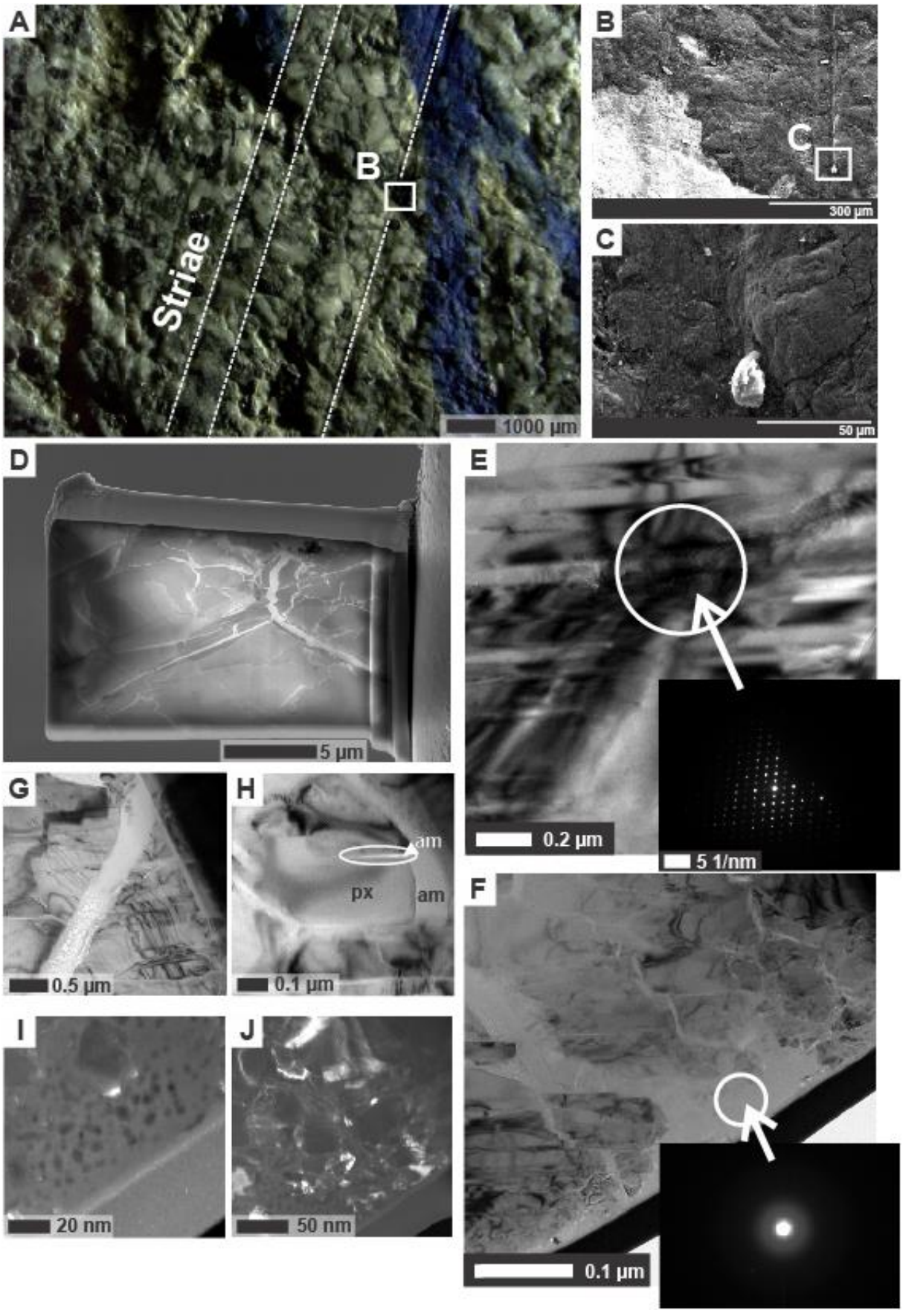
A
Striae
B
1000 µm
B
C
300 µm
C
50 µm
D
5 µm
E
0.2 µm
5 1/nm
F
0.1 µm
G
0.5 µm
H
am
px
am
0.1 µm
I
20 nm
J
50 nm

Figure 9. Gwoira Conglomerate dolerite cobble with nanograin coating. A) Optical photomicrograph (reflected light) of the cobble surface that was truncated by the fault. The surface is abraded by NNE-trending striae. B) Secondary electron image of the striation in (A). C) Close up of (B) showing a groove lineation behind a quartz asperity on a pyroxene grain. D) Focused ion beam (FIB) sample cut perpendicular to the fault (nanograin) surface. Amorphous vein material from the fault surface can be seen cutting across host material. E) TEM brightfield image of host material (pyroxene) comprising lamellae of clino- and orthopyroxene (inset diffraction pattern). F) TEM brightfield image of the shiny surface. Diffraction pattern (inset) illustrates that vein material and the surface are amorphous. G) Cross-cutting amorphous veins in host pyroxene. Beam damage can be seen as holes. H) Veinlet network and amorphous material surrounding, and injected into, a pyroxene grain. I-J) Darkfield TEM images. I) Polished surface of the truncated cobble. Dark spots in the TEM image are holes due to beam damage, suggesting that the amorphous material coating of the mirror surface volatilized under the high voltage current and is hydrous. J) Lower magnification image of (I) demonstrating continuity of the amorphous surface.

Striations on facet surfaces trend subparallel to the inferred NNE slip direction of the fault. Figures 9A–C show the striated surface of the analyzed dolerite including a groove lineation etched into a clinopyroxene-grain by a quartz fragment. The TEM analysis reveals that the mirror surface on the facets is a 2 µm-thick layer of amorphous material mainly consisting of Al and Si (Fig. 9I–F). The TEM images show multiple veins of this amorphous material emanating from the fault-parallel layer and injecting discordantly across host pyroxene grains in the truncated clast (Figs. 9G, 9H).

4.2 Chlorite geothermometry of the fault rocks

More than 100 chlorite grains (270 microprobe measurements) in 12 samples of mylonite and foliated cataclasite from eight localities in the Mai'iu fault zone were analysed. Our analyses targeted chlorite grains infilling syntectonically created microstructural sites, including: (a) in the mylonites, asymmetrical (normal sense) strain shadows and shear bands as well as pulled-apart necks between boudins of epidote and albite; (b) in the foliated cataclasites, dark chlorite-rich folia or C' normal-sense shear bands or ultracataclasite bands; and (c) in both the mylonites and foliated cataclasites, little deformed chlorite veins that cross-cut the foliation and/or pseudotachylite veins. The results of estimated chlorite formation temperatures versus the fraction of chlorite (X=1 is pure chlorite) to "swelling" component (X=0 is saponite) are shown in Figure 10.

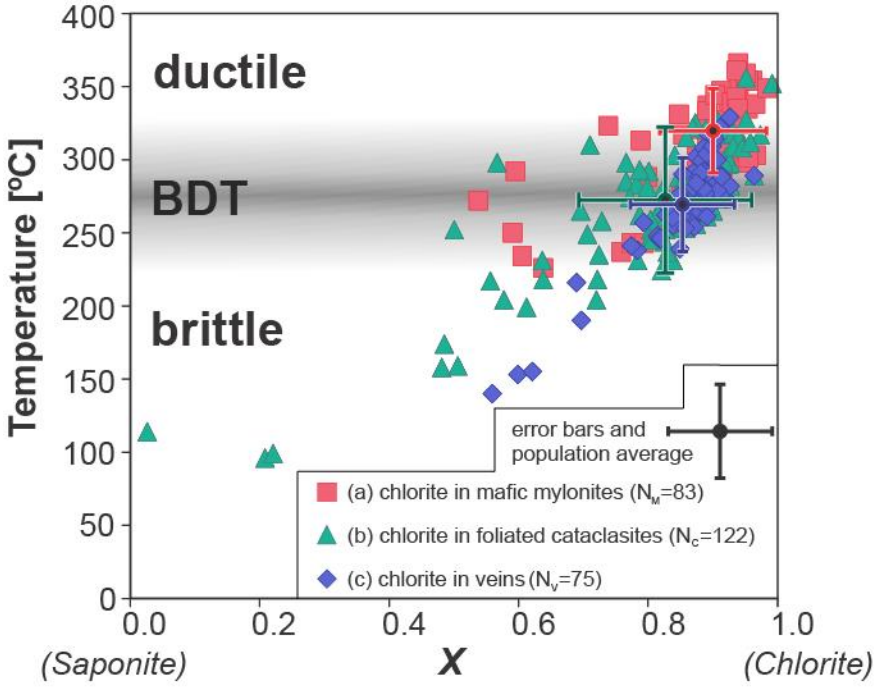

Figure 10. A plot of chlorite formation temperatures (calculated using the geothermometer by Cathelineau, 1988) versus X (the proportion of chlorite to swelling component after the method by Wise; see Bettison & Schiffman, 1988) for syntectonic microstructures in mafic mylonites and foliated cataclasites and chlorite veins cross-cutting these units (see text for explanations). The crosses indicate average values with 1σ error for estimated temperatures and chlorite proportion (X).

Chlorite geothermometry yields temperatures from: (a) 226°C to 366°C with an average of 310±31 °C (1σ) in syntectonic sites in mylonites; (b) 158°C to 356°C with an average of 273±46°C (1σ) in syntectonic sites in foliated cataclasites; and (c) 140°C to 329°C with an average of 270±34°C (1σ) in little-deformed chlorite-filled veins cross-cutting both mylonite and foliated cataclasite. Nearly pure chlorite (clinochlore) is observed in all the mylonite samples (X>0.85), whereas mixed-layer smectite-chlorite to saponite (X<0.50) occurred in the dark folia of some of the foliated cataclasites. Overall there is an increase in "swelling" component (smaller X value) as the calculated temperature decreases. Following the recommendation of Bevins et al. (1991), we excluded the 12 chlorite compositional measurements for which X<0.55 in our calculation of the average chlorite formation temperature for that unit. The shaded area in Figure 10 (labelled "BDT") indicates the overlap between the estimated temperatures in the mylonite samples and the later, cross-cutting chlorite veins.

5 Discussion

5.1 Mai'iu fault structure and fault rock assemblage

The Mai'iu fault exposes mafic mylonitic rocks that have been exhumed from ~25±5 km depth at peak metamorphic conditions of T=425±50 °C and P=5.9–7.2 kbar (based on pseudosection modelling of EPMA mineral chemistry data, Daczko et al., 2009). The late Neogene and younger fabrics in the mylonitic unit were later overprinted in the narrower and structurally overlying <3 m thick fault rock sequence composed of (from bottom to top): foliated cataclasite, ultracataclasite and gouge (Fig. 2). The upper mylonite and adjacent foliated

cataclasite units are cross-cut by several generations of chlorite, calcite and pseudotachylite veins, many of them ductilely deformed (Figs. 2, 3, 4). The brittle fault rocks (ultracataclasites and gouges) have a NNE-trending striation that is parallel to the ductile stretching lineation in the mylonitic rocks, and all fault rock units share the same normal shear sense. The fault rock units become thinner structurally upward, and each unit overprints the underlying one. Together, these observations record a progressive localization of slip that advanced structurally upward in time, and culminated with slip along the sharp and planar principal displacement surface at the base of the unmetamorphosed upper plate.

The estimated chlorite formation temperatures (Fig. 10) decrease from the mylonite (226–366°C) to the foliated cataclasite unit (158–356°C). We relate the wide temperature range of the foliated cataclasite, especially some very high estimated temperatures in that unit, to reflect the largely inherited nature of the mylonitic rock that was reworked into that younger, partially brittle fault rock (Fig. 4B). We interpret the overlap in estimated temperatures between the mylonites and late-stage chlorite veins that cut both it and the foliated cataclasite unit to indicate a temperature range of 226°C to 329°C at the onset of brittle fracturing (Fig. 10). The mineral transformation of chlorite to mixed-layer smectite-chlorite (Fig. 10) and the neoformed corrensite in the ultracataclasite unit indicate sub-greenschist-facies temperatures of ~150–225°C in this fault unit (e.g., Robinson et al., 2002; Surace et al., 2011; Moore et al., 2016). Furthermore, we suggest that saponite in the gouges (XRD data, Supporting Information Table S7.1) was stable at temperatures <150°C (e.g., Lockner et al., 2011; Richard et al., 2014; Boulton et al., 2018). Thus the fault rock sequence and its associated temperatures track a temporal evolution of cooling and embrittlement of the footwall together with progressive localization of brittle slip during exhumation across the BDT and to the Earth's surface.

The Mai'iu fault dips 15–24° along its trace but steepens northward to 30–40° at 12–25 km depth as indicated by a corridor of microseismicity down-dip of it (Abers et al., 2016; Fig. 1C). From these observations, we infer that the Mai'iu fault has a convex-upward geometry not only on the exhumed and abandoned southern part of the fault, but also on the active part of the fault in the subsurface to the north, a curvature that we attribute to operation of rolling hinge-style deformation (Spencer, 1984; Spencer, 2010; Mizera et al., 2019). The convexity, structure, fault rock assemblage, and some deformation mechanisms for the Mai'iu fault resemble those of other continental detachment faults (e.g., Platt et al., 2015; Cooper et al., 2017), but an unusual aspect of the Mai'iu fault is that its footwall rock type is primarily metabasaltic. The next section outlines several deformation mechanisms, both seismic and aseismic, that we infer were active in these mafic rocks as they were exhumed by slip on the Mai'iu fault (Fig. 11).

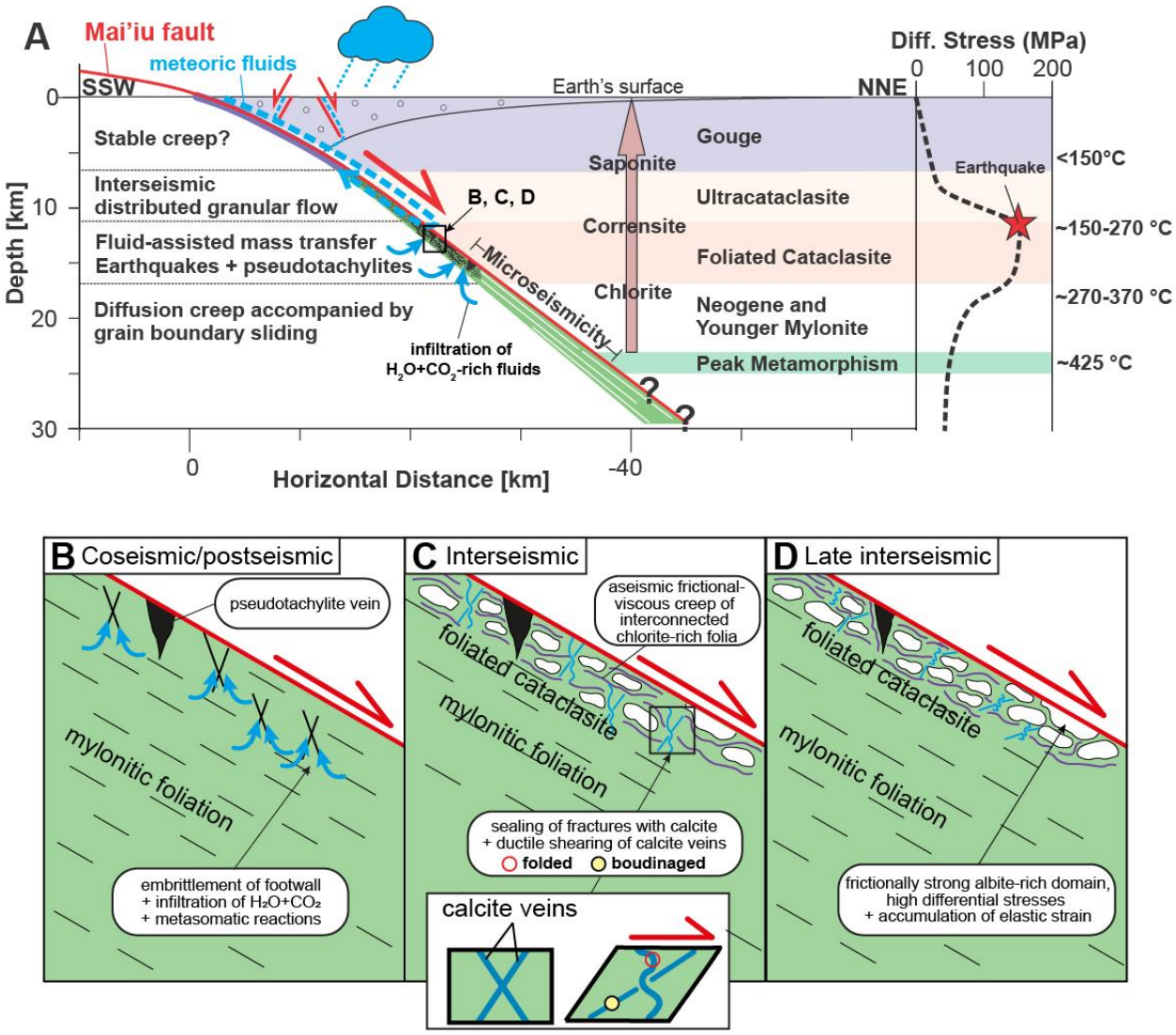

Figure 11. A) Profile across the Mai'iu fault and schematic spatiotemporal changes of deformation mechanisms interpreted in the context of the seismic cycle (e.g., Sibson, 1992). Blue arrows: influx of a chemically active fluid phase (H_2O + CO_2 rich). Mauve arrow with Chlorite, Corrensite, Saponite: Stability and change of these minerals as a function of depth. Microseismicity range is based on Abers et al. (2016). Schematic curve of maximum (static) differential stress versus depth for the Mai'iu fault is based on Mizera (2019). Red star on this strength-curve indicates the depth of dated pseudotachylite veins assuming a dip slip rate of ~10 mm/yr and a convex-upward shaped fault dipping 30–40° at depth. B-D) Schematic evolution of the rheology in the foliated cataclasites, active at a depth range corresponding to T=150 to 270°C, approximately 8 to 15 km. B) Brittle fracturing of the mafic mylonites and/or foliated cataclasites increases the permeability of the fault core, leading to the infiltration of H_2O + CO_2-rich fluids and reaction R1. Short black lines highlight open fractures (Coseismic/postseismic). C) Time-dependent and stress-dependent diffusive mass transfer processes within the foliated cataclasites ultimately lead to the development of interconnected chlorite-rich folia, promoting creep by stable frictional sliding in the chlorite-rich folia. Open fractures are sealed with hydrothermal calcite, and the calcite veins are ductilely sheared during interseismic periods (Interseismic). D) Gradually, precipitation of albite, calcite and quartz from an intergranular fluid phase in fractures and pores cement and strengthen the foliated cataclasites, thus promoting elastic strain accumulation (Late interseismic).

672 ## 5.2 Evolution of deformation mechanisms during shearing of a metabasaltic footwall

673 ### 5.2.1 Late Neogene and younger mylonites, precursor shear zone and fault reactivation

674 We do not observe any evidence for intracrystalline deformation of the primary mineral
675 assemblage (epidote, actinolite, titanite, and albite) of the metabasaltic mylonites. Instead, we
676 observe the following microstructures in these rocks (Fig. 3): (a) an average grain size of 6–35
677 µm; (b) straight phase boundaries between epidote, actinolite and titanite grains and other phases
678 along alignments that span a distance of several grain widths (Fig. 3B); (c) phase-boundary
679 parallel grain offsets (predominantly epidote, actinolite and titanite) along these straight phase
680 boundaries; (d) chemical zonation of epidote grains (Fig. 3B); (e) a strong CPO of non-
681 plastically deformed actinolite grains (Fig. 3C); and (f) a weak to random CPO of albite.

682 From these observations, we infer that shearing in the mylonites was controlled by
683 diffusion creep accompanied by grain-boundary sliding (GBS) (cf. Aspiroz et al., 2007;
684 Getsinger et al., 2013; Elyaszadeh et al., 2018). The strong CPO of actinolite in the mylonites
685 resembles that described for clinoamphiboles in other shear zones of greenschist- to amphibolite-
686 facies metabasites (Aspiroz et al., 2007; Getsinger et al., 2013; Getsinger & Hirth, 2014). These
687 authors attribute strong preferred orientations in amphiboles to diffusion creep accompanied by
688 rigid-body rotation in an otherwise weak (plagioclase-rich), fine-grained matrix. Rigid-body
689 rotation of actinolite in our rocks is consistent with widespread microfolding of the mylonitic
690 foliation and fracturing of acicular actinolite grains (Fig. 3A, inset). Diffusion creep
691 accommodated by anisotropic dissolution and precipitation of amphibole may also contribute to
692 a strong CPO of amphibole (Pearce et al., 2011), and both processes are not mutually exclusive.

693 Based on the fine grain size of the mafic minerals, the strong shape preferred orientation
694 (CPO and SPO) of actinolite, the syntectonic growth of chlorite (secondary phase admixture), we
695 suggest that grain-size-sensitive creep was an important weakening mechanism in the mylonites.
696 The fine grain size and preferred orientation of actinolite increases the cumulative surface area of
697 the grains and decreases mean interparticle distances (e.g., Herwegh et al., 2011 and references
698 therein), both of which would promote rates of diffusion creep. Newly grown interstitial chlorite
699 may have helped to overcome local strain incompatibilities between grains (cf. Behrmann, 1985;
700 Stünitz & Tullis, 2001; Speckbacher et al., 2013) and limit grain growth (Herwegh et al., 2011;
701 Kilian et al., 2011; Menegon et al., 2015).

702 The transition from the precursor, non-mylonitic schist to the overlying Neogene and
703 younger mylonites is marked by: (a) rotation of the stretching lineation from NW to NNE trends
704 (Little et al., 2019); (b) a strengthening of the mafic fabric (especially the increase in CPO of
705 actinolite, Fig. 5B); and (c) a change from top-to-the-south (thrust sense) to top-to-the-north
706 (normal sense) shear fabrics (Figs. 2B, 2C). Both the non-mylonitic schist and the mylonites
707 have similar fine grain sizes (Fig. 5B; Supporting Information Table S4.1 to S4.4) indicating
708 that the footwall of the Mai'iu fault was pre-conditioned for grain size sensitive (GSS) creep
709 prior to the onset of extension when the slip-sense on the fault was reversed. In particular, the
710 Mai'iu fault inherited the pre-existing contrast between these fine-grained mafic rocks in the
711 footwall and the coarse-grained ultramafic rocks (predominantly harzburgite and minor
712 serpentine; Smith & Davies, 1976) of the Papuan Ultramafic Belt in the adjacent hangingwall. At
713 the time of extensional fault inversion, this fault contact dipped >44°, not only at depth but also
714 at the surface, where the oldest hangingwall sediments onlapped against the fault scarp (Mizera
715 et al., 2019; Webber et al., 2020).

Geodynamic models have explored conditions under which a preexisting, failed continental subduction margin may evolve into a domal metamorphic core complex after changes in tectonic boundary conditions (e.g., Biemiller et al., 2019). According to these, extensional inversion is most likely if the precursor thrust is: (1) weak and/or strain softening (see also Lavier et al., 1999; Choi & Buck, 2012; Choi et al., 2013), and (2) originally moderately to steeply dipping (Biemiller et al., 2019). Our observations, together with other data for the Mai'iu fault (Little et al., 2019; Mizera et al., 2019; Webber et al., 2020), converge on a scenario of extensional inversion of the Owen-Stanley thrust shear zone, with slip on that inherited fault zone exhuming the footwall through a rolling-hinge process.

5.2.2 Formation of the foliated cataclasite and implications for a seismic cycle on the Mai'iu fault

The upward transition from mylonites to the foliated cataclasites is marked by: (a) bleaching of the greenschist-facies derived metabasalt (lighter in colour and less mafic than in the mylonites, Figs., 2C, 2D); (b) decreasing mean grain size (Fig. 5B) and increasing intensity of microfaulting and brecciation; (c) development of a mm- to cm-scale spaced foliation defined by alternating albite-rich light and chlorite-rich dark coloured folia (Figs. 2D, 4); (d) strong embayment and truncation of epidote and actinolite against neo-formed chlorite (Fig. 4E); (e) passive concentration and growth of chlorite and subordinate clays in interconnected dark folia; (f) abundant calcite veining and cementation of albite in light-coloured folia (Fig. 4D); (g) CPO weakening and randomization in actinolite (indicated by decreasing M-index; Figs. 4G, 5B); and (h) increasing occurrence and thickness of pseudotachylite veins (Figs. 2E, 4A). These microstructures lead us to infer that the spaced foliation in the foliated cataclasite unit formed during deformation by the coupled fluid-assisted dissolution of epidote and actinolite, mostly in the dark-coloured seams, where it was associated with growth and concentration of chlorite and subordinate clays; and precipitation of albite, calcite and quartz, mostly in the light coloured domains.

One effect of dissolution of epidote and actinolite was bleaching of the foliated cataclasite relative to the mafic mylonite from which it was derived. Although this is a fluid-assisted reaction, we did not find evidence for sustained high pore-fluid pressures in the foliated cataclasites. Emplacement of calcite veins indicate that fluid pressures were at times high enough to induce hydrofracturing (i.e., $P_f > \sigma_3$); however, fluid influx was not high enough to completely retrogress the metabasaltic mineral assemblage as observed in other MCCs such as the Moresby Seamount Detachment in the eastern Woodlark Rift (Speckbacher et al., 2012, 2013). We interpret temporal variations in fluid pressure, the formation and folding of the foliation in the foliated cataclasites, and multiple generation of pseudotachylite veins hosted in these rocks in the context of a seismic cycle-model as explained below (e.g., Sibson, 1992; Scholz, 2002; Figs. 11B-D).

Influx of a chemically active fluid phase (H_2O+CO_2) during embrittlement of the mylonitic rocks (maybe during earthquakes) promoted the dissolution of mafic minerals (coseismic/postseismic period in Fig. 11B). In metasomatic reaction R.1, actinolite and epidote react away, leaving residual chlorite ±illite to accumulate in the dark colored folia. At the same time, the reaction products calcite and quartz were precipitated in dilation sites, particularly within the light-colored folia. Part of the reaction also involved dissolution of albite, diffusion of albite in an intergranular fluid, and re-precipitation of albite in dilation sites, especially in the

light-colored folia together with calcite and quartz. Compositional changes of albite after dissolution and re-precipitation were insignificant (Fig. 5A).

This mass transfer process (mineral transformation, diffusive mass transfer, and re-precipitation) ultimately led to the development of an interconnected chlorite-rich folia in the cataclasites; a case of paired reaction and textural softening (e.g., Stewart et al., 2000; Imber et al., 2001; Moore & Lockner, 2004; Collettini & Holdsworth, 2004; Richard et al., 2014). Aseismic creep, at least temporarily, was facilitated by stable frictional sliding in the chlorite-rich folia (interseismic; Fig. 11C; e.g., Jefferies et al., 2006; Collettini et al., 2009). This is in some ways similar to the pressure solution-accommodated sliding model (frictional-viscous flow) of Bos and Spiers (2002), where minerals are dissolved at sites of stress concentration and re-precipitated in pressure shadows. Natural and experimental observations indicate that the kinetics of diffusive mass transfer is maximized along boundaries between phyllosilicates and more soluble phases (Niemeijer & Spiers, 2005; Gratier, 2011; Richard et al., 2014 and references therein).

An explanation for the mm-scale differentiated foliation might be that the fluid activity of the precipitating minerals (albite, quartz and calcite) was insufficient to transport mobile elements large distances in the intergranular fluid. Thus, deposition occurred in nearby voids (e.g., Gratier et al., 2013). Precipitation of albite, calcite and quartz in fractures and pores strengthened the rock locally, especially in the light-coloured folia (e.g., Richard et al., 2014). Such reaction-strengthening would slow down rates of dissolution–precipitation creep (e.g., Rutter, 1983) by increasing the mass transfer distance (late interseismic period, Fig. 11D). Increased sealing of the fractures with calcite may have led to a positive feedback loop, whereby the well-cemented, feldspar-rich light-coloured folia formed frictionally strong asperities that accumulated stress elastically and ultimately yielded by brittle, cataclastic deformation (cf. Richard et al., 2014).

The spaced foliation in the foliated cataclasites is pervasively folded on the mm- to cm-scale, and is transected by multiple generations of calcite and pseudotachylite veins that appear less folded than that foliation (Fig. 4A). These cross-cutting relationships suggest that periods of slow creep were accommodated by slip along the phyllosilicate-rich folia. Periodically, the foliated cataclasites hosted localized seismic slip, which caused fracturing, grain-size reduction, and frictional melting. In other words, the rock experienced a mixed-mode style of slip that was variably seismic to aseismic (e.g., Collettini et al., 2011; Little et al., 2019). The spatial pattern of weakening (phyllosilicate enrichment and alignment, in the dark folia) and strengthening (calcite cementation and veining, in the light folia) caused the rock to become layered and mechanically anisotropic, a situation that contributed to development of fold instabilities along the spaced foliation fabric. Calcite veins reflect episodic periods of fluid inflow that may have influenced the activity and distribution of the different deformation mechanisms (Richard et al., 2014).

5.2.3 Grain-size reduction, hydrous alteration and slow-to-fast slip processes in the ultracataclasites

The transition from the foliated cataclasite to the ultracataclasite is marked by: (a) extreme grain-size reduction (Figs. 5B, 6B); (b) bulk chemical changes (e.g., loss of Na, Ca and gain of K, Mg; Supporting Information Table S1.1); (c) mineral transformation from chlorite to trioctahedral mixed-layer smectite-chlorite ±corrensite to saponite and the K-feldspathization of albite (R. 2); (d) randomization of all CPOs in actinolite, epidote and titanite (Fig. 5B); and (e)

formation of K-feldspar and magnetite ±maghemite (Figs. 6G, 6H, 7). We infer that the dark-coloured, unfoliated, and clay-rich ultracataclasite unit with its sub-angular to rounded mafic clasts was derived from brittle fragmentation of the footwall. Bulk chemical changes, K-feldspathization of albite and neocrystallization of corrensite and K-feldspar indicate hydrous alteration of the basaltic footwall (XRD data of bulk mafic fault rocks Supporting Information Table S7.1). The well-rounded shape of the ultracataclasite lithic clasts in the ultracataclasite, and especially the coated structure of those clasts (clast-cortex aggregates, CCA; Figs. 6E–G), suggest clast rotation during granular flow and accretion of clay material (e.g., Boutareaud et al., 2008; Han & Hirose, 2012; Rempe et al., 2014). Granular flow of the ultracataclasite matrix is also suggested by attitude-dependant stretching versus folding of calcite veinlets embedded in it (Fig. 6A)—a relationship that indicates distributed shearing in that matrix (Little et al., 2019).

We interpret the high magnetic susceptibility of ~13×10^{-6} m^3 kg^{-1} measured in one of the ultracataclasite samples from the Mai'iu fault (compared to the other Mai'iu fault rocks and Goropu Metabasalt; Watson, 2019) and the occurrence of abundant, nm-sized magnetite±maghemite in ultracataclasite samples (in veins, as coatings, and swirled into reworked ultracataclasite clasts) to have formed by the breakdown of predominantly Fe-bearing mixed-layer smectite-chlorite during frictional shearing (thermomechanical decomposition). This interpretation is supported by changes in rock magnetic properties in other fault zones associated with recent earthquakes (e.g., 1999 Taiwan Chi-Chi earthquake, e.g., Mishima et al., 2009; Wenchuan earthquake in Sichuan Province, China, e.g., Cai et al., 2019) and high-velocity frictional experiments on crushed siltstones (containing quartz with a matrix of clay minerals, such as illite, kaolinite, smectite, and chlorite; e.g., Tanikawa et al., 2007). The high-velocity frictional experiment by Tanikawa et al. (2007) showed that the bulk magnetic susceptibility is proportional to the frictional work applied and increases with displacement due to thermal decomposition of paramagnetic clays in the powdered siltstone. Both thermally and mechanically driven mineral transformation reactions contribute to an anomalously high magnetic susceptibility, similar to that observed in the Mai'iu fault ultracataclasite unit (Fig. 7; e.g., Tanikawa et al., 2008).

Frictional devolatilization of Fe-bearing smectite clay is expected at temperatures >400 °C (Rowe & Griffith, 2015 and references therein). We did not observe breakdown of mixed-layer smectite-chlorite during the time-dependent magnetic susceptibility test; however, the test was performed under 1 atm and without any frictional work. Another possibility is that the magnetite was derived from external supersaturated hydrothermal fluids (i.e., external Fe-saturated fluids from ultramafic rocks in the hangingwall). This origin may be supported by the occurrence of magnetite along fractures in the ultracataclasites, but it does not explain the precipitation of single magnetite grains scattered within the fault rock or the magnetite nanograin coating around older ultracataclasite clasts (Supporting Information S5).

We infer that deformation of the ultracataclasite unit occurred at strain rates that varied with time. Hydrous alteration of the ultracataclasite matrix indicates that fluid inflow led to weakening of the matrix by retrogression of chlorite to corrensite (e.g., Moore, 2014). At the same time, cementation with unstable calcite would promote strengthening (e.g., Verberne et al., 2015). The observed suite of microstructures, including ductilely folded calcite veinlets, in the ultracataclasite unit indicate that periods of slow (probably aseismic) creep potentially alternated with fast (potentially seismic) slip events. CCAs similar to ones observed in our fault rocks have been reproduced in rotary shear experiments on frictionally heated granular material at seismic

velocities (Boutareaud et al. 2010, 2012). However, granular flow at a wide range of velocities can produce CCAs, even in the absence of thermal pressurization and fault rock fluidization at elevated temperature (Han & Hirose, 2012). While granular flow itself can facilitate CCA formation, the nanograin magnetite that coats clasts in the Mai'iu fault ultracataclasite appears to have originated from the thermal decomposition of Fe-bearing minerals such as corrensite during coseismic slip (Hirono et al., 2006; Mishima et al., 2006; Yang et al., 2012).

5.2.4 Frictionally weak fault gouges and fault-faceted surfaces of cobbles truncated by the principal displacement surface

The gouges contain recycled clasts from the underlying mafic footwall (ultracataclasite, cataclasite and mylonite fragments) and, from ultramafic rocks in the overlying hangingwall (dolomite and spinel-group minerals). This recycling is reflected by an increase in grain-size of mono- and polyphase clasts in the gouge relative to those in the underlying ultracataclasite (Fig. 8A). The recycled clasts in the gouges "float" in a fine-grained matrix dominated by saponite (Fig. 8C) and have random CPOs as indicated by a low M-index (Fig. 5B). Incorporation of ultramafic components into the gouge potentially promoted saponite-forming reactions (e.g., Moore & Rymer, 2012; Moore, 2014). Saponite is typically derived from the breakdown of chlorite and/or corrensite under declining temperatures. In mafic rocks, its formation requires fluid, and it consumes Mg, Fe, Al and (Ca + Na + K) derived from epidote, actinolite, albite (and, in our case potentially also the ultramafic hangingwall; e.g., Moore, 2014). Multiple phases of fluid flow might be recorded by our observation of saponitic domains overprinted by silica-rich ones (Figs. 8E, 8F).

The Pliocene alluvial conglomerates of the Gwoira Conglomerate (<3 km thick; Webber et al., 2020) and Quaternary deposits in the hangingwall form permeable pathways for the flow of meteoric fluids. Such fluids may have significantly altered and weakened the fault gouges in the shallowest part of the Mai'iu fault zone (Fig. 11A; Little et al., 2019). Experimental data on saponite-rich gouges (Carpenter et al., 2012; Moore et al., 2016; Boulton et al., 2018; Biemiller et al., submitted) indicate a weak coefficient of friction ($\mu<0.2$) and velocity-strengthening behaviour (subject to aseismic stable sliding) across a wide range of sub-seismic sliding velocities, temperatures, and effective normal stresses. However, at coseismic slip velocities (>0.1 m/s), velocity-strengthening minerals such as saponite do not necessarily prevent large earthquake rupture propagation (e.g., Di Toro et al., 2011; Faulkner et al., 2011; Boulton et al., 2017).

Our documentation of amorphous, mirror-like surfaces (nanograin coating) on the fault-faceted surfaces of cobbles truncated by the principal displacement surface may reflect seismic slip at shallow depths (Figs. 1K; 9)—although this interpretation is debatable (e.g., Verberne et al., 2014; De Paola et al., 2015 and references therein). In some laboratory experiments, a nanograin coating was produced by extreme grain comminution at seismic to subseismic creep velocities (e.g., Verberne et al., 2014). To assess whether the nanograins may have formed by comminution or shear heating, we calculated the minimum grain size that can be achieved by grinding (the grinding limit) for a basaltic rock, plagioclase and quartz based on fracture toughness (K_{IC}) and flow stresses at zero °K ($\hat{\tau}_0$; equation 13 in Sammis & Ben-Zion, 2008). The estimated minimum grain sizes are $>d_{minBasalt}$=268 nm, $>d_{minPlag}$=53 nm and $>d_{minQuartz}$=86 nm, respectively ($d_{minQuartz}$ was calculated by Sammis & Ben-Zion, 2008; Mizera, 2019). This estimation is imprecise due to the uncertainties in material properties (Sammis & Ben-Zion,

2008), but it suggests that the interpreted amorphous mirror-like coating on the cobble-surfaces (Figs. 9F, 9I, 9J) cannot be achieved by comminution alone. For this reason, we interpret that this nano-coating of amorphous material (Si and Al rich) and the injection veins (Figs. 9D, 9G, 9H) have been generated by frictional heating and slip along a narrow principal displacement surface (e.g., Oohashi et al., 2011; Smith et al., 2013; Rowe & Griffith, 2015 and references therein).

5.3 Strain rates during exhumational shearing of the Mai'iu fault

A maximum strain rate in the mafic mylonites that accommodated extensional slip on the Mai'iu fault can be calculated by the relation $\varepsilon = \mathring{u}/h$, where ε is the strain rate, $\mathring{u}$ the slip rate and h the thickness of the deforming zone (e.g., Rowe et al., 2011). Using the known fault dip-slip rate of ~10 mm/yr (Webber et al., 2018) and the width of the mylonites, which thin from ~60 m to as low as 1.5 m, calculated shear strain rates range from 5.3×10^{-12} to 2.1×10^{-10} s^{-1}. Getsinger and Hirth (2014) showed that flow laws for wet plagioclase can be similarly applied to fine-grained amphibole. Applying experimentally derived diffusion creep flow laws for wet Ab_{100} (H_2O 0.2 wt.%) by Offerhaus et al. (2001), pure albite with an average grain size diameter of ~15 µm in the mylonites at temperature of ~400 °C and differential stresses of ~60–100 MPa (Little et al., 2019; Mizera, 2019) is predicted to deform at strain rates of 1.5×10^{-13} to ~2.5×10^{-13} s^{-1}. This estimated strain rate is lower than that required to accommodate the full dip-slip rate. This shortfall may indicate that: (1) a natural polyphase mafic aggregate at greenschist facies conditions with its neoformed, interstitial chlorite (and with strong CPO and SPO) is weaker in diffusion creep than that predicted by extrapolations of laboratory experiments on wet albite (Little et al., 2019); or (2) the sheared thickness of the mylonite unit was thicker than assumed above.

To accommodate the Mai'iu fault's full slip rate in the ~1.5–3.0 m-wide foliated cataclasites by aseismic creep of the interconnected chlorite-rich folia would require a bulk strain rate of 1.1×10^{-10} to 2.1×10^{-10} s^{-1}, but this is likely higher than the actual rate of long-term, frictional-viscous pressure solution creep (e.g., Bos & Spiers, 2002; Imber et al., 2008). Aseismic creep may locally be impeded where chlorite-rich folia become locked against stronger albitic domains enlarging through precipitation and/or not dissolving fast enough (dissolution-limited), perhaps causing them to deform cataclastically (e.g., Richard et al., 2014). Such load transfer into the albite-rich layers might have caused elastic strain to increase and creep rates to reduce in the foliated cataclasites (i.e., case of partial locking, Fig. 11D; see Biemiller et al., submitted). Ductilely deformed calcite and pseudotachylite veins in the foliated cataclasite unit (Fig. 4A, inset) are strong evidence that some slip in this unit was seismic, and that fast-slip events were followed by postseismic and/or interseismic creep.

5.4 Seismic slip along an active low-angle normal fault

Overall, several lines of evidence suggest that some slip on the Mai'iu fault was seismic. These include: (1) pseudotachylite veins in mylonites and foliated cataclasites (Figs. 2E, 3E, 4A); (2) nm-sized magnetite±maghemite grains in veins cross-cutting the ultracataclasite matrix and wrapping older ultracataclasite clasts (Figs. 6G, 6H); and (3) mirror-like surfaces on hangingwall cobbles truncated by the fault and coated with amorphous material (Fig. 9). The numerous exposed, 5–40 mm thick pseudotachylite veins as well as brittle faults cross-cutting the spaced foliation in the foliated cataclasites indicate that aseismic fluid-assisted mass transfer

was periodically punctuated by earthquakes. During earthquakes, slip on the the propagating rupture may have led to the thermomechanical breakdown of Fe-bearing minerals (predominantly mixed-layer smectite-chlorite in the ultracataclasites) by frictional heating to form magnetite-bearing veins (e.g., Cai et al., 2019). Dated pseudotachylite veins hosted by the foliated cataclasite unit yield $^{40}Ar/^{39}Ar$ ages as young as ~2.2 Ma (Little et al., 2019). At the known slip rate of ~10 mm/yr on a 30–40° dipping fault, such ages imply pseudotachylite generation at 10–12 km depth. We infer that the foliated cataclasite and its pseudotachylite veins formed in a relatively strong, moderaltely-dipping, mid-crustal domain of elevated differential stress where slip was accommodated by a mixture of seismic and aseismic slip (Fig. 11A). We interpret the corridor of microseismicity at 12–25 km depth (Abers et al., 2016) to reflect present-day aseismic creep (e.g., Chiaraluce et al., 2007, 2014; Vadacca et al., 2016) that is taking place in the down-dip, un-exhumed equivalents of the described mylonites and foliated cataclasites.

6 Conclusions

The Mai'iu fault zone, an extensional detachment formed from inversion of a pre-existing ophiolitic suture, developed in a pre-existing, fine-grained, footwall metabasaltic protolith. The upwardly narrowing arrangement of progressively lower-temperature fault rocks developed from this protolith display clear evidence that slip became progressively localized and more brittle as slip on the fault carried the footwall towards the surface. Microstructures in the fault rocks record transitions in dominant deformation mechanisms in metabasaltic rocks accommodating slip, and chlorite thermometry allows us to assign approximate temperatures to these transitions.

- Slip within the mylonites was accomplished by diffusion creep accompanied by rotation and grain-boundary sliding of pre-existing, fine-grained (~6–35 μm in diameter) epidote, actinolite, chlorite, and albite at temperatures >270–370°C and strain-rates of 5.3×10^{-12} to 2.1×10^{-10} s^{-1}.
- At shallower levels on the fault (T≥150–300°C), fluid-assisted mass transfer of albite, quartz and calcite led to mineral transformation reactions with continuous chlorite growth, creating a 1.5–3 m thick zone of foliated cataclasites. This zone deformed in part by aseismic frictional-viscous creep at a maximum strain rate of 1.1×10^{-10} to 2.1×10^{-10} s^{-1}.
- Build-up of elastic-strain in the foliated cataclasites eventually facilitated earthquakes propagation through them, as indicated by the injection of pseudotachylite veins. Later creep caused folding of those veins.
- The foliated cataclasites formed at ~8–15 km depth in a frictionally strong, mid-crustal part of the fault that dipped at least ~30°. This zone maintained elevated differential stresses and deformed at slip rates that varied spatiotemporally from high (seismic) to low (aseismic).
- Slip in the shallower-formed ultracataclasite unit (T~150–225°C) was at least in part accomplished by distributed granular flow of the ultrafine-grained mafic minerals.
- At the shallowest crustal levels (T<150°C), clay-rich gouges contain abundant saponite, a velocity-strengthening, weak mineral (μ<0.2). Given sufficient areal

distribution on the fault plane, saponite gouges may have promoted aseismic slip on the shallowest dipping most poorly oriented part of the Mai'iu fault (dipping ~15–24°). In the light of our data, slip on the shallow Mai'iu fault does not present a mechanical paradox.

Acknowledgments, Samples, and Data

Marsden Fund grant VUW1310 provided financial support to conduct this research. We are grateful to Hugh Davies (University of Papua New Guinea) and Ian Smith (University of Auckland) for providing field book scans and discussions. We thank Susan Ellis, Samuel Webber, Jürgen Österle, Laura Wallace, Kevin Norton, and Daniel Stockli for field support and discussions. This work profited from discussions with André Niemeijer that helped to sharpen our thinking. Special thanks go to the many landowners, oral chiefs, elders, and citizens who granted us permission to study their land and who allowed us to stay in their villages or houses and were supportive with advice and help.We also thank our guides and carriers without whom this work would not have been possible.

All structural data can be obtained from Little et al. (2019) and Mizera (2019). All microstructural and geochemical data presented in this study are available through Mizera (2019).

References

Abers, G. A., Mutter, C. Z., & Fang, J. (1997). Shallow dips of normal faults during rapid extension: Earthquakes in the Woodlark-D'Entrecasteaux rift system, Papua New Guinea. Journal of Geophysical Research: Solid Earth, 102(B7), 15301-15317.

Abers, G. A., Eilon, Z., Gaherty, J. B., Jin, G., Kim, Y. H., Obrebski, M., & Dieck, C. (2016). Southeast Papuan crustal tectonics: Imaging extension and buoyancy of an active rift. Journal of Geophysical Research: Solid Earth, 121(2), 951-971.

Anderson, E. M. (1951). The dynamics of faulting.

Aspiroz, M. D., Lloyd, G. E., & Fernández, C. (2007). Development of lattice preferred orientation in clinoamphiboles deformed under low-pressure metamorphic conditions. A SEM/EBSD study of metabasites from the Aracena metamorphic belt (SW Spain). Journal of Structural Geology, 29(4), 629-645.

Axen, G. J., & Bartley, J. M. (1997). Field tests of rolling hinges: Existence, mechanical types, and implications for extensional tectonics. Journal of Geophysical Research: Solid Earth, 102(B9), 20515-20537.

Axen, G. J. (2004). Low-angle normal fault mechanics and crustal strength. In: Rheology and Deformation of the Lithosphere (ed. G. Karner), 46-91 (Columbia University Press, 2004).

Axen, G. J. (2007). Research Focus: Significance of large-displacement, low-angle normal faults. Geology, 35(3), 287-288.

Bachmann, F., Hielscher, R., & Schaeben, H. (2010). Texture analysis with MTEX–free and open source software toolbox. In Solid State Phenomena (Vol. 160, pp. 63-68). Trans Tech Publications Ltd.

Behrmann, J. H. (1985). Crystal plasticity and superplasticity in quartzite; a natural example. Tectonophysics, 115(1), 101-129.

Beiersdorfer, R. E., & Day, H. W. (1995). Mineral paragenesis of pumpellyite in lowgrade mafic rocks. Low-Grade Metamorphism of Mafic Rocks: Boulder, Colorado, Geological Society of America. Special Paper, 296, 5-27.

Bercovici, D., & Ricard, Y. (2012). Mechanisms for the generation of plate tectonics by two-phase grain-damage and pinning. Physics of the Earth and Planetary Interiors, 202, 27-55.

Bettison, L. A., & Schiffman, P. (1988). Compositional and structural variations of phyllosilicates from the Point Sal ophiolite, California. American Mineralogist, 73(1-2), 62-76.

Bevins, R. E., Robinson, D., & Rowbotham, G. (1991). Compositional variations in mafic phyllosilicates from regional low-grade metabasites and application of the chlorite geothermometer. Journal of Metamorphic Geology, 9(6), 711-721.

Biemiller, J., Ellis, S., Mizera, M., Little, T., Wallace, L., & Lavier, L. (2019). Tectonic inheritance following failed continental subduction: a model for core complex formation in cold, strong lithosphere. Tectonics, 38(5), 1742-1763.

Bos, B., & Spiers, C. J. (2002). Frictional-viscous flow of phyllosilicate-bearing fault rock: Microphysical model and implications for crustal strength profiles. Journal of Geophysical Research: Solid Earth (1978–2012), 107(B2), ECV-1.

Boulton, C., Yao, L., Faulkner, D. R., Townend, J., Toy, V. G., Sutherland, R., ... & Shimamoto, T. (2017). High-velocity frictional properties of Alpine Fault rocks: Mechanical data, microstructural analysis, and implications for rupture propagation. Journal of Structural Geology, 97, 71-92.

Boulton, C., Barth, N. C., Moore, D. E., Lockner, D. A., Townend, J., & Faulkner, D. R. (2018). Frictional properties and 3-D stress analysis of the southern Alpine Fault, New Zealand. Journal of Structural Geology.

Bourdelle, F., & Cathelineau, M. (2015). Low-temperature chlorite geothermometry: a graphical representation based on a T–R2+–Si diagram. European Journal of Mineralogy, 27(5), 617-626.

Boutareaud, S., Calugaru, D. G., Han, R., Fabbri, O., Mizoguchi, K., Tsutsumi, A., & Shimamoto, T. (2008). Clay-clast aggregates: A new textural evidence for seismic fault sliding?. Geophysical Research Letters, 35(5).

Boutareaud, S., Boullier, A. M., Andreani, M., Calugaru, D. G., Beck, P., Song, S. R., & Shimamoto, T. (2010). Clay clast aggregates in gouges: New textural evidence for seismic faulting. Journal of Geophysical Research: Solid Earth, 115(B2).

Boutareaud, S., Hirose, T., Andréani, M., Pec, M., Calugaru, D. G., Boullier, A. M., & Doan, M. L. (2012). On the role of phyllosilicates on fault lubrication: Insight from micro-and nanostructural investigations on talc friction experiments. Journal of Geophysical Research: Solid Earth, 117(B8).

Buck, W. R. (1990). Comment on "Origin of regional, rooted low-angle normal faults: A mechanical model and its tectonic implications" by An Yin, Tectonics, 9(3), 545–546, doi: 10.1029/TC009i003p00545.

Bunge, H. J. (2013). Texture analysis in materials science: mathematical methods. Elsevier.

Byerlee, J. (1978). Friction of rocks. Pure and applied geophysics, 116(4-5), 615-626.

Cai, Y., Pei, J., Wang, H., Sheng, M., & Si, J. (2019). Paleo-earthquakes revealed by rock magnetic evidence from the Anxian-Guanxian Fault, Sichuan Province, China. Tectonophysics, 752, 68-80.

Cairns, E. A., Little, T. A., Turner, G. M., Wallace, L. M., & Ellis, S. (2015). Paleomagnetic evidence for vertical-axis rotations of crustal blocks in the Woodlark Rift, SE Papua New Guinea: Miocene to present-day kinematics in one of the world's most rapidly extending plate boundary zones. Geochemistry, Geophysics, Geosystems, 16(7), 2058-2081.

Carpenter, B. M., Saffer, D. M., & Marone, C. (2012). Frictional properties and sliding stability of the San Andreas fault from deep drill core. Geology, 40(8), 759-762.

Cathelineau, M., & Nieva, D. (1985). A chlorite solid solution geothermometer the Los Azufres (Mexico) geothermal system. Contributions to Mineralogy and Petrology, 91(3), 235-244.

Cathelineau, M. (1988). Cation site occupancy in chlorites and illites as function of temperature. Clay minerals, 23(4), 471-85.

Chiaraluce, L., Chiarabba, C., Collettini, C., Piccinini, D., & Cocco, M. (2007). Architecture and mechanics of an active low-angle normal fault: Alto Tiberina fault, northern Apennines, Italy. Journal of Geophysical Research: Solid Earth, 112(B10).

Chiaraluce, L., Amato, A., Carannante, S., Castelli, V., Cattaneo, M., Cocco, M., ... & Marzorati, S. (2014). The Alto Tiberina Near Fault Observatory (northern Apennines, Italy). Annals of Geophysics, 57(3).

Choi, E., & Buck, W. R. (2012). Constraints on the strength of faults from the geometry of rider blocks in continental and oceanic core complexes. Journal of Geophysical Research: Solid Earth, 117(B4).

Choi, E., Buck, W. R., Lavier, L. L., & Petersen, K. D. (2013). Using core complex geometry to constrain fault strength. Geophysical Research Letters, 40(15), 3863-3867.

Collettini, C., & Sibson, R. H. (2001). Normal faults, normal friction?. Geology, 29(10), 927-930.

Collettini, C., & Holdsworth, R. E. (2004). Fault zone weakening and character of slip along low-angle normal faults: insights from the Zuccale fault, Elba, Italy. Journal of the Geological Society, 161(6), 1039-1051.

Collettini, C., Niemeijer, A., Viti, C., & Marone, C. (2009). Fault zone fabric and fault weakness. Nature, 462(7275), 907-910.

Collettini, C. (2011). The mechanical paradox of low-angle normal faults: Current understanding and open questions. Tectonophysics, 510(3), 253-268.

Collettini, C., Niemeijer, A., Viti, C., Smith, S. A., & Marone, C. (2011). Fault structure, frictional properties and mixed-mode fault slip behavior. Earth and Planetary Science Letters, 311(3-4), 316-327.

Collettini, C., Tesei, T., Scuderi, M. M., Carpenter, B. M., & Viti, C. (2019). Beyond Byerlee friction, weak faults and implications for slip behavior. Earth and Planetary Science Letters, 519, 245-263.

Cooper, F. J., Platt, J. P., & Behr, W. M. (2017). Rheological transitions in the middle crust: insights from Cordilleran metamorphic core complexes. Solid Earth, 8(1), 199.

Cross, A. J. (2015). Microstructural evolution under non-steady state deformation in mid-crustal ductile shear zones (Doctoral dissertation, University of Otago).

Daczko, N. R., Caffi, P., Halpin, J. A., & Mann, P. (2009). Exhumation of the Dayman dome metamorphic core complex, eastern Papua New Guinea. Journal of Metamorphic Geology, 27(6), 405-422.

Daczko, N. R., Caffi, P., & Mann, P. (2011). Structural evolution of the Dayman dome metamorphic core complex, eastern Papua New Guinea. Bulletin, 123(11-12), 2335-2351.

Davies, H. L., & Smith, I. E. (1974). Tufi-Cape Nelson, Papua New Guinea, Sheets SC/55–8 and SC55-4, Geological Series and Explanatory Notes: Bureau of Mineral Resources, Geology and Geophysics, Department of Minerals and Energy in co-operation with the Geological Survey of Papua New Guinea, scale 1:250,000.

Davies, H. L. (1978). Folded thrust fault and associated metamorphism in the Suckling-Dayman massif, Papua New Guinea. Geological Survey of Papua New Guinea.

De Paola, N., Holdsworth, R. E., Viti, C., Collettini, C., & Bullock, R. (2015). Can grain size sensitive flow lubricate faults during the initial stages of earthquake propagation?. Earth and Planetary Science Letters, 431, 48-58.

Di Toro, G., Han, R., Hirose, T., De Paola, N., Nielsen, S., Mizoguchi, K., ... & Shimamoto, T. (2011). Fault lubrication during earthquakes. Nature, 471(7339), 494.

Dunlop, D. J., & Özdemir, Ö. Rock magnetism//Fundamentals and frontiers, 1997.

Dunlop, D. J., Özdemir, Ö., & Schmidt, P. W. (1997). Paleomagnetism and paleothermometry of the Sydney Basin 2. Origin of anomalously high unblocking temperatures. Journal of Geophysical Research: Solid Earth, 102(B12), 27285-27295.

Eilon, Z., Abers, G. A., Gaherty, J. B., & Jin, G. (2015). Imaging continental breakup using teleseismic body waves: The Woodlark Rift, Papua New Guinea. Geochemistry, Geophysics, Geosystems, 16(8), 2529-2548.

Elyaszadeh, R., Prior, D. J., Sarkarinejad, K., & Mansouri, H. (2018). Different slip systems controlling crystallographic preferred orientation and intracrystalline deformation of amphibole in mylonites from the Neyriz mantle diapir, Iran. Journal of Structural Geology, 107, 38-52.

Etheridge, M. A., Wall, V. J., Cox, S. F., & Vernon, R. H. (1984). High fluid pressures during regional metamorphism and deformation: implications for mass transport and

deformation mechanisms. Journal of Geophysical Research: Solid Earth (1978–2012), 89(B6), 4344-4358.

Faulkner, D. R., Mitchell, T. M., Healy, D., & Heap, M. J. (2006). Slip on 'weak' faults by the rotation of regional stress in the fracture damage zone. Nature, 444(7121), 922.

Faulkner, D. R., Mitchell, T. M., Behnsen, J., Hirose, T., & Shimamoto, T. (2011). Stuck in the mud? Earthquake nucleation and propagation through accretionary forearcs. Geophysical Research Letters, 38(18).

Ferris, A., Abers, G. A., Zelt, B., Taylor, B., & Roecker, S. (2006). Crustal structure across the transition from rifting to spreading: the Woodlark rift system of Papua New Guinea. Geophysical Journal International, 166(2), 622-634.

Finlayson, D. M., Drummond, B. J., Collins, C. D. M., & Connelly, J. B. (1977). Crustal structures in the region of the Papuan Ultramafic Belt. Physics of the Earth and Planetary Interiors, 14(1), 13-29.

Getsinger, A. J., Hirth, G., Stünitz, H., & Goergen, E. T. (2013). Influence of water on rheology and strain localization in the lower continental crust. Geochemistry, Geophysics, Geosystems, 14(7), 2247-2264.

Getsinger, A. J., & Hirth, G. (2014). Amphibole fabric formation during diffusion creep and the rheology of shear zones. Geology, 42(6), 535-538.

Gratier, J. P. (2011). Fault permeability and strength evolution related to fracturing and healing episodic processes (years to millennia): the role of pressure solution. Oil & Gas Science and Technology–Revue d'IFP Energies nouvelles, 66(3), 491-506.

Gratier, J. P., Dysthe, D. K., & Renard, F. (2013). The role of pressure solution creep in the ductility of the Earth's upper crust. In Advances in Geophysics (Vol. 54, pp. 47-179). Elsevier.

Han, R., & Hirose, T. (2012). Clay–clast aggregates in fault gouge: An unequivocal indicator of seismic faulting at shallow depths?. Journal of Structural Geology, 43, 92-99.

Hashimoto, M. (1972). Reactions producing actinolite in basic metamorphic rocks. Lithos, 5(1), 19-31.

Healy, D. (2008). Damage patterns, stress rotations and pore fluid pressures in strike-slip fault zones. Journal of Geophysical Research: Solid Earth, 113(B12).

Herwegh, M., Linckens, J., Ebert, A., Berger, A., & Brodhag, S. H. (2011). The role of second phases for controlling microstructural evolution in polymineralic rocks: A review. Journal of Structural Geology, 33(12), 1728-1750.

Hirono, T., Lin, W., Yeh, E. C., Soh, W., Hashimoto, Y., Sone, H., ... & Murayama, M. (2006). High magnetic susceptibility of fault gouge within Taiwan Chelungpu fault: Nondestructive continuous measurements of physical and chemical properties in fault rocks recovered from Hole B, TCDP. Geophysical Research Letters, 33(15).

Hreinsdóttir, S., & Bennett, R. A. (2009). Active aseismic creep on the Alto Tiberina low-angle normal fault, Italy. Geology, 37(8), 683-686.

Imber, J., Holdsworth, R. E., Butler, C. A., & Strachan, R. A. (2001). A reappraisal of the Sibson-Scholz fault zone model: The nature of the frictional to viscous ("brittle-ductile") transition along a long-lived, crustal-scale fault, Outer Hebrides, Scotland. Tectonics, 20(5), 601-624.

Imber, J., Holdsworth, R. E., Smith, S. A. F., Jefferies, S. P., & Collettini, C. (2008). Frictional-viscous flow, seismicity and the geology of weak faults: a review and future directions. Geological Society, London, Special Publications, 299(1), 151-173.

Jackson, J. A. (1987). Active normal faulting and crustal extension. Geological Society, London, Special Publications, 28(1), 3-17

Jackson, J. A., & White, N. J. (1989). Normal faulting in the upper continental crust: observations from regions of active extension. Journal of Structural Geology, 11(1-2), 15-36.

Jefferies, S. P., Holdsworth, R. E., Shimamoto, T., Takagi, H., Lloyd, G. E., & Spiers, C. J. (2006). Origin and mechanical significance of foliated cataclastic rocks in the cores of crustal-scale faults: Examples from the Median Tectonic Line, Japan. Journal of Geophysical Research: Solid Earth, 111(B12).

Kilian, R., Heilbronner, R., & Stünitz, H. (2011). Quartz grain size reduction in a granitoid rock and the transition from dislocation to diffusion creep. Journal of Structural Geology, 33(8), 1265-1284.

Lavier, L. L., Roger Buck, W., & Poliakov, A. N. (1999). Self-consistent rolling-hinge model for the evolution of large-offset low-angle normal faults. Geology, 27(12), 1127-1130.

Lindley, I. D. (2014). Suckling Dome and the Australian–Woodlark plate boundary in eastern Papua: the geology of the Keveri and Ada'u Valleys. Australian Journal of Earth Sciences, 61(8), 1125-1147.

Lister, G. S., & Davis, G. A. (1989). The origin of metamorphic core complexes and detachment faults formed during Tertiary continental extension in the northern Colorado River region, USA. Journal of Structural Geology, 11(1), 65-94.

Little, T. A., Webber, S. M., Mizera, M., Boulton, C., Oesterle, J., Ellis, S., Boles, A., van der Pluijm, B., Norton, K., Seward, D., Biemiller, J., and Wallace, L. (2019): Evolution of a rapidly slipping, active low-angle normal fault, Suckling-Dayman Metamorphic Core Complex, SE Papua New Guinea.

Lockner, D. A., Morrow, C., Moore, D., & Hickman, S. (2011). Low strength of deep San Andreas fault gouge from SAFOD core. Nature, 472(7341), 82.

Mainprice, D., Bachmann, F., Hielscher, R., & Schaeben, H. (2015). Descriptive tools for the analysis of texture projects with large datasets using MTEX: strength, symmetry and components. Geological Society, London, Special Publications, 409(1), 251-271.

Menegon, L., Fusseis, F., Stünitz, H., & Xiao, X. (2015). Creep cavitation bands control porosity and fluid flow in lower crustal shear zones. Geology, 43(3), 227-230.

Mishima, T., Hirono, T., Soh, W., & Song, S. R. (2006). Thermal history estimation of the Taiwan Chelungpu fault using rock-magnetic methods. Geophysical research letters, 33(23).

Mishima, T., Hirono, T., Nakamura, N., Tanikawa, W., Soh, W., & Song, S. R. (2009). Changes to magnetic minerals caused by frictional heating during the 1999 Taiwan Chi-Chi earthquake. Earth, planets and space, 61(6), 797-801.

Mizera, M. (2019). Deformational Processes Accommodating Slip on an Active Low-Angle Normal Fault, Suckling-Dayman Metamorphic Core Complex, Papua New Guinea.

Mizera, M., Little, T. A., Biemiller, J., Ellis, S., Webber, S., & Norton, K. P. (2019). Structural and Geomorphic Evidence for Rolling-Hinge Style Deformation of an Active Continental Low-Angle Normal Fault, SE Papua New Guinea. Tectonics, 38(5), 1556-1583.

Montési, L. G. (2013). Fabric development as the key for forming ductile shear zones and enabling plate tectonics. Journal of Structural Geology, 50, 254-266.

Moore, D. E., & Lockner, D. A. (2004). Crystallographic controls on the frictional behavior of dry and water-saturated sheet structure minerals. Journal of Geophysical Research: Solid Earth, 109(B3).

Moore, D. E., & Rymer, M. J. (2012). Correlation of clayey gouge in a surface exposure of serpentinite in the San Andreas Fault with gouge from the San Andreas Fault Observatory at Depth (SAFOD). Journal of Structural Geology, 38, 51-60.

Moore, D. E. (2014). Comparative mineral chemistry and textures of SAFOD fault gouge and damage-zone rocks. Journal of Structural Geology, 68, 82-96.

Moore, D. E., Lockner, D. A., & Hickman, S. (2016). Hydrothermal frictional strengths of rock and mineral samples relevant to the creeping section of the San Andreas Fault. Journal of Structural Geology, 89, 153-167.

Niemeijer, A. R., & Spiers, C. J. (2005). Influence of phyllosilicates on fault strength in the brittle-ductile transition: Insights from rock analogue experiments. Geological Society, London, Special Publications, 245(1), 303-327.

Offerhaus, L. J., Wirth, R., & Dresen, G. (2001). High-temperature creep of polycrystalline albite. Deformation Mechanisms, Rheology and Tectonics, 124, 107-131.

Oohashi, K., Hirose, T., & Shimamoto, T. (2011). Shear-induced graphitization of carbonaceous materials during seismic fault motion: Experiments and possible implications for fault mechanics. Journal of Structural Geology, 33(6), 1122-1134.

Österle, J. (2019). The thermo-tectonic evolution of the Suckling-Dayman metamorphic core complex, southeastern Papua New Guinea (Doctoral dissertation, Victoria University of Wellington).

Österle, J. E., Stockli, D. F., Seward, D., & Little, T. A. Dating of young (< 1 Ma) tephras: Using U-Pb (zircon) and (U-Th [-Sm])/He (zircon, apatite, magnetite) chronometers to unravel the eruption age of a tephra in the Woodlark Rift of Papua New Guinea. Terra Nova.

Özdemir, Ö., & Banerjee, S. K. (1984). High temperature stability of maghemite (γ-Fe2O3). Geophysical research letters, 11(3), 161-164.

Özdemir, Ö. (1990). High-temperature hysteresis and thermoremanence of single-domain maghemite. Physics of the Earth and planetary interiors, 65(1-2), 125-136.

Pearce, M. A., Wheeler, J., & Prior, D. J. (2011). Relative strength of mafic and felsic rocks during amphibolite facies metamorphism and deformation. Journal of Structural Geology, 33(4), 662-675.

Platt, J. P. (2015). Rheology of two-phase systems: A microphysical and observational approach. Journal of Structural Geology, 77, 213-227.

Platt, J. P., Behr, W. M., & Cooper, F. J. (2015). Metamorphic core complexes: windows into the mechanics and rheology of the crust. Journal of the Geological Society, 172(1), 9-27.

Rempe, M., Smith, S. A., Ferri, F., Mitchell, T. M., & Di Toro, G. (2014). Clast-cortex aggregates in experimental and natural calcite-bearing fault zones. Journal of Structural Geology, 68, 142-157.

Rice, J. R. (1992). Fault stress states, pore pressure distributions, and the weakness of the San Andreas fault. International Geophysics, 51, 475-503.

Richard, J., Gratier, J. P., Doan, M. L., Boullier, A. M., &Renard, F. (2014). Rock and mineral transformations in a fault zone leading to permanent creep: Interactions between brittle and viscous mechanisms in the San Andreas Fault. Journal of Geophysical Research: Solid Earth, 119(11), 8132-8153.

Rigo, A., Lyon-Caen, H., Armijo, R., Deschamps, A., Hatzfeld, D., Makropoulos, K., ... & Kassaras, I. (1996). A microseismic study in the western part of the Gulf of Corinth (Greece): implications for large-scale normal faulting mechanisms. Geophysical Journal International, 126(3), 663-688.

Robinson, D., Schmidt, S. T., & De Zamora, A. S. (2002). Reaction pathways and reaction progress for the smectite-to-chlorite transformation: evidence from hydrothermally altered metabasites. Journal of metamorphic Geology, 20(1), 167-174.

Rowe, C. D., Meneghini, F., & Moore, J. C. (2011). Textural record of the seismic cycle: Strain-rate variation in an ancient subduction thrust. Geological Society, London, Special Publications, 359(1), 77-95.

Rowe, C. D., & Griffith, W. A. (2015). Do faults preserve a record of seismic slip: A second opinion. Journal of Structural Geology, 78, 1-26.

Rutter, E. H., & Mainprice, D. H. (1979). On the possibility of slow fault slip controlled by a diffusive mass transfer process. Gerlands Beitrage zur Geophysik, 88(2), 154-162.

Rutter, E. H. (1983). Pressure solution in nature, theory and experiment. Journal of the Geological Society, 140(5), 725-740.

Sammis, C. G., & Ben-Zion, Y. (2008). Mechanics of grain-size reduction in fault zones. Journal of Geophysical Research: Solid Earth, 113(B2).

Scholz, C. H. (2002). The Mechanics of Earthquakes and Faulting. Cambridge University Press, Cambridge, 471 p.

Sibson, R. H. (1985). A note on fault reactivation. Journal of Structural Geology, 7(6), 751-754.

Sibson, R. H. (1992). Implications of fault-valve behaviour for rupture nucleation and recurrence. Tectonophysics, 211(1-4), 283-293.

Skelton, A. D. L., Valley, J. W., Graham, C. M., Bickle, M. J., & Fallick, A. E. (2000). The correlation of reaction and isotope fronts and the mechanism of metamorphic fluid flow. Contributions to Mineralogy and Petrology, 138(4), 364-375.

Skemer, P., Katayama, I., Jiang, Z., & Karato, S. I. (2005). The misorientation index: Development of a new method for calculating the strength of lattice-preferred orientation. Tectonophysics, 411(1-4), 157-167.

Sleep, N. H., & Blanpied, M. L. (1992). Creep, compaction and the weak rheology of major faults. Nature, 359(6397), 687-692.

Smith, I. E. & Davies, H. L. (1976). Geology of the Southeast Papuan Mainland. Bureau of mineral resources, geology and geophysics, Bulletin 165.

Smith, S. A. F., Holdsworth, R. E., Collettini, C., & Pearce, M. A. (2011). The microstructural character and mechanical significance of fault rocks associated with a continental low-angle normal fault: the Zuccale Fault, Elba Island, Italy. Geological Society, London, Special Publications, 359(1), 97-113.

Smith, I. E. (2013). The chemical characterization and tectonic significance of ophiolite terrains in southeastern Papua New Guinea. Tectonics, 32(2), 159-170.

Smith, S. A. F., Di Toro, G., Kim, S., Ree, J. H., Nielsen, S., Billi, A., & Spiess, R. (2013). Coseismic recrystallization during shallow earthquake slip. Geology, 41(1), 63-66.

Speckbacher, R., Behrmann, J. H., Nagel, T. J., Stipp, M., & Mahlke, J. (2012). Fluid flow and metasomatic fault weakening in the Moresby Seamount detachment, Woodlark Basin, offshore Papua New Guinea. Geochemistry, Geophysics, Geosystems, 13(11).

Speckbacher, R., Stipp, M., Behrmann, J. H., & Heidelbach, F. (2013). Fluid-assisted fracturing, cataclasis, and resulting plastic flow in mylonites from the Moresby Seamount detachment, Woodlark Basin. Journal of Structural Geology, 56, 156-171.

Spencer, J. E. (1984). Role of tectonic denudation in warping and uplift of low-angle normal faults. Geology, 12(2), 95-98.

Spencer, J. E., & Chase, C. G. (1989). Role of crustal flexure in initiation of low-angle normal faults and implications for structural evolution of the Basin and Range province. Journal of Geophysical Research: Solid Earth, 94(B2), 1765-1775.

Spencer, J. E. (2010). Structural analysis of three extensional detachment faults with data from the 2000 Space-Shuttle Radar Topography Mission. GSA Today, 20(8), 4-10.

Stenvall, C. A., Fagereng, Å., & Diener, J. F. (2019). Weaker than weakest: on the strength of shear zones. Geophysical Research Letters, 46(13), 7404-7413.

Stewart, M., Holdsworth, R. E., & Strachan, R. A. (2000). Deformation processes and weakening mechanisms within the frictional–viscous transition zone of major crustal-scale faults: insights from the Great Glen Fault Zone, Scotland. Journal of Structural Geology, 22(5), 543-560.

Stipp, M., Stünitz, H., Heilbronner, R., & Schmid, S. M. (2002). Dynamic recrystallization of quartz: correlation between natural and experimental conditions. Geological Society, London, Special Publications, 200(1), 171190.

Stipp, M., & Kunze, K. (2008). Dynamic recrystallization near the brittle-plastic transition in naturally and experimentally deformed quartz aggregates. Tectonophysics, 448(1-4), 77-97.

Stünitz, H., & Tullis, J. (2001). Weakening and strain localization produced by syn-deformational reaction of plagioclase. International Journal of Earth Sciences, 90(1), 136-148.

Surace, I. R., Clauer, N., Thélin, P., & Pfeifer, H. R. (2011). Structural analysis, clay mineralogy and K–Ar dating of fault gouges from Centovalli Line (Central Alps) for reconstruction of their recent activity. Tectonophysics, 510(1-2), 80-93.

Tanikawa, W., Mishima, T., Hirono, T., Lin, W., Shimamoto, T., Soh, W., & Song, S. R. (2007). High magnetic susceptibility produced in high-velocity frictional tests on core samples from the Chelungpu fault in Taiwan. Geophysical Research Letters, 34(15).

Tanikawa, W., Mishima, T., Hirono, T., Soh, W., & Song, S. R. (2008). High magnetic susceptibility produced by thermal decomposition of core samples from the Chelungpu fault in Taiwan. Earth and Planetary Science Letters, 272(1-2), 372-381.

Taylor, B., & Huchon, P. (2002). Active continental extension in the western Woodlark Basin: a synthesis of Leg 180 results. In Proceedings of the Ocean Drilling Program, Scientific Results (Vol. 180, pp. 1-36). P. Huchon, B. Taylor, and A. Klaus.

Tregoning, P., Lambeck, K., Stolz, A., Morgan, P., McClusky, S. C., Beek, P., ... & Murphy, B. (1998). Estimation of current plate motions in Papua New Guinea from Global Positioning System observations. Journal of Geophysical Research: Solid Earth, 103(B6), 12181-12203.

Vadacca, L., Casarotti, E., Chiaraluce, L., & Cocco, M. (2016). On the mechanical behaviour of a low-angle normal fault: the Alto Tiberina fault (Northern Apennines, Italy) system case study. Solid Earth, 7(6), 1537-1549.

Verberne, B. A., Plümper, O., de Winter, D. M., & Spiers, C. J. (2014). Superplastic nanofibrous slip zones control seismogenic fault friction. Science, 346(6215), 1342-1344.

Verberne, B. A., Niemeijer, A. R., De Bresser, J. H., & Spiers, C. J. (2015). Mechanical behavior and microstructure of simulated calcite fault gouge sheared at 20–600 C: Implications for natural faults in limestones. Journal of Geophysical Research: Solid Earth, 120(12), 8169-8196.

Viegas, G., Menegon, L., & Archanjo, C. (2016). Brittle grain-size reduction of feldspar, phase mixing and strain localization in granitoids at mid-crustal conditions (Pernambuco shear zone, NE Brazil). Solid Earth, 7(2), 375-396.

Wallace, L. M., Stevens, C., Silver, E., McCaffrey, R., Loratung, W., Hasiata, S., ... & Taugaloidi, J. (2004). GPS and seismological constraints on active tectonics and arc-continent collision in Papua New Guinea: Implications for mechanics of microplate rotations in a plate boundary zone. Journal of Geophysical Research: Solid Earth, 109(B5).

Wallace, L. M., Ellis, S., Little, T., Tregoning, P., Palmer, N., Rosa, R., ... & Kwazi, J. (2014). Continental breakup and UHP rock exhumation in action: GPS results from the Woodlark Rift, Papua New Guinea. Geochemistry, Geophysics, Geosystems, 15(11), 4267-4290.

Watson, E. (2019). Using paleomagnetism to test rolling hinge behaviour of an active low angle normal fault, Papua New Guinea.

Warren, J. M., & Hirth, G. (2006). Grain size sensitive deformation mechanisms in naturally deformed peridotites. Earth and Planetary Science Letters, 248(1-2), 438-450.

Webb, L. E., Baldwin, S. L., Little, T. A., & Fitzgerald, P. G. (2008). Can microplate rotation drive subduction inversion?. Geology, 36(10), 823-826.

Webber, S., Norton, K. P., Little, T. A., Wallace, L. M., & Ellis, S. (2018). How fast can low-angle normal faults slip? Insights from cosmogenic exposure dating of the active Mai'iu fault, Papua New Guinea. Geology, 46(3), 227-230.

Webber, S., Little, T. A., Norton, K. P., Österle, J., Mizera, M., Seward, D., & Holden, G. (2020). Progressive back-warping of a rider block atop an actively exhuming, continental low-angle normal fault. Journal of Structural Geology, 130, 103906.

Westaway, R. (2005). Active low-angle normal faulting in the Woodlark extensional province, Papua New Guinea: A physical model. Tectonics, 24(6).

Whitney, D. L., Teyssier, C., Rey, P., & Buck, W. R. (2013). Continental and oceanic core complexes. Geological Society of America Bulletin, 125(3-4), 273-298.

Wintsch, R. P., Christoffersen, R., & Kronenberg, A. K. (1995). Fluid-rock reaction weakening of fault zones. Journal of Geophysical Research: Solid Earth, 100(B7), 13021-13032.

Wintsch, R. P., & Yeh, M. W. (2013). Oscillating brittle and viscous behavior through the earthquake cycle in the Red River Shear Zone: Monitoring flips between reaction and textural softening and hardening. Tectonophysics, 587, 46-62.

Yang, T., Chen, J., Wang, H., & Jin, H. (2012). Rock magnetic properties of fault rocks from the rupture of the 2008 Wenchuan earthquake, China and their implications: Preliminary results from the Zhaojiagou outcrop, Beichuan County (Sichuan). Tectonophysics, 530, 331-341.

Yavuz, F., Kumral, M., Karakaya, N., Karakaya, M. Ç., & Yıldırım, D. K. (2015). A Windows program for chlorite calculation and classification. Computers & Geosciences, 81, 101-113.

Yin, A. (1989). Origin of regional, rooted low-angle normal faults: A mechanical model and its tectonic implications. Tectonics, 8(3), 469-482.

Geochemistry, Geophysics, Geosystems

Supporting Information for

Slow-to-Fast Deformation in Mafic Fault Rocks on an Active Low-Angle Normal Fault, Woodlark Rift, SE Papua New Guinea

Marcel Mizera[1], Timothy Little[2], Carolyn Boulton[2], David Prior[3], Emma Watson[4], James Biemiller[5], Joseph White[6], Norio Shigematsu[7]

[1]Faculty of Geosciences, Utrecht University, Utrecht, The Netherlands.
[2]School of Geography, Environment and Earth Sciences, Victoria University of Wellington, Wellington, New Zealand.
[3]Department of Geology, University of Otago, Dunedin, New Zealand.
[4]GNS Science, Lower Hutt, New Zealand.
[5]Institute for Geophysics, Jackson School of Geosciences, University of Texas at Austin, Austin, Texas, USA.
[6]Department of Earth Sciences, University of New Brunswick, Fredericton, Canada.
[7]Research Institute Eathquake and Volcano Geology, Geological Survey of Japan, AIST.

Contents of this file

Additional Supporting Information (Files uploaded separately)

Table S9.1 ***(Albite_EPMA_Data.xlsx).*** Feldspar compositions in mafic mylonites and foliated cataclasites.
Table S9.2 ***(Chlorite_EPMA_data.xlsx).*** Chlorite compositions, calculated temperatures and proportions of chlorite to swelling component (X) in analysed mylonite, foliated cataclasites and chlorite veins.

Introduction

This Supporting Information provides bulk rock and mineral-specific compositional and microstructural data on metabasaltic fault rocks exhumed by the Mai'iu fault in the footwall of the Suckling-Dayman Metamorphic Core Complex. The supplementary data were obtained from several analytical techniques, including: (1) field emission gun scanning electron microscopy (FEG-SEM) including energy dispersive spectroscopy (EDS) and also electron backscatter diffractometry (EBSD) to quantify elemental compositions and crystallographic orientation data in collected fault rock samples; (2) temperature-dependent magnetic susceptibility experiments on a Bartington MS2 furnace system in order to determine the Curie temperature(s) of the constituent ferromagnetic/ferrimagnetic phase(s) and the magnetic mineralogy of an ultracataclasite sample; (3) transmission electron microscopy (TEM) to analyze the mirror polish of one fault-truncated dolerite cobble in order to describe the composition, thickness and grain-size of the shiny, fault-truncated surface, and the origin of striation on these surfaces; (4) X-Ray fluorescence (XRF) in order to determine major element bulk rock compositions of Goropu Metabasalt, a mylonite and two gouge samples; (5) X-Ray Diffractometry (XRD) to identify mineral phases in 15 fault rock samples comprising ultracataclasites and gouges; and (7) electron probe micro-analyzer (EPMA) to determine the chemical composition of chlorite and albite in mylonites and foliated cataclasites. Chlorite and albite compositions can be found in the separate files *'Chlorite_EPMA_data.xlsx'* and *'Albite_EPMA_Data.xlsx'*, respectively.

In addition to the presenting analytical results derived from these method in a series of Tables, we also present EDS-derived element and EBSD-derived phase maps; EBSD-derived pole figures showing crystallographic orientation distributions of the phases actinolite, epidote, titanite, and albite; and EBSD-derived grain-size statistics for these phases. The Supporting Information also includes optical photomicrographs and SEM imagery.

Text S1. EDS-based Elemental Compostions of Mafic Fault Rocks

Elemental compositions of whole thin section (~2x1 cm) are shown in Table S1.1. Elemental compositions of polyphase clasts in gouge samples are shown in Table S1.2 and Table S1.3. The elemental data shown in Table S1.1 of the different fault rock units indicate a decrease in sodium (Na) and an increase in potassium (K) in the ultracataclasites relative to the mylonite and foliated cataclasite samples. EDS-based elemental compositions of polyphase clasts in the gouges indicate that these clasts are similar in composition to the structurally underlying fault rocks (mylonite, cataclasite and ultracataclasite).

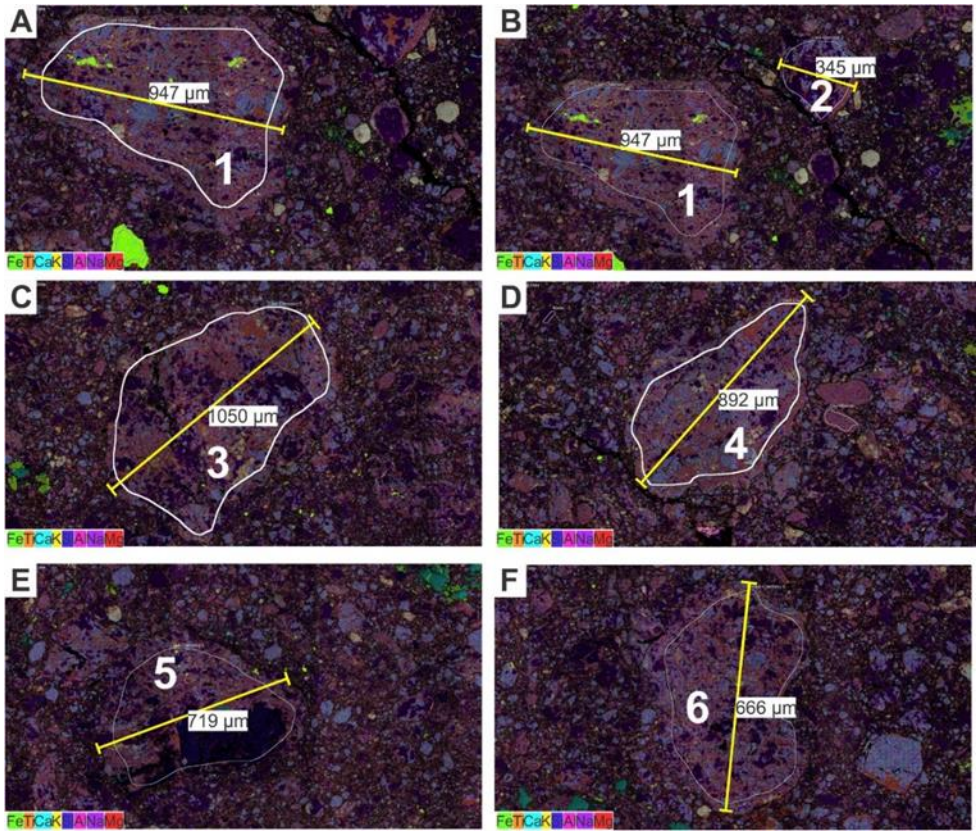

Figure S1.1. EDS-based layered elemental images of polyphase clasts embedded in fault gouge (PNG16-142A). Color scheme: iron (Fe)–green; titanium (Ti)–orange; calcium (Ca)–cyan; potassium (K)–yellow; silicon (Si)–blue; aluminium (Al)–pink; sodium (Na)–purple; magnesium (Mg)–red. Yellow scale bars in micrometers indicate diameter of polyphase clasts. A-F) Different sized polyphase clasts. EDS-based elemental compositions of these clasts are shown in Table S1.2. The elemental compositions of these clasts are similar to mylonites and foliated cataclasites. A) Polyphase clast (1). B) Polyphase clasts (1) and (2). C) Polyphase clast (3). D) Polyphase clast (4). E) Polyphase clast (5). F) Polyphase clast (6).

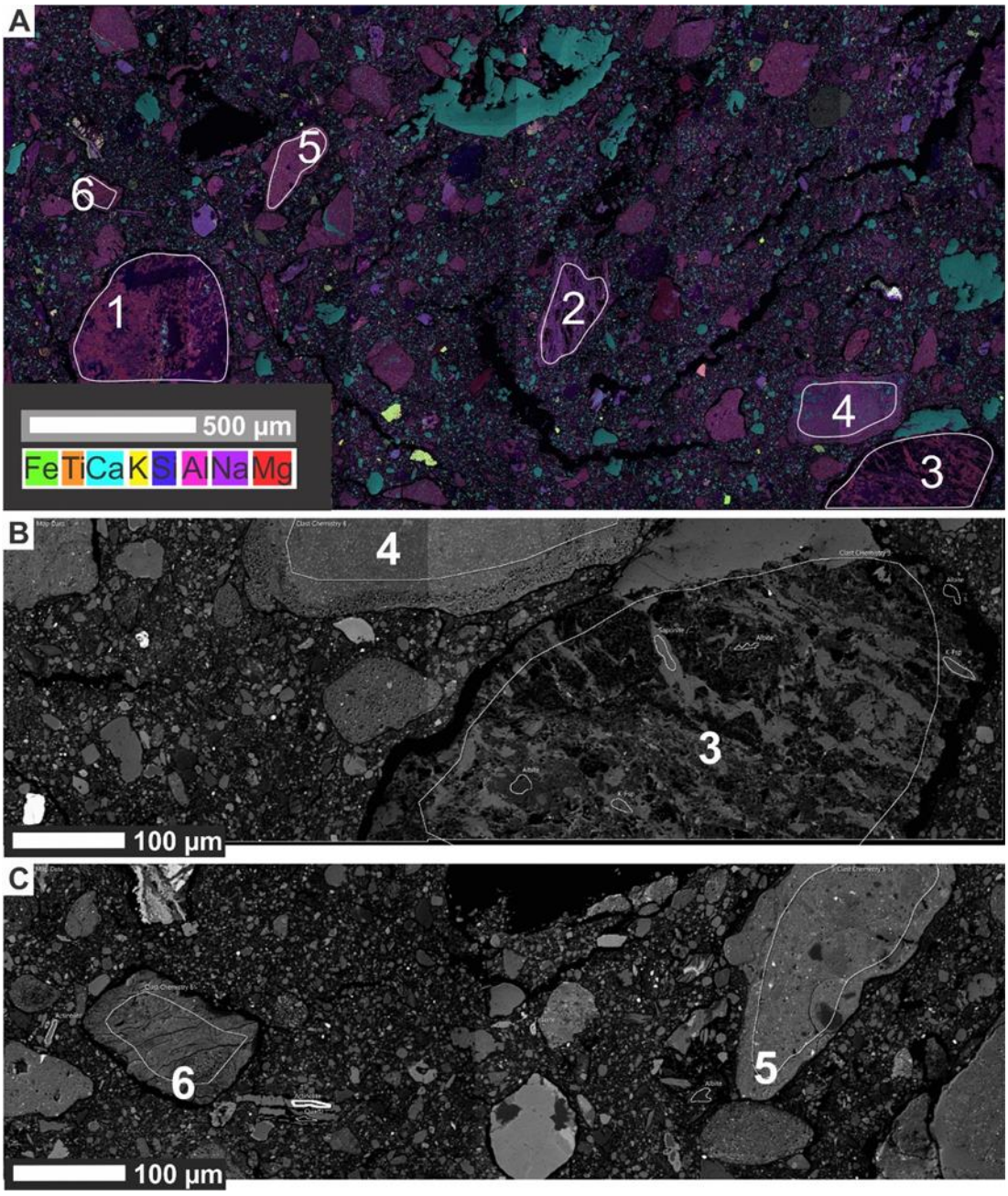

Figure S1.2. Layered elemental image and backscatter electron (BSE) images of polyphase clasts embedded in fault gouge (PNG16-142B). EDS-based elemental compositions of the analysed clasts are shown in Table S1.3. A) EDS-based layered elemental image. Clasts 1-3 are similar to mylonites and foliated cataclasites in elemental composition; clasts 4-6 are similar to ultracataclasites in elemental composition. Color scheme: iron (Fe)–green; titanium (Ti)–orange; calcium (Ca)–cyan; potassium (K)–yellow; silicon (Si)–blue; aluminium (Al)–pink; sodium (Na)–purple; magnesium (Mg)–red. B) BSE image of clast 3 and 4 (A). Clast 3 is a foliated cataclasite lithic fragment; clast 4 is a porous ultracataclasite lithic fragment. C) BSE image of clast 5 and 6 (A). Both clasts resemble the ultracataclasite in texture and composition.

Spectrum Label	Mylonite	Cataclasite	UCAT-D2	UCAT-D1	Green Gouge	Grey Gouge
	PNG16-142C	PNG16-142E	PNG16-142D2	PNG16-142D1	PNG16-142A	PNG16-142B
O	42.65	41.99	37.68	41.61	36.35	29.28
Na	2.23	2.71	0.47	0.52	2.08	0.72
Mg	4.57	3.23	4.38	4.36	3.41	3.41
Al	8.04	6.87	6.49	6.97	6.77	5.09
Si	22.55	21.14	20.26	21.31	19.13	14.68
K	0.18	0.23	4.62	5.39	0.2	1.29
Ca	8.46	9.6	4.96	5.44	6.15	7.59
Ti	0.64	0.84	1	1.04	1	0.61
Mn	0.15	0.17	0.12	0.12	0.14	0.13
Fe	7.35	7.18	7.44	7.36	8.12	6.19
Zn	0.13	0.16	0.04	0.03	0.13	0.05
Total	**96.95**	**94.17**	**87.48**	**94.16**	**83.65**	**69.27**

Table S1.1. EDS-based elemental compositions (wt%) of the different fault rock units (collected at the active Mai'iu fault trace, PNG16-142). Highlighted fields in the ultracataclasites show a strong elemental decrease (red) of Na and Ca and a strong increase (green) of K.

Green Gouge (PNG16-142A)

Spectrum Label	Clast-Chemistry 1	Clast-Chemistry 2	Clast-Chemistry 3	Clast-Chemistry 4	Clast-Chemistry 5	Clast-Chemistry 6
O	42.26	45.8	41.92	42.5	41.14	42.03
Na	1.58	5.57	2.56	1.58	1.57	2.01
Mg	3.71	1.69	3.73	3.49	3.03	3.58
Al	8.2	10.39	7.61	8.42	4.59	7.71
Si	19.27	26.14	21.18	19.43	27.25	21.34
K	0.14	0.13	0.29	0.16	0.2	0.3
Ca	8.47	3.94	6.49	8.84	4.42	7.43
Ti	1.3	0.17	1.21	1.37	0.53	1.04
Mn	0.16			0.12	0.13	0.14
Fe	10.4	5.6	8.35	9.92	6.25	8.63
Total	**96.08**	**99.42**	**93.35**	**95.84**	**89.19**	**94.19**

Table S1.2. EDS-based elemental composition (wt%) of polyphase clasts in a gouge sample (PNG16-142A), ~5 cm beneath the active Mai'iu fault plane. Analysed clasts are shown in the EDS maps of Figure S1.1 (see above).

Grey Gouge (PNG16-142B)

Spectrum Label	Clast Chemistry 1	Clast Chemistry 2	Clast CHemistry 3	Clast Chemistry 4	Clast Chemistry 5	Clast Chemistry 6
O	43.53	36.6	36.16	42.3	40.18	40.45
Na	3.73	1.13	2.73	1.31	0.66	0
Mg	3.54	3.71	3.87	1.75	4.41	6.8
Al	10.07	7.88	7.11	7.37	7.91	7.34
Si	22.52	16.69	20.66	23.45	21.74	19.65
K	0.08	0	1.49	6.19	5.66	3.88
Ca	2.39	7.38	2.1	8.07	2.01	2.59
Ti	1.02	1.33	1.21	0.57	1.06	0.74
Mn	0.16	0	0	0	0	0
Fe	7.8	7.54	5.68	3.03	9	8.67
Total	**94.84**	**82.43**	**81.22**	**94.04**	**92.63**	**90.12**

Table S1.3. EDS-based elemental compositions (wt%) of polyphase clasts in a gouge sample (PNG16-142B) immediately beneath the active Mai'iu fault plane. Analysed clasts are shown in the EDS map and SEM back-scatter image of Figure S1.2 (see above).

Text S2. Additional Backscatter Electron Images and EDS Maps of Mafic Fault Rocks

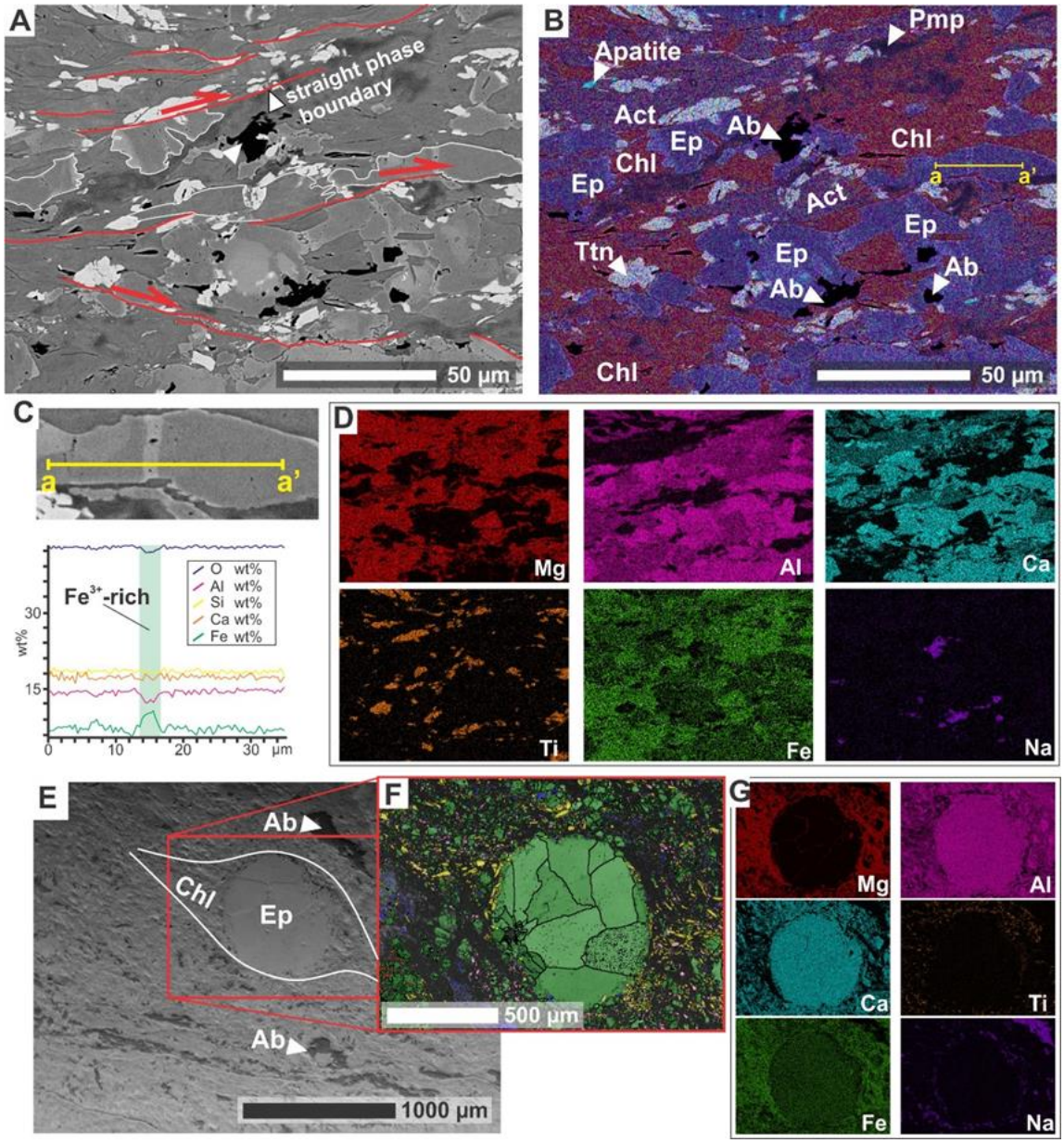

Figure S2.1. Mafic mylonite (PNG15-59A). Parts A, B, and D all depict the same part of this sample. Figures are arranged with the normal slip sense of the Mai'iu fault shown top-to-the-right. A) Backscatter electron (BSE) image of the fine-grained mylonitic matrix. Epidotes are zoned and have Fe-rich rims. B) Layered elemental image (individual element maps in D). Dark red colours highlights chlorite. Albite (dark "inkspots") appears in relation with epidote. C). Elemental-profile through epidote-clast. D) Individual element maps of the area in part (A) and (B). E) BSE image of epidote amygdule in fine-grained mafic matrix (same sample). F) EBSD phase map. Green–epidote; yellow–actinolite; blue–albite; pink–titanite. G) Element maps of the area in part (F). Dark red areas in the magnesium map correspond to chlorite, which we interpret to be neo-formed.

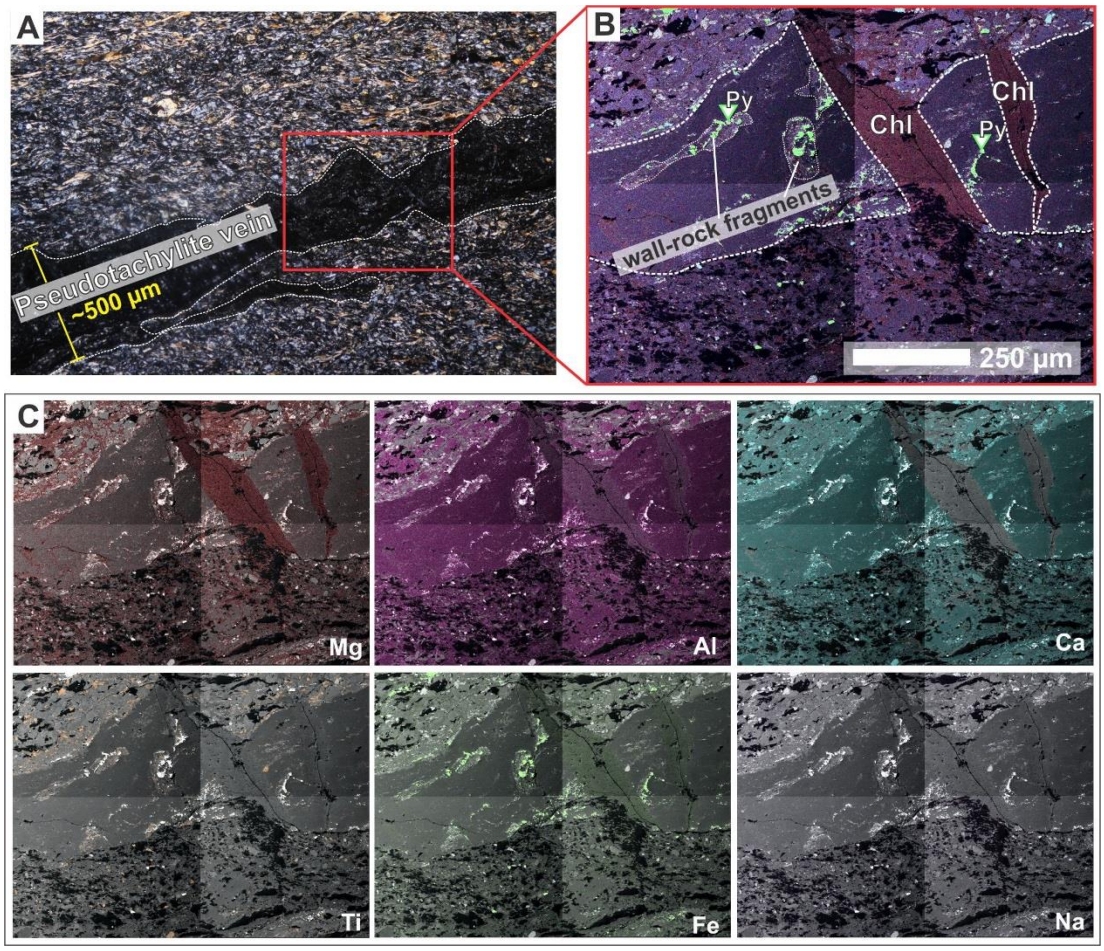

Figure S2.2. Pseudotachylite vein in mylonite sample (PNG16-142C). A) Optical photomicrograph (crossed polarizers). Yellow scale bar in micrometers indicates thickness of pseudotachylite vein. B) Layered elemental image of pseudotachylite vein with abundant pyrite (Py) grains and wall-rock fragments. Dark red areas cross-cutting the pseudotachylite vein indicate chlorite (Chl). C) EDS-based element maps for Mg, Al, Ca, Ti, Fe, and Na. Dark red areas in the magnesium map indicate chlorite.

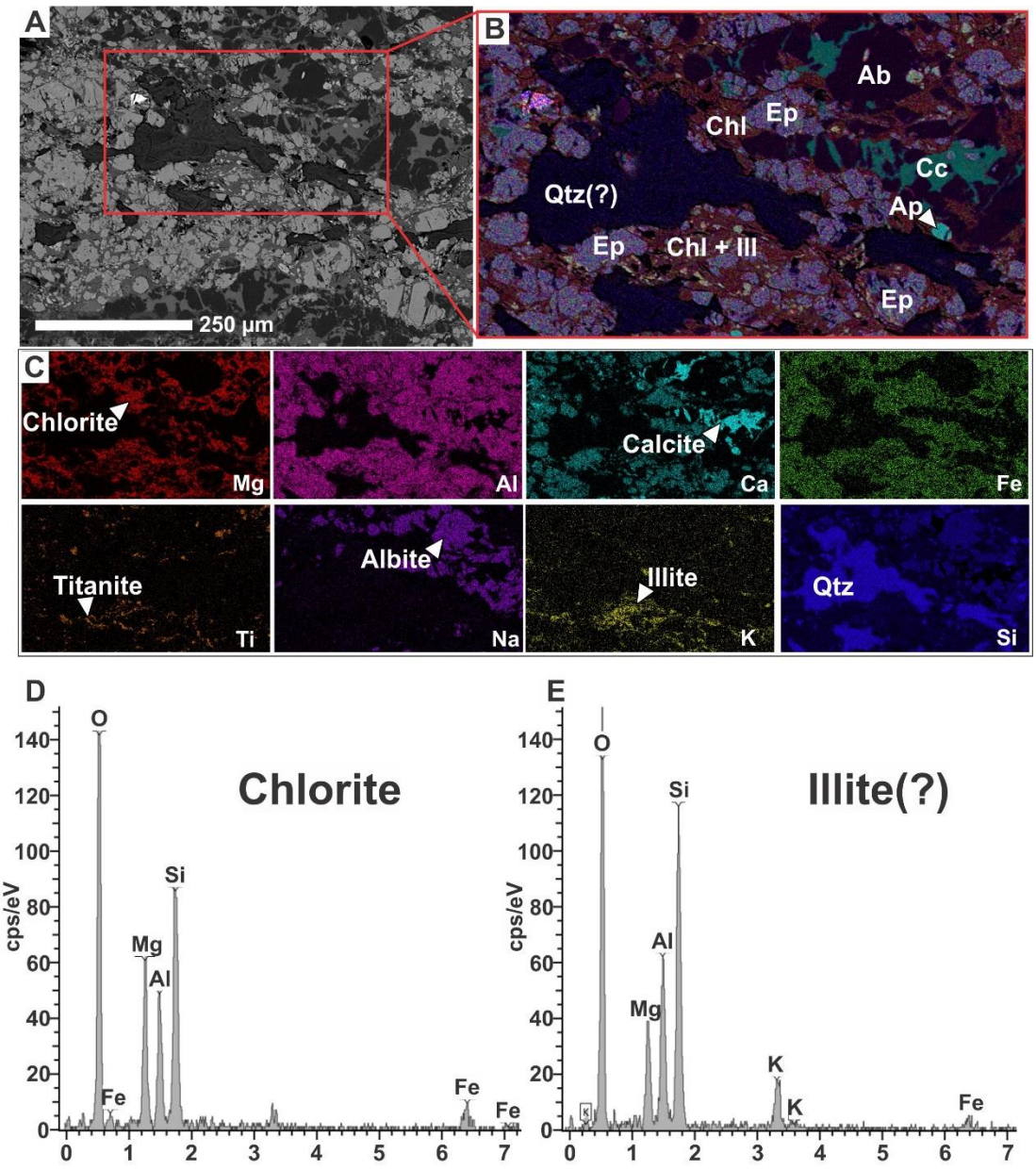

Figure S2.3. Foliated cataclasite (PNG16-17H). Figures are arranged with the normal slip sense of the Mai'iu fault shown top-to-the-right. A) Backscatter electron (BSE) image of dark folia in the cataclasite. B) Layered elemental image based on EDS analysis of the dark folia. Dark, brick red colours indicate chlorite. We infer that chlorite grew and was passively concentrated during a reaction that consumed epidote (purple colour) and actinolite (purple-red colour). C) Elemental maps for Mg, Al, Ca, Fe, Ti, Na, K and Si. D) and E) EDS spectra, respectively, of chlorite and presumably Illite. Note that the presence of 1Md and 2M1 illites in this sample was verified by XRD analyses (see Little et al., 2019).

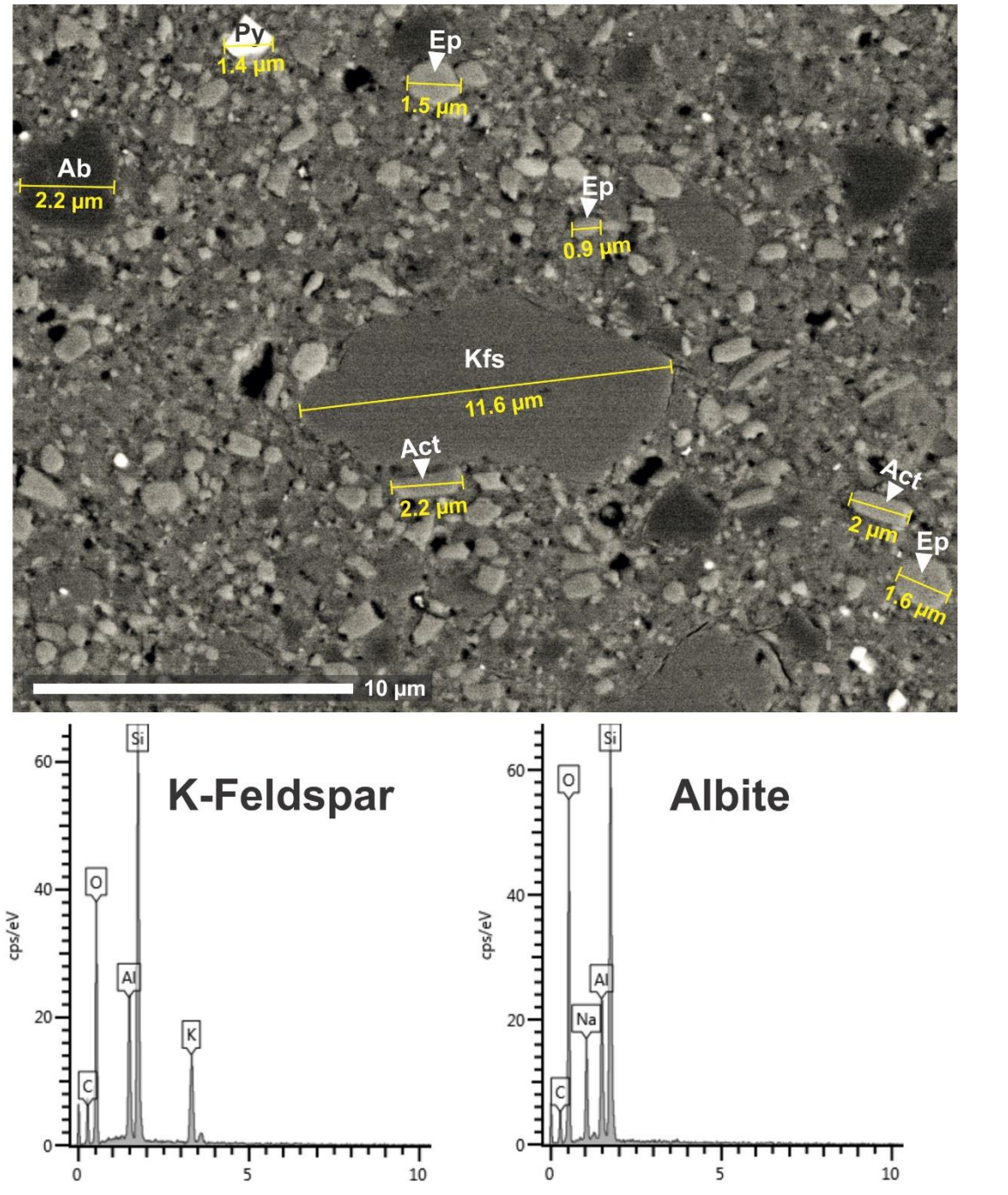

Figure S2.4. Sample PNG15-50DR: Backscatter electron (BSE) image of ultracataclasite and EDS spectra of albite and K-feldspar grains in the matrix. The BSE image includes yellow scale bars in micrometers that indicate the diameters of particular grains, including relict mafic lithic grains and K-feldspar grains.

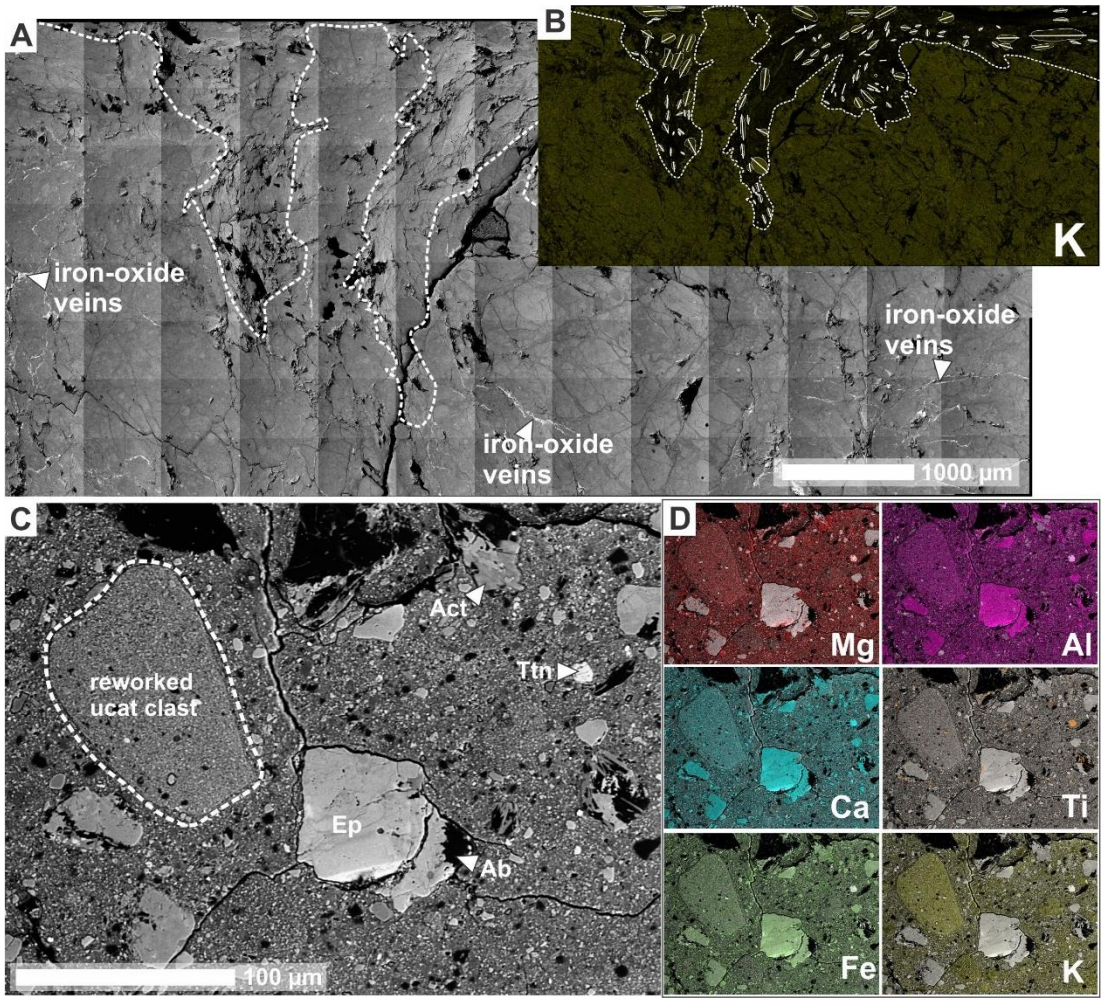

Figure S2.5. Backscatter electron (BSE) images and EDS maps of sample PNG16-142D2 (ultracataclasite). A) BSE image of the whole thin section. On this image, light-colored veins are iron-oxide veins. B) Potassium (K) map of (A) indicates elemental zonation (a K enriched domain—bottom; K depleted domain—top). White glyphs indicate orientation of long-axis of K-rich fragments in the K-depleted domain. C) Back-scatter image of ultracataclasite matrix. Older ultracataclasite-clasts are reworked in the matrix and show an apparent higher concentration of potassium relative to the surrounding matrix. D) Elemental maps for the same area as in C.

Text S3. EBSD Data Processing

Raw EBSD data were processed with the MTEX toolbox for MATLAB (Bachmann et al., 2010) after the approach of Cross (2015). In MTEX, raw EBSD data of indexed pixels are converted to grains based on a Voronoi decomposition method. The script populates the whole map area with grains (defined as areas encompassed by boundaries of >10° misorientation), whereas non-indexed phases are removed in a later step. Identified "grains" smaller than 2 x 2 pixels in size were removed from the acquired EBSD map as they are likely the result of misindexing. A smoothing factor of 2 was applied to the mapped grains. Furthermore, poorly constrained grains were removed based on the fraction of their area covered by raw data (f_i), (Cross, 2015):

$$f_i = \frac{n_i \cdot d_{step}^2}{A_{grain}}, \qquad \text{(Eq. S3.1)}$$

where n_i is the number of indexed pixels in a grain, d_{step} is the step size (width of each pixel), and A_{grain} is the area a grain covers based on the Voronoi decomposition. Because some fault rocks were poorly indexed (especially ultracataclasites, fault gouge, and weathered schists), a critical threshold value for f_i was estimated for every sample based on trade-off curves for the indexed fraction of grains versus the cumulative number of grains. The knee of this curve represents the threshold value between poorly constrained and well constrained grains (Cross, 2015). The grains that fall under the category "poorly constrained grains" were removed from the EBSD map. Step sizes and threshold values for f_i are given for each sample in Table S4.1 to Table S4.4 of S4 ('EBSD-based Fabric Strength and Grain-Size Estimates of Mafic Fault Rocks'). Fabric strength is herein quantified by calculating both the J-index of Bunge (2013) and the M-index of Skemer et al. (2005). The latter parameter measures the difference between the observed distribution of uncorrelated misorientation angles and the distribution of uncorrelated misorientation angles for a random fabric—the stronger the fabric, the greater the M-index ranging from 0 (random fabric) to 1 (single crystal; Skemer et al., 2005; Mainprice et al., 2015). All MTEX scripts for the data processing can be found in the contribution by Mizera (2019).

Text S4. EBSD-based Fabric Strength and Grain-Size Estimates of Mafic Fault Rocks

The following tables and figures summarize the results of the processed EBSD data from the different mafic fault rocks. The results presented in the following tables include mean grain size estimates and fabric strength of actinolite, epidote, albite and titanite in the different fault rock units. The tables are followed by figures of all analysed and processed EBSD maps starting with mafic mylonite samples and continuing with foliated cataclasite, ultracataclasite, gouge and non-mylonitic mafic schist. All crystallographic pole diagrams shown in these figures are Schmidt lower hemisphere equal-area projections.

Actinolite

Sample#	Rock Type	Domain	Tradeoff-Curve	Step Size (μm)	N_O	N_P	N_G	Mean GS	(1σ)	Min	Max	All Grains J (ODF)	All Grains J (MDF)	All Grains S	All Grains M	1 point per Grain J (ODF)	1 point per Grain J (MDF)	1 point per Grain S	1 point per Grain M
15-43	Mylonite	Mafic Matrix	0.4	2.0	80860	57671	523	25.0	±16	4.1	103.8	3.707	1.260	-0.851	0.105	2.762	1.179	-0.700	0.080
16-142C	Mylonite	Montaged Mafic Matrix	0.5	2.0	364636	303953	8140	13.4	±8.6	3.3	117.9	5.317	1.856	-1.097	0.225	4.796	1.708	-0.995	0.204
15-52A	Mylonite	Mafic Matrix	0.3	2.0	44740	29633	433	22.2	±14	5.3	96.9	8.628	2.649	-1.547	0.300	8.013	2.537	-1.498	0.291
16-17E	Mylonite	Mafic Matrix	0.4	1.0	61041	27372	587	9.1	±5	2.3	38.2	1.768	1.058	-0.325	0.041	1.812	1.056	-0.349	0.038
15-73A	Mylonite	Whole Sample	0.5	1.0	275101	163625	2359	10.2	±5.7	2.0	64.5	8.172	2.785	-1.514	0.317	7.838	2.769	-1.508	0.291
15-73A	Mylonite	Actinolite Layer	0.5	1.0	208327	153596	1916	10.7	±6	2.2	64.9	9.217	3.127	-1.649	0.346	8.558	3.092	-1.628	0.316
15-73A	Mylonite	Fine Grained Matrix	0.5	1.0	77930	37409	763	8.7	±4.7	2.0	35.7	6.438	2.132	-1.257	0.261	6.575	2.096	-1.263	0.246
15-59A	Mylonite	Mafic Matrix	0.5	2.0	625853	532722	14657	12.7	±8.7	3.3	162.2	2.479	1.181	-0.515	0.087	2.184	1.122	-0.421	0.072
15-59A	Mylonite	Mafic Matrix	0.4	5.0	34121	19267	1606	23.3	±11	10.0	120.4	3.546	1.430	-0.800	0.149	3.656	1.452	-0.822	0.151
15-59A	Mylonite	Mafic Matrix	0.3	5.0	21434	16443	1335	23.3	±9.6	10.0	97.4	4.320	1.656	-0.984	0.181	4.487	1.687	-1.001	0.185
15-59A	Mylonite	Dark Matrix	0.3	5.0	5681	3585	281	25.0	±9.8	9.2	65.1	3.492	1.335	-0.779	0.139	3.543	1.317	-0.813	0.142
16-125B	Cataclasite	Mafic Matrix	0.3	1.0	25779	17011	262	10.3	±7.4	2.0	70.1	6.814	1.590	-1.050	0.194	4.214	1.280	-0.846	0.144
16-125B	Cataclasite	Mafic Matrix	0.2	0.5	8798	6471	89	7.3	±4.8	1.0	18.4								
16-142E	Cataclasite	Montaged Mafic Matrix	0.5	2.0	239868	189670	5296	12.7	±8.7	3.6	107.8	1.621	1.034	-0.272	0.051	1.523	1.028	-0.233	0.045
16-142E	Ultramylonite	Ultramylonite Layer	0.5	2.0	2900	2227	119	9.1	±4.4	3.3	29.7	2.508	1.021	-0.498	0.022	2.070	1.014	-0.478	0.021
15-50E	Cataclasite	Mafic Matrix	0.3	1.0	15082	9090	149	11.5	±5.8	2.4	37.7	3.551	1.313	-0.783	0.145	3.014	1.157	-0.702	0.093
16-50RD	Cataclasite	Mafic Matrix	0.3	2.0	24298	12356	236	22.1	±11	5.5	61.2	2.152	1.056	-0.410	0.062	2.117	1.043	-0.441	0.051
16-151E	Cataclasite	Dark Matrix	0.4	1.0	71118	54041	1465	7.4	±4.2	1.8	48.5	4.792	1.615	-0.957	0.212	4.653	1.615	-0.935	0.200
16-151E	Cataclasite	Dark Matrix	0.4	2.0	20381	12054	373	13.3	±8.8	4.2	95.7	4.686	1.382	-0.961	0.157	5.017	1.560	-0.988	0.196

Table S4.1 (continued).

											All Grains				1 point per Grain			
Sample#	Rock Type	Domain	Tradeoff-Curve	Step Size (μm)	N_O	N_P	N_G	Mean GS	(1σ)	Min	Max	J (ODF)	J (MDF)	S	M	J (ODF)	J (MDF)	S	M
16-125A	Ultracataclasite	UCAT matrix	0.1	0.5	136359	1715	141	2.3	±0.9	1.3	12.8	1.102	1.000	-0.049	0.003	1.798	1.007	-0.378	0.016
16-142D	Ultracataclasite	UCAT matrix	0.2	0.6	27443	334	27	2.5	±1.1	1.8	10.0	4.019	1.053	-0.738	0.034	14.575	2.477	2.477	0.212
16-142B	Gouge	Matrix	0.3	0.6	28686	8103	250	3.5	±2.5	1.2	22.9	1.256	1.001	-0.098	0.005	1.641	1.013	-0.300	0.018
16-142A	Gouge	Matrix	0.4	0.5	156216	77242	1368	3.8	±2.8	1.0	39.9	1.234	1.001	-0.094	0.006	1.121	1.001	-0.058	0.004
16-126A	Schist/Mylonite?	Mafic Matrix	0.3	0.8	190428	120029	726	12.9	±8.1	1.4	68.6	3.276	1.300	-0.725	0.115	2.747	1.222	-0.625	0.093
16-126B	Schist	Mafic Matrix	0.35	1.5	45274	21704	754	11.3	±5.9	3.2	52.3	2.257	1.127	-0.469	0.071	2.313	1.128	-0.487	0.076
16-169	Schist	Mafic Matrix	0.3	1.5	98667	79461	1918	11.9	±7.9	2.9	80.6	3.305	1.382	-0.771	0.108	3.188	1.358	-0.742	0.114
16-176	Schist	Mafic Matrix	0.3	2.0	40561	12060	288	19.3	±11	4.6	81.5	4.394	1.661	-0.978	0.163	4.849	1.792	-1.116	0.165
16-182	Schist/Mylonite?	Mafic Matrix	0.3	2.0	150845	109770	1042	25.7	±19	3.6	157.5	3.544	1.418	-0.829	0.127	3.939	1.650	-0.923	0.151

Table S4.1. EBSD-derived grain-size statistics and fabric strengths (J-index, S-index and M-index) for actinolite. N_O—number of orientations; N_P—number of pixels; N_G—number of grains; Mean GS—mean grain size; 1σ—standard deviation; Min, Max—minimum and maximum measured grain sizes, respectively.

Epidote

Sample#	Rock Type	Domain	Tradeoff-Curve	Step Size (µm)	N_O	N_P	N_G	Mean GS	(1σ)	Min	Max	All Grains J (ODF)	All Grains J (MDF)	All Grains S	All Grains M	1 point per Grain J (ODF)	1 point per Grain J (MDF)	1 point per Grain S	1 point per Grain M
15-43	Mylonite	Mafic Matrix Montaged	0.4	2.0	36874	15459	320	19.0	±8.8	3.7	48.5	1.388	1.009	-0.171	0.030	1.555	1.009	-0.247	0.032
16-142C	Mylonite	Mafic Matrix	0.5	2.0	400404	380064	2770	22.8	±18	3.6	135.8	2.376	1.183	-0.546	0.136	2.062	1.126	-0.424	0.118
15-52A	Mylonite	Mafic Matrix	0.3	2.0	52085	30822	549	23.2	±10	4.1	61.7	2.157	1.122	-0.447	0.114	2.301	1.167	-0.520	0.136
16-17E	Mylonite	Mafic Matrix	0.4	1.0	667540	512312	5383	12.0	±7.1	1.7	87.5	1.093	1.000	-0.045	0.007	1.079	1.000	-0.040	0.007
15-73A	Mylonite	Whole Sample	0.5	1.0	102747	60270	327	13.8	±9.4	2.2	77.1	2.193	1.025	-0.376	0.048	1.586	1.016	-0.284	0.041
15-73A	Mylonite	Actinolite Layer	0.5	1.0	24870	18773	66	15.1	±11	2.8	78.4	6.067	1.143	-0.950	0.071	2.702	1.036	-0.696	0.049
15-73A	Mylonite	Fine Grained Matrix	0.5	1.0	80935	47727	305	13.4	±7.9	2.2	74.7	2.437	1.032	-0.395	0.052	1.581	1.015	-0.286	0.040
15-59A	Mylonite	Mafic Matrix	0.5	2.0	623947	598470	4035	21.8	±20	3.3	223.8	1.204	1.001	-0.091	0.008	1.057	1.000	-0.029	0.004
15-59A	Mylonite	Mafic Matrix	0.4	5.0	50459	38023	1472	31.2	±19	10.4	170.6	1.283	1.004	-0.128	0.019	1.202	1.004	-0.096	0.020
15-59A	Mylonite	Mafic Matrix	0.3	5.0	18985	17722	682	30.1	±17	11.3	172.7	1.655	1.004	-0.249	0.014	1.295	1.004	-0.140	0.021
15-59A	Mylonite	Mafic Matrix	0.3	5.0	24119	20831	776	33.2	±18	12.2	170.8	1.660	1.016	-0.276	0.036	1.429	1.014	-0.192	0.038
16-142E	Cataclasite	Mafic Matrix Montaged	0.5	2.0	190620	153614	3254	14.8	±9.6	3.6	115.1	1.160	1.001	-0.075	0.010	1.109	1.001	-0.053	0.008
15-50E	Cataclasite	Mafic Matrix	0.3	1.0	32839	29326	134	18.7	±10	3.7	60.4	2.589	1.019	-0.569	0.031	1.925	1.013	-0.422	0.039
16-50RD	Cataclasite	Mafic Matrix	0.3	2.0	29596	19683	277	26.2	±11	5.8	63.9	1.324	1.001	-0.148	0.007	1.399	1.002	-0.188	0.013
16-151E	Cataclasite	Dark Matrix	0.4	2.0	65694	35518	821	17.1	±9	4.5	76.4	1.197	1.001	-0.094	0.009	1.229	1.002	-0.110	0.012

Table S4.2 (continued)

Sample#	Rock Type	Domain	Tradeoff-Curve	Step Size (μm)	N_O	N_P	N_G	Mean GS	(1σ)	Min	Max	All Grains J (ODF)	All Grains J (MDF)	All Grains S	All Grains M	1 point per Grain J (ODF)	1 point per Grain J (MDF)	1 point per Grain S	1 point per Grain M
16-125A	Ultracataclasite	UCAT Matrix	0.1	0.5	100167	237	37	1.6	±0.5	1.0	3.0	1.415	1.007	-0.168	0.021	6.282	1.159	-1.279	0.056
16-142D	Ultracataclasite	UCAT Matrix	0.2	0.6	24865	4116	164	3.0	±2.1	1.2	14.0	1.260	1.002	-0.116	0.005	1.503	1.002	-0.242	0.006
16-142B	Gouge	Matrix	0.3	0.6	30410	12664	244	3.7	±3	1.1	18.7	1.441	1.002	-0.169	0.006	1.586	1.004	-0.264	0.013
16-142A	Gouge	Matrix	0.4	0.5	221658	151589	2351	3.9	±3.1	0.7	56.6	1.275	1.001	-0.099	0.003	1.201	1.001	-0.096	0.006
16-126B	Schist	Mafic Matrix	0.4	1.5	213165	189910	1116	20.3	±14	2.7	148.7	3.953	1.065	-0.499	0.066	1.478	1.008	-0.176	0.029
16-182	Schist/Mylonite?	Mafic Matrix	0.3	2.0	164960	121725	1188	27.1	±16	3.9	180.0	1.372	1.006	-0.165	0.024	1.319	1.008	-0.149	0.029
15-72A	Schist	Mafic Matrix	0.5	2.0	119483	109578	1733	16.2	±12	3.7	109.8	1.832	1.045	-0.340	0.067	1.721	1.052	-0.305	0.068

Table S4.2. EBSD-based grain-size statistics and fabric strengths (J-index, S-index and M-index) for epidote. N_O—number of orientations; N_P—number of pixels; N_G—number of grains; Mean GS—mean grain size; 1σ—standard deviation; Min, Max—minimum and maximum measured grain sizes, respectively.

Albite

Sample#	Rock Type	Domain	Tradeoff-Curve	Step Size (μm)	N_O	N_P	N_G	Mean GS	(1σ)	Min	Max	All Grains J (ODF)	All Grains J (MDF)	All Grains S	All Grains M	1 point per Grain J (ODF)	1 point per Grain J (MDF)	1 point per Grain S	1 point per Grain M
15-43	Schist	Mafic Matrix	0.4	2.0	170016	120357	2415	16.7	±11.0	3.6	99.8	1.814	1.023	-0.323	0.031	1.745	1.017	-0.309	0.027
16-142C	Mylonite	Montaged Mafic Matrix	0.5	2.0	108869	87195	2368	13.0	±8.6	3.3	66.6	1.443	1.008	-0.206	0.017	1.340	1.004	-0.171	0.013
15-52A	Mylonite	Mafic Matrix	0.3	2.0	22353	16053	227	21.7	±14.0	3.6	83.8	3.138	1.040	-0.675	0.036	2.520	1.029	-0.622	0.030
16-17E	Mylonite	Matrix	0.4	1.0	454765	222597	5336	8.5	±4.6	1.8	61.5	1.418	1.013	-0.219	0.022	1.539	1.022	-0.277	0.028
15-59A	Mylonite	Mafic Matrix	0.5	2.0	5753	4914	118	12.5	±9.3	3.6	56.8	21.897	3.987	-2.102	0.326	13.885	2.237	-1.812	0.211
15-59A	Mylonite	Mafic Matrix	0.4	5.0	8296	5187	256	28.5	±19.0	9.7	99.9	2.470	1.015	-0.515	0.019	2.178	1.017	-0.517	0.025
15-59A	Mylonite	Mafic Matrix	0.3	5.0	4670	3956	190	25.9	±14.0	11.2	85.4	4.961	1.081	-0.909	0.035	2.721	1.026	-0.667	0.027
16-125B	Cataclasite/Ultramylonite	Mafic Matrix	0.3	1.0	50774	38749	732	8.7	±6.5	1.8	46.7	1.984	1.009	-0.369	0.019	1.712	1.007	-0.319	0.017
16-125B	Cataclasite/Ultramylonite	Mafic Matrix	0.2	0.5	272017	213089	1770	6.8	±6.9	0.8	55.8	1.781	1.007	-0.300	0.017	1.656	1.006	-0.273	0.013
16-142E	Cataclasite	Montaged Mafic Matrix	0.5	2.0	238202	172818	3692	14.4	±11.0	3.3	106.1	1.491	1.011	-0.226	0.023	1.370	1.007	-0.191	0.018
16-142E	Ultramylonite	Ultramylonite Layer	0.5	2.0	1967	1241	84	9.9	±3.9	4.4	22.4	3.115	1.030	-0.722	0.027	3.651	1.042	-0.954	0.026
15-50E	Cataclasite	Mafic Matrix	0.3	1.0	69721	58896	360	13.1	±12.0	1.8	67.7	3.599	1.069	-0.764	0.041	2.520	1.023	-0.562	0.028
16-50RD	Cataclasite	Mafic Matrix	0.3	2.0	22338	15439	295	18.9	±13.0	3.6	65.5	2.594	1.028	-0.539	0.031	3.198	1.029	-0.653	0.024
16-151E	Cataclasite	Dark Matrix	0.4	1.0	268945	232190	2483	10.4	±7.8	1.8	56.9	1.429	1.005	-0.204	0.015	1.318	1.003	-0.164	0.011
16-151E	Cataclasite	Dark Matrix	0.4	2.0	89562	63191	1428	16.6	±9.4	3.3	74.9	1.550	1.009	-0.255	0.022	1.453	1.008	-0.230	0.020
16-125A	Ultracataclasite	UCAT Matrix	0.3	0.5	6412	3044	163	2.5	±1.5	1.0	10.3	2.114	1.008	-0.340	0.014	2.846	1.023	-0.711	0.028

Table S4.3 (continued)

Sample#	Rock Type	Domain	Tradeoff-Curve	Step Size (μm)	N_O	N_P	N_G	Mean GS	(1σ)	Min	Max	All Grains J (ODF)	All Grains J (MDF)	All Grains S	All Grains M	1 point per Grain J (ODF)	1 point per Grain J (MDF)	1 point per Grain S	1 point per Grain M
16-142D	Ultracataclasite	UCAT Matrix	0.2	0.6	2497	944	114	2.1	±0.8	1.1	5.6	1.929	1.007	-0.324	0.012	3.608	1.046	-0.886	0.026
16-142B	Gouge	Matrix	0.3	0.6	17292	13270	508	2.9	±2.4	1.1	16.8	3.595	1.040	-0.682	0.024	2.416	1.011	-0.493	0.012
16-142A	Gouge	Matrix	0.4	0.5	47391	35808	1081	2.8	±2.3	0.9	20.0	2.412	1.021	-0.464	0.025	2.065	1.007	-0.385	0.009
16-126A	Schist/Mylonite?	Mafic Matrix	0.3	0.8	166814	114747	1312	8.7	±6.6	1.3	68.6	1.736	1.012	-0.284	0.021	1.633	1.011	-0.284	0.019
16-126B	Schist	Mafic Matrix	0.4	1.5	39122	22449	623	11.5	±7.2	2.5	41.4	1.645	1.008	-0.285	0.016	1.728	1.011	-0.334	0.019
16-169	Schist	Mafic Matrix	0.3	1.5	110051	78042	2168	12.2	±7.0	2.7	65.6	1.510	1.004	-0.226	0.012	1.408	1.004	-0.200	0.014
16-176	Schist	Mafic Matrix	0.3	2.0	11691	4851	130	17.8	±9.0	4.8	49.4	2.197	1.013	-0.441	0.017	3.107	1.033	-0.801	0.024
16-182	Schist/Mylonite?	Mafic Matrix	0.3	2.0	50956	25171	367	24.5	±14.0	4.0	94.2	2.229	1.061	-0.515	0.050	2.673	1.105	-0.691	0.065
15-72A	Schist	Mafic Matrix	0.5	2.0	96519	75656	2593	12.3	±7.0	3.3	57.9	1.503	1.010	-0.230	0.021	1.413	1.007	-0.203	0.019

Table S4.3. EBSD-based grain-size statistics and fabric strengths (J-index, S-index and M-index) for albite. N_O—number of orientations; N_P—number of pixels; N_G—number of grains; Mean GS—mean grain size; 1σ—standard deviation; Min, Max—minimum and maximum measured grain sizes, respectively.

Titanite

Sample#	Rock Type	Domain	Tradeoff-Curve	Step Size (μm)	N_O	N_P	N_G	Mean GS	(1σ)	Min	Max	All Grains J (ODF)	All Grains J (MDF)	All Grains S	All Grains M	1 point per Grain J (ODF)	1 point per Grain J (MDF)	1 point per Grain S	1 point per Grain M
16-142C	Mylonite	Montaged Mafic Matrix	0.5	2.0	43512	35236	1211	12.2	7.0	3.3	56.9	2.318	1.171	-0.507	0.096	2.044	1.133	-0.429	0.085
15-52A	Mylonite	Mafic Matrix	0.3	2.0	4023	1233	73	13.1	5.1	4.7	30.9	2.357	1.129	-0.591	0.087	3.366	1.179	-0.914	0.114
15-73A	Mylonite	Mafic Matrix	0.5	1.0	182312	73344	2114	7.8	3.4	2.0	30.2	2.023	1.144	-0.412	0.080	2.141	1.165	-0.453	0.085
15-73A	Mylonite	Mafic Matrix	0.5	1.0	36330	18659	447	8.3	3.4	2.4	22.7	2.787	1.340	-0.658	0.118	3.576	1.570	-0.873	0.151
15-73A	Mylonite	Fine Grained Matrix	0.5	1.0	148002	60466	1791	7.6	3.3	2.0	30.4	1.892	1.112	-0.371	0.071	1.959	1.123	-0.399	0.074
16-17E	Mylonite	Mafic Matrix	0.4	1.0	24395	5565	336	5.8	2.5	1.9	15.0	1.157	1.002	-0.075	0.010	1.373	1.002	-0.179	0.011
15-59A	Mylonite	Mafic Matrix	0.5	2.0	85909	62208	3350	10.5	4.8	3.3	43.5	1.473	1.033	-0.209	0.038	1.404	1.024	-0.181	0.032
15-59A	Mylonite	Mafic Matrix	0.4	5.0	2488	177	34	16.4	2.8	12.0	23.8	1.380	1.013	-0.179	0.025	4.372	1.200	-1.149	0.091
15-59A	Mylonite	Mafic Matrix	0.3	5.0	723	96	19	17.0	3.3	12.0	25.5	1.723	1.031	-0.338	0.043	5.582	1.282	-1.366	0.109
15-59A	Ultramylonite?	Mafic Matrix	0.3	5.0	1028	81	16	18.8	3.7	13.7	25.6	1.485	1.009	-0.219	0.021	7.436	1.620	-1.645	0.194
16-142E	Cataclasite	Montaged Mafic Matrix	0.5	2.0	17517	9227	642	9.1	4.3	3.3	44.4	1.279	1.004	-0.123	0.010	1.314	1.006	-0.158	0.011
16-142E	Ultramylonite	Ultramylonite Layer	0.5	2.0	460	230	22	8.0	3.2	4.5	15.6	3.301	1.053	-0.756	0.035	5.334	1.171	-1.299	0.057
15-50E	Cataclasite	Mafic Matrix	0.3	1.0	1961	1051	30	9.2	4.5	2.4	18.4	3.194	1.056	-0.672	0.041	3.557	1.034	-0.922	0.021
16-50RD	Cataclasite	Mafic Matrix	0.3	2.0	3161	781	39	13.8	6.4	5.6	34.0	1.594	1.003	-0.263	0.009	3.415	1.060	-0.935	0.060
16-151E	Cataclasite	Mafic Matrix	0.4	1.0	6824	3288	169	5.9	2.5	1.9	16.2	1.746	1.027	-0.310	0.037	1.832	1.028	-0.377	0.037
16-151E	Cataclasite	Mafic Matrix	0.4	2.0	1776	356	36	9.2	3.2	4.8	17.8	1.887	1.024	-0.351	0.038	3.747	1.076	-0.991	0.045

Table S4.4 (continued)

											All Grains				1 point per Grain			
Sample#	**Rock Type**	**Domain**	**Tradeoff-Curve**	**Step Size (μm)**	**N_O**	**N_P**	**N_G**	**Mean GS**	**(1σ)**	**Min**	**Max**	**J (ODF)**	**J (MDF)**	**S**	**M**	**J (ODF)**	**J (MDF)**	**S**	**M**
16-125A	Ultracataclasite	UCAT Matrix	0.3	0.5	57747	463	49	2.1	0.6	1.1	3.5	1.191	1.002	-0.089	0.006	2.649	1.022	-0.698	0.022
16-142D	Ultracataclasite	UCAT Matrix	0.2	0.6	12604	932	109	2.2	0.8	1.2	4.9	1.199	1.002	-0.091	0.009	1.809	1.005	-0.383	0.016
16-142B	Gouge	Matrix	0.3	0.6	10744	1889	118	2.7	1.4	1.2	8.3	1.215	1.002	-0.099	0.008	1.796	1.007	-0.364	0.016
16-142A	Gouge	Matrix	0.4	0.5	59202	26103	1266	2.6	1.5	0.9	16.6	1.140	1.000	-0.064	0.005	1.095	1.000	-0.047	0.002
16-126A	Schist/Mylonite?	Mafic Matrix	0.3	0.8	40846	12956	321	7.6	3.7	1.8	25.5	1.309	1.009	-0.145	0.021	1.455	1.011	-0.219	0.027
16-126B	Schist	Mafic Matrix	0.4	1.5	20265	6685	389	9.3	4.2	3.2	31.9	1.445	1.022	-0.201	0.039	1.538	1.019	-0.256	0.036
PNG16-169	Schist	Mafic Matrix	0.3	1.5	4948	1236	114	7.5	2.8	3.5	14.6	1.249	1.001	-0.116	0.007	1.890	1.014	-0.420	0.030
16-182	Schist/Mylonite?	Mafic Matrix	0.3	2.0	10012	2115	118	13.5	5.5	5.0	32.7	1.475	1.016	-0.227	0.029	2.148	1.022	-0.493	0.032
15-72A	Schist	Mafic Matrix	0.5	2.0	5904	1401	168	7.1	3.3	3.7	37.8	1.427	1.011	-0.186	0.029	1.838	1.024	-0.385	0.045

Table S4.4. EBSD-based grain-size statistics and fabric strengths (J-index, S-index and M-index) for titanite. N_O—number of orientations; N_P—number of pixels; N_G—number of grains; Mean GS—mean grain size; 1σ—standard deviation; Min, Max—minimum and maximum measured grain sizes, respectively.

Mafic Mylonites:

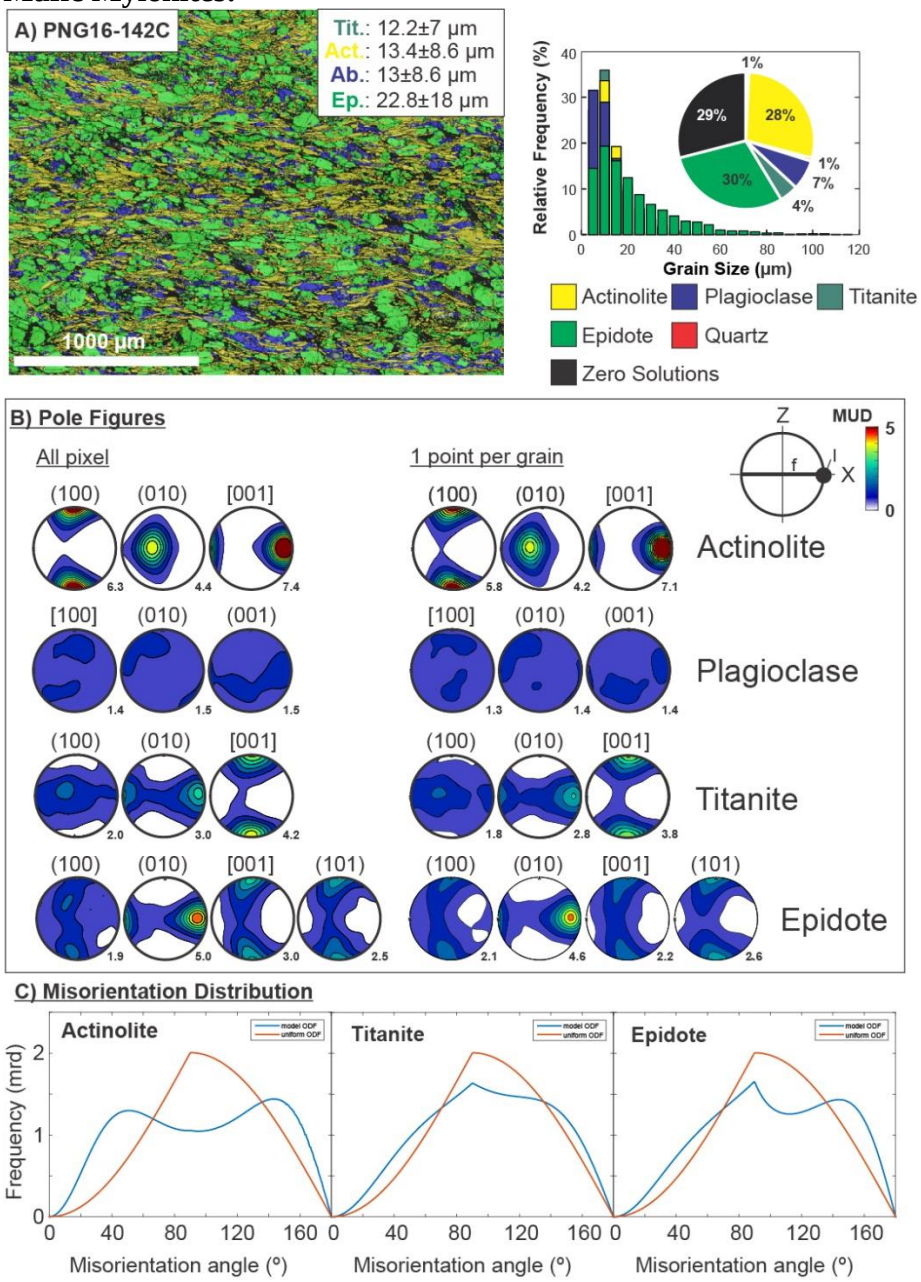

Figure S4.1. EBSD data for mylonite sample PNG16-142C (exhumed beneath active Mai'iu fault). A) EBSD-based phase map (2 µm step size) of the mylonite sample and average grain sizes of titanite, actinolite, epidote and albite (left-hand site); grain-size histogram (relative frequency[%] vs. grain size [µm]) and phase fraction (%; pie diagram) of selected minerals (right-hand side). B) Contoured pole figures of selected crystallographic axes and poles; left—based on all pixels; right—based on one point per grain. MUD—Multiples of uniform distribution; l—lineation; f—foliation. C) Misorientation distribution plot (misorientation angle versus frequency [mrd=multiples of random density]) of selected minerals for uncorrelated grains (blue curves), and a theoretical random distribution (red curves). ODF—Orientation density functions.

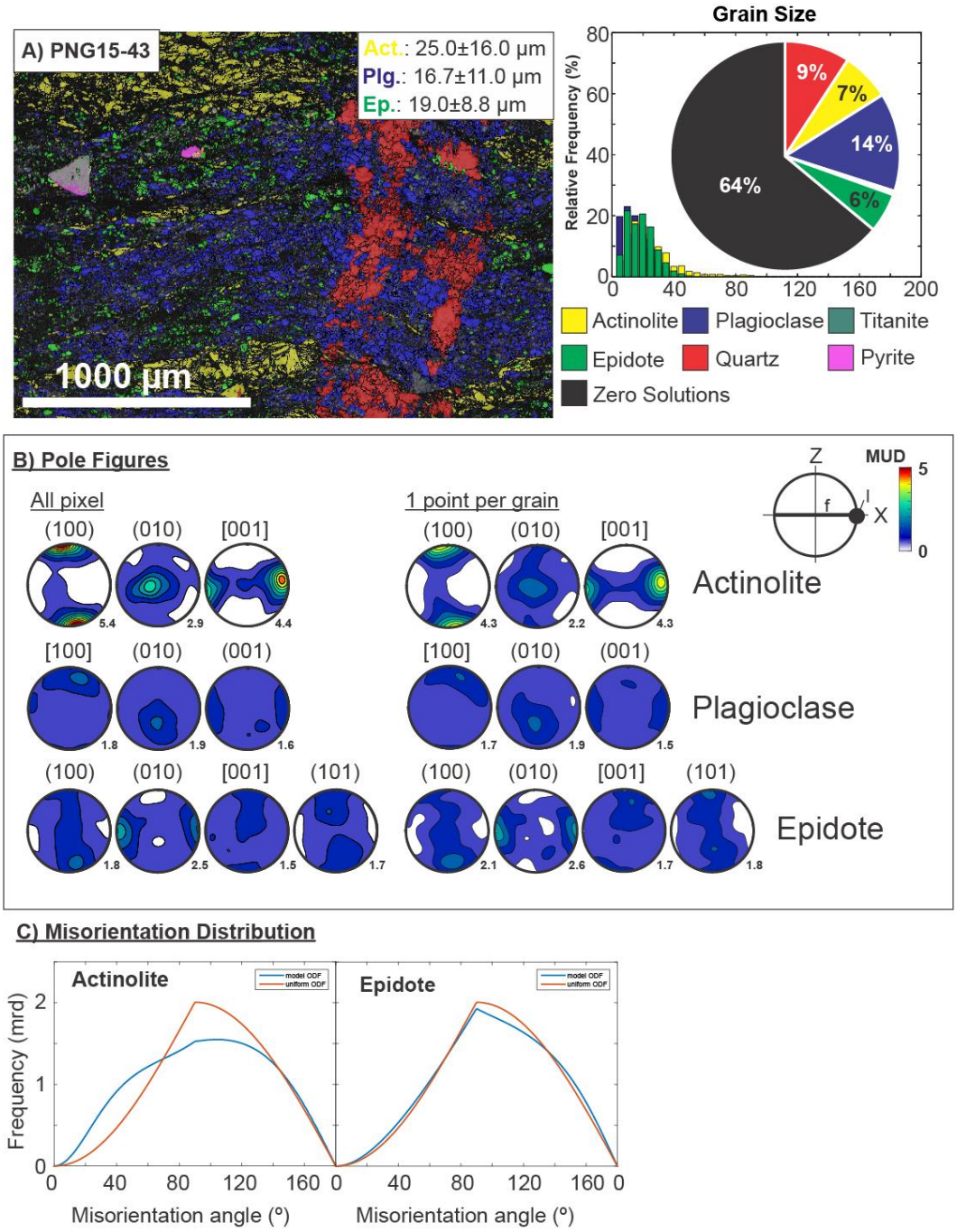

Figure S4.2. EBSD data for mylonite sample PNG15-43 (~700 m south of the active Mai'iu fault trace). A) EBSD-based phase map (2 µm step size) and average grain sizes of actinolite, epidote and albite (left-hand site); grain-size histogram (relative frequency[%] vs. grain size [µm]) and phase fraction (%; pie diagram) of selected minerals (right-hand side). B) Contoured pole figures of selected crystallographic axes and poles; left—based on all pixels; right—based on one point per grain. MUD—Multiples of uniform distribution; l—lineation; f—foliation. C) Misorientation distribution plot (misorientation angle versus frequency [mrd=multiples of random density]) of selected minerals for uncorrelated grains (blue curves), and a theoretical random distribution (red curves). ODF—Orientation density functions.

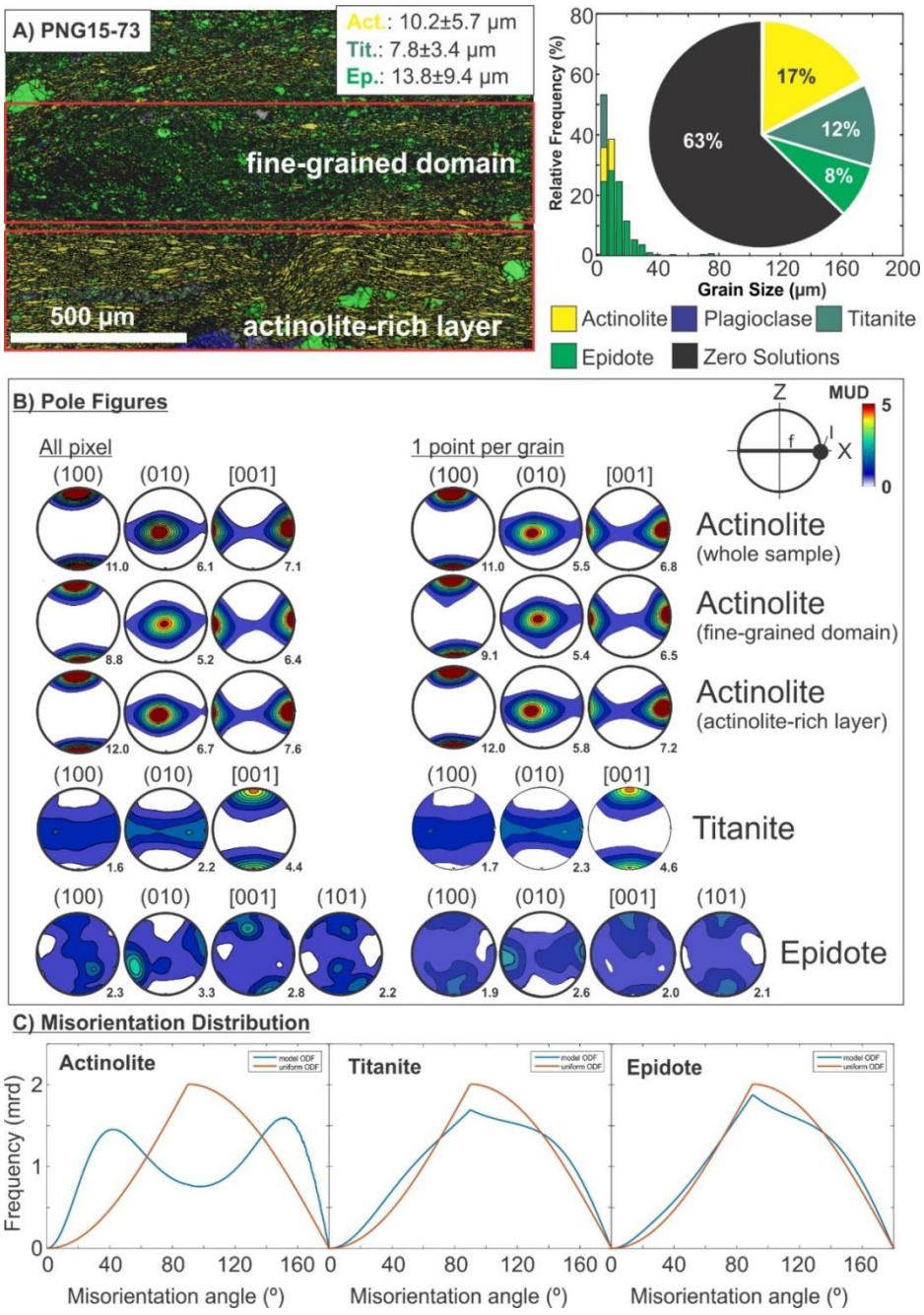

Figure S4.3. EBSD data for mylonite sample PNG15-73 (~10 m south of the active Mai'iu fault trace). A) EBSD-based phase map (1 µm step size) and average grain sizes of titanite, actinolite and epidote based on the whole map (left-hand site); grain-size histogram (relative frequency[%] vs. grain size [µm]) and phase fraction (%; pie diagram) of selected minerals based on the whole map (right-hand side). B) Contoured pole figures of selected crystallographic axes and poles; left—based on all pixels; right—based on one point per grain. MUD—Multiples of uniform distribution; l—lineation; f—foliation. C) Misorientation distribution plot (misorientation angle versus frequency [mrd=multiples of random density]) of selected minerals based on the whole map for uncorrelated grains (blue curves), and a theoretical random distribution (red curves). ODF—Orientation density functions.

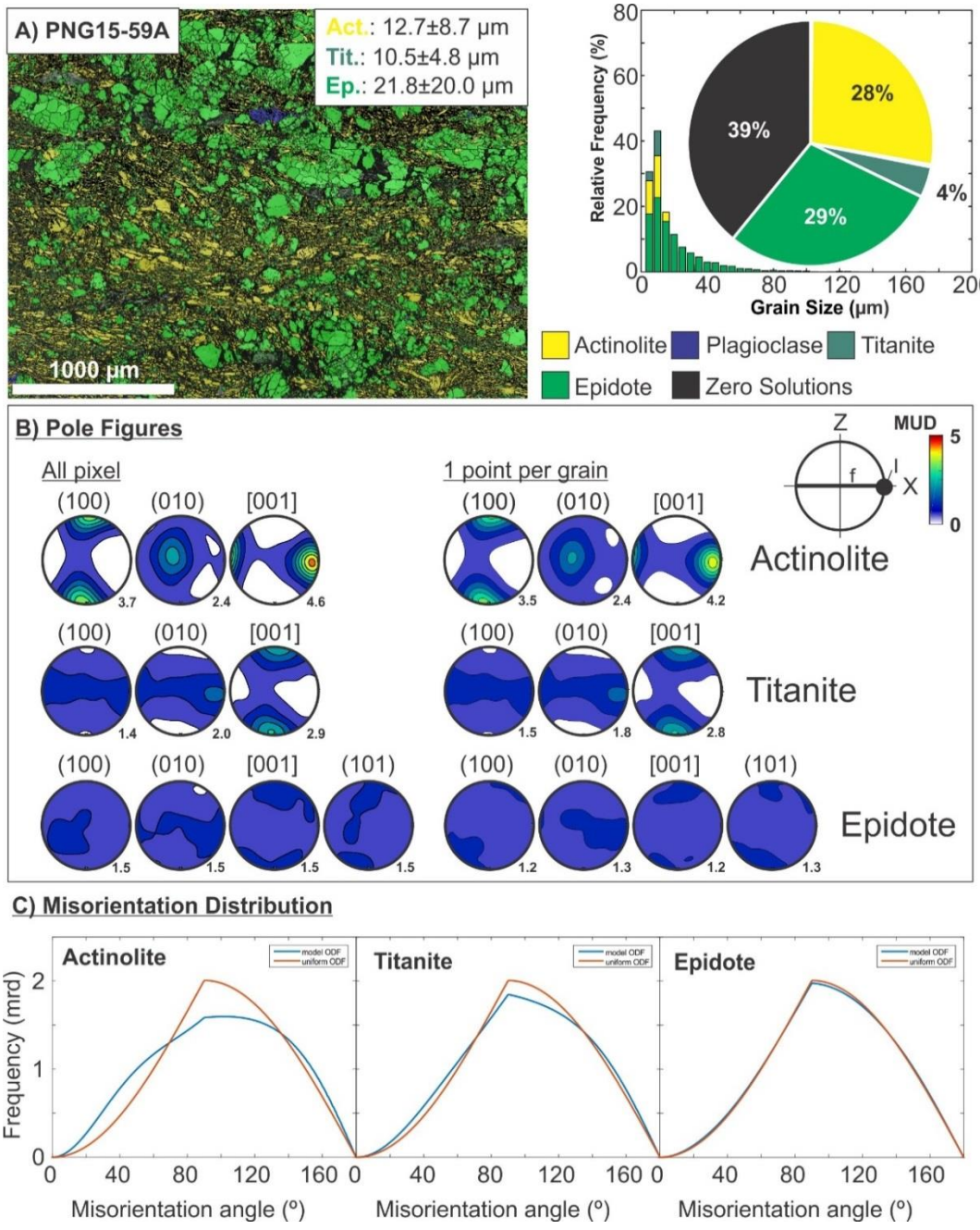

Figure S4.4. EBSD data for an epidote-rich domain of mylonite sample PNG15-59A (~50 m south of the active Mai'iu fault trace). A) EBSD-based phase map (2 µm step size) and average grain sizes of titanite, actinolite and epidote (left-hand site); grain-size histogram (relative frequency[%] vs. grain size [µm]) and phase fraction (%; pie diagram) of selected minerals (right-hand side). B) Contoured pole figures of selected crystallographic axes and poles; left—based on all pixels; right—based on one point per grain. MUD—Multiples of uniform distribution; l—lineation; f—foliation. C) Misorientation distribution plot (misorientation angle versus frequency [mrd=multiples of random density]) of selected minerals for uncorrelated grains (blue curves), and a theoretical random distribution (red curves). ODF—Orientation density functions.

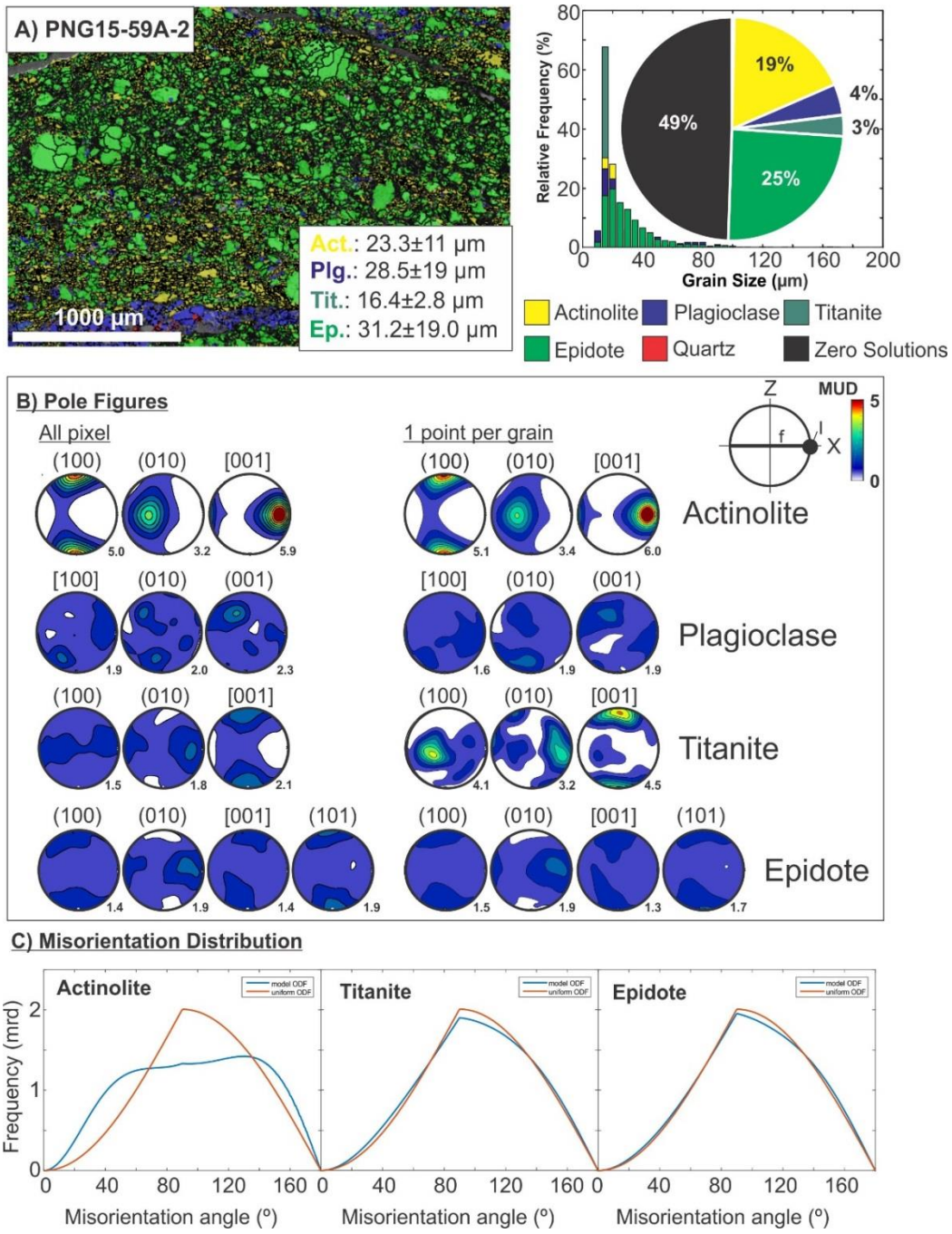

Figure S4.5. EBSD data for mylonite sample PNG15-59A-2 (~50 m south of the active Mai'iu fault trace). A) EBSD-based phase map (5 µm step size) and average grain sizes of titanite, actinolite, epidote and albite (left-hand site); grain-size histogram (relative frequency[%] vs. grain size [µm]) and phase fraction (%; pie diagram) of selected minerals (right-hand side). B) Contoured pole figures of selected crystallographic axes and poles; left—based on all pixels; right—based on one point per grain. MUD—Multiples of uniform distribution; l—lineation; f—foliation. C) Misorientation distribution plot (misorientation angle versus frequency [mrd=multiples of random density]) of selected minerals for uncorrelated grains (blue curves), and a theoretical random distribution (red curves). ODF—Orientation density functions.

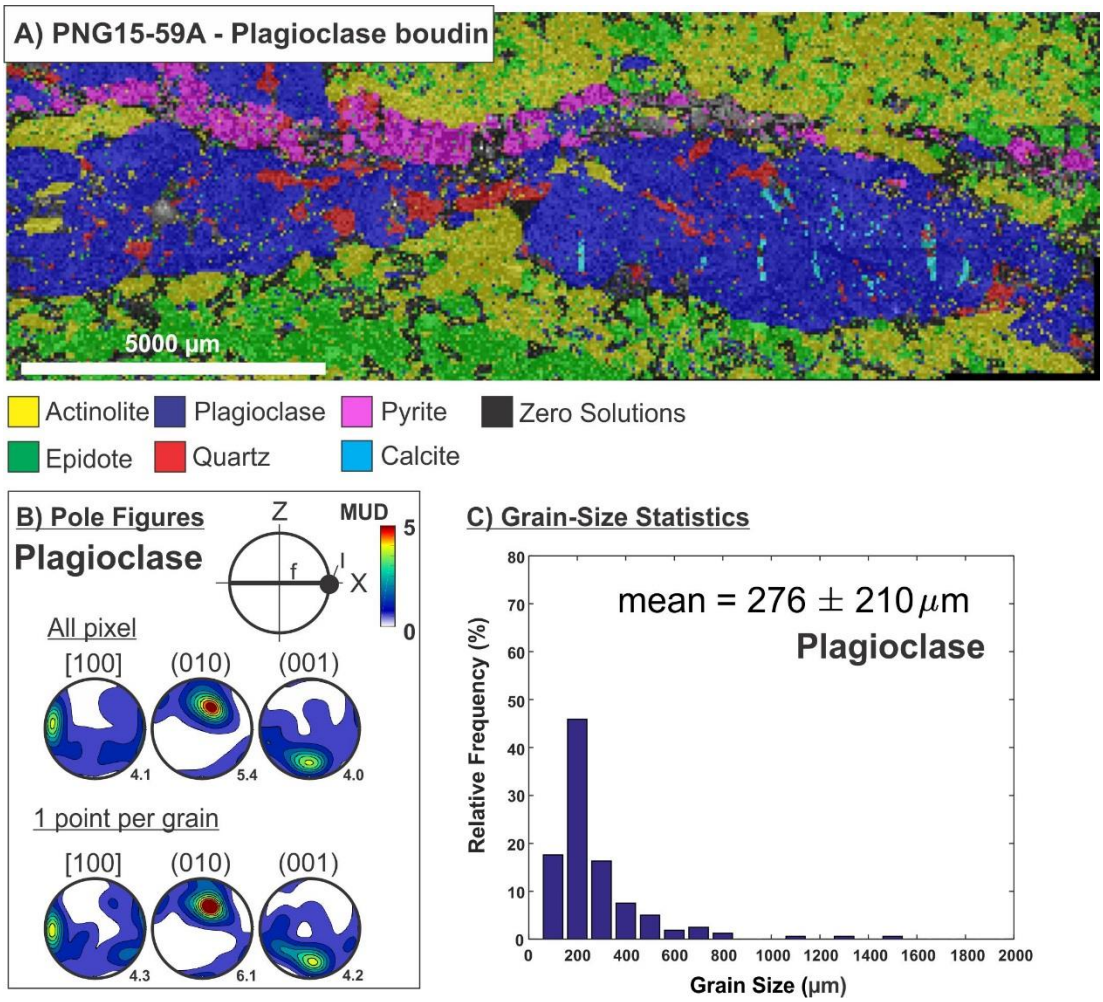

Figure S4.6. EBSD data for of albitic boudin in mylonite sample PNG15-59A (albite only; ~50 m south of the active Mai'iu fault trace). A) Phase map (50 µm step size). B) Contoured pole figures of selected crystallographic axes and poles in albite based on all pixels (top row) and based on one point per grain (bottom row). C) Albite grain size statistics.

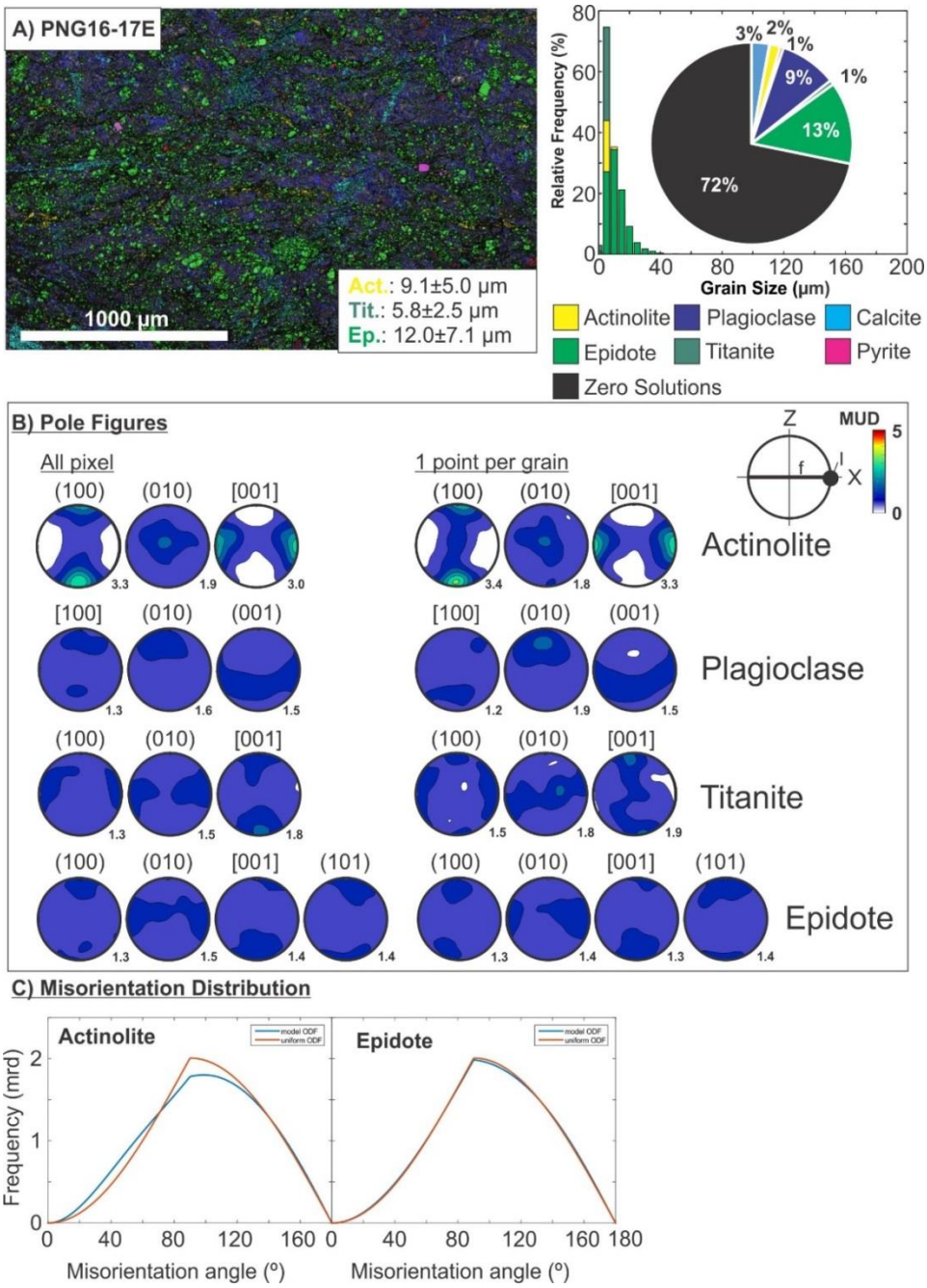

Figure S4.7. EBSD analysis of (ultra?)mylonite sample PNG16-17E (~50 cm structurally beneath the foliated cataclasite unit close to the inactive Mai'iu fault trace). A) EBSD-based phase map (1 µm step size) and average grain sizes of titanite, actinolite and epidote (left-hand site); grain-size histogram (relative frequency[%] vs. grain size [µm]) and phase fraction (%; pie diagram) of selected minerals (right-hand side). B) Contoured pole figures of selected crystallographic axes and poles; left—based on all pixels; right—based on one point per grain. MUD—Multiples of uniform distribution; l—lineation; f—foliation. C) Misorientation distribution plot (misorientation angle versus frequency [mrd=multiples of random density]) of selected minerals for uncorrelated grains (blue curves), and a theoretical random distribution (red curves). ODF—Orientation density functions.

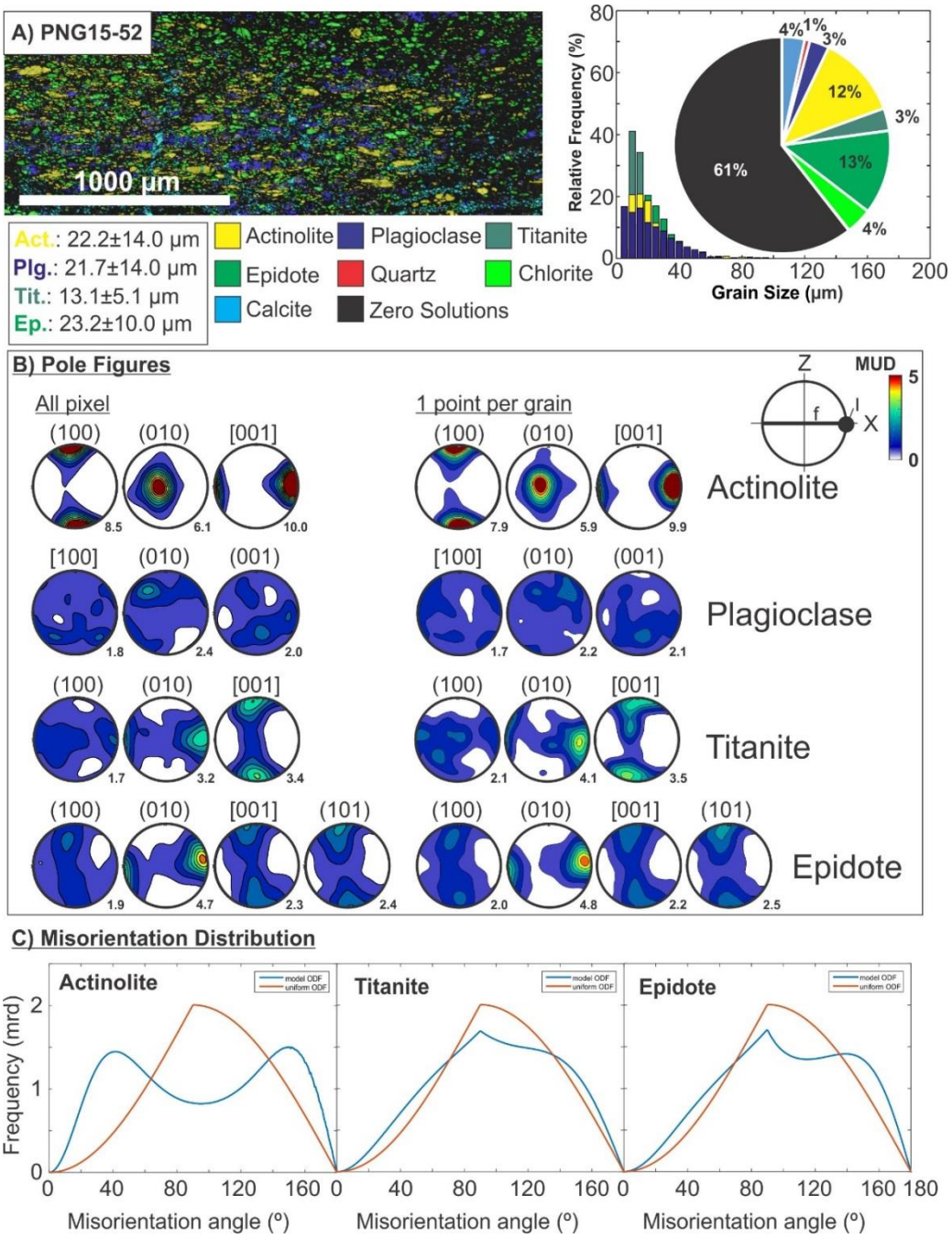

Figure S4.8. EBSD data for mylonite sample PNG15-52 (~5 m south of the active Mai'iu fault trace). A) EBSD-based phase map (2 µm step size) and average grain sizes of titanite, actinolite, epidote and albite (left-hand site); grain-size histogram (relative frequency[%] vs. grain size [µm]) and phase fraction (%; pie diagram) of selected minerals (right-hand side). B) Contoured pole figures of selected crystallographic axes and poles; left—based on all pixels; right—based on one point per grain. MUD—Multiples of uniform distribution; l—lineation; f—foliation. C) Misorientation distribution plot (misorientation angle versus frequency [mrd=multiples of random density]) of selected minerals for uncorrelated grains (blue curves), and a theoretical random distribution (red curves). ODF—Orientation density functions.

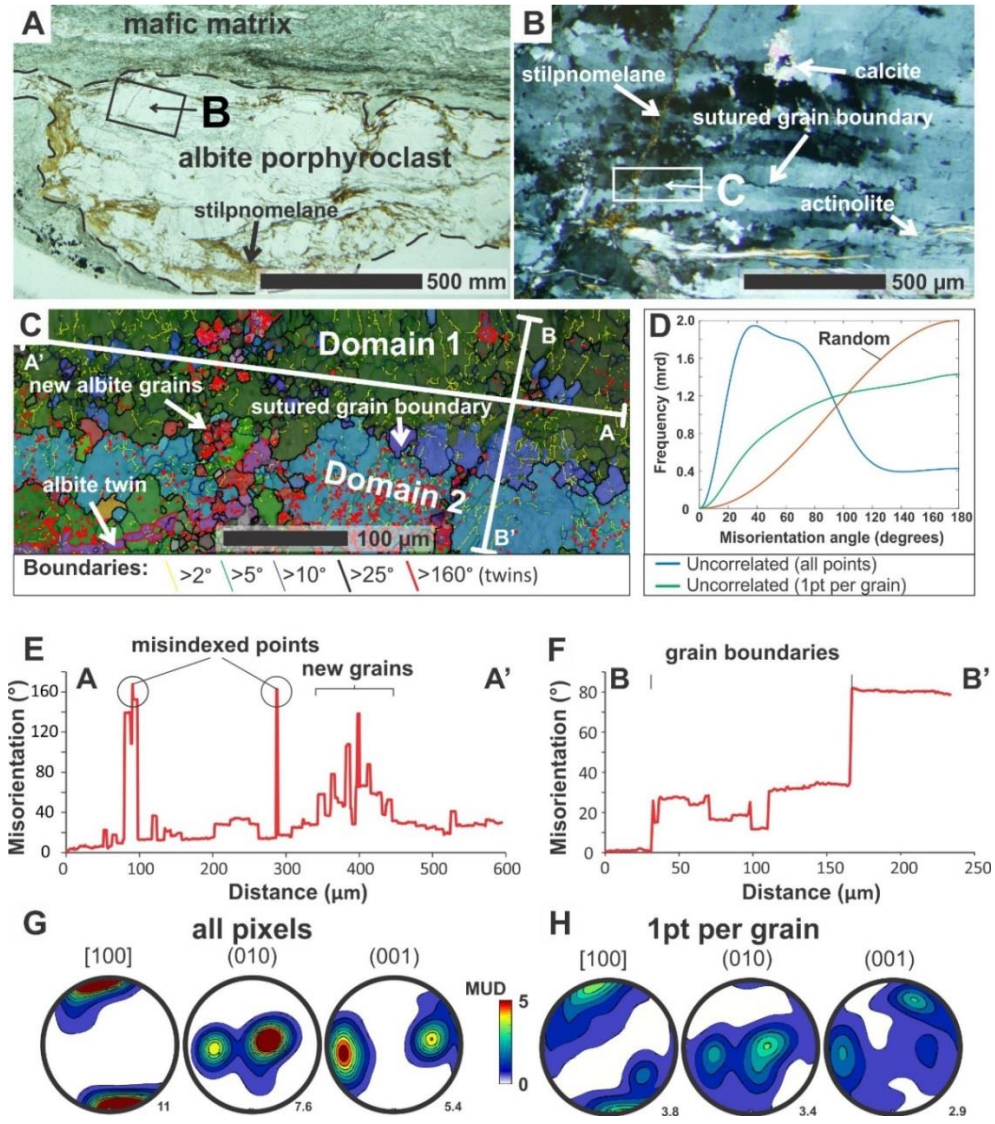

Figure S4.9. Microstructural analysis of an albite porphyroclast in the mafic mylonite sample PNG15-73. A) Optical photomicrograph of an albite porphyroclast (up to 2 cm in diameter). Stilpnomelane grew at the outer rim and along fractures of this porphyroclast. B) Optical photomicrograph (XPOL) of the deformed albite porphyroclast showing strong internal lattice distortion, intergrown actinolite fibres, and stilpnomelane ±calcite in fractures. C) EBSD (all Euler colors) map of the host albite grain (Domain 1), albite grain with bulged and sutured grain boundaries (Domain 2), and smaller albite aggregates (step size: 1 µm). D) Misorientation distribution plot (misorientation angle versus frequency [mrd=multiples of random density]) for all collected points and one point per grain (uncorrelated), and a theoretical random distribution. Note, misindexed points were excluded from this analysis. E) and F) misorientation profiles (misorientation angle relative to the starting point) across the different albite domains. G) and H) Lower-hemisphere, equal-area pole plots of selected crystallographic directions (Schmidt projection) of all collected points (pixels; mostly controlled by the orientation of the parent albite grain); and one point per grain (embraces the orientations of recrystallized grains in the analyzed section).

Foliated Cataclasites:

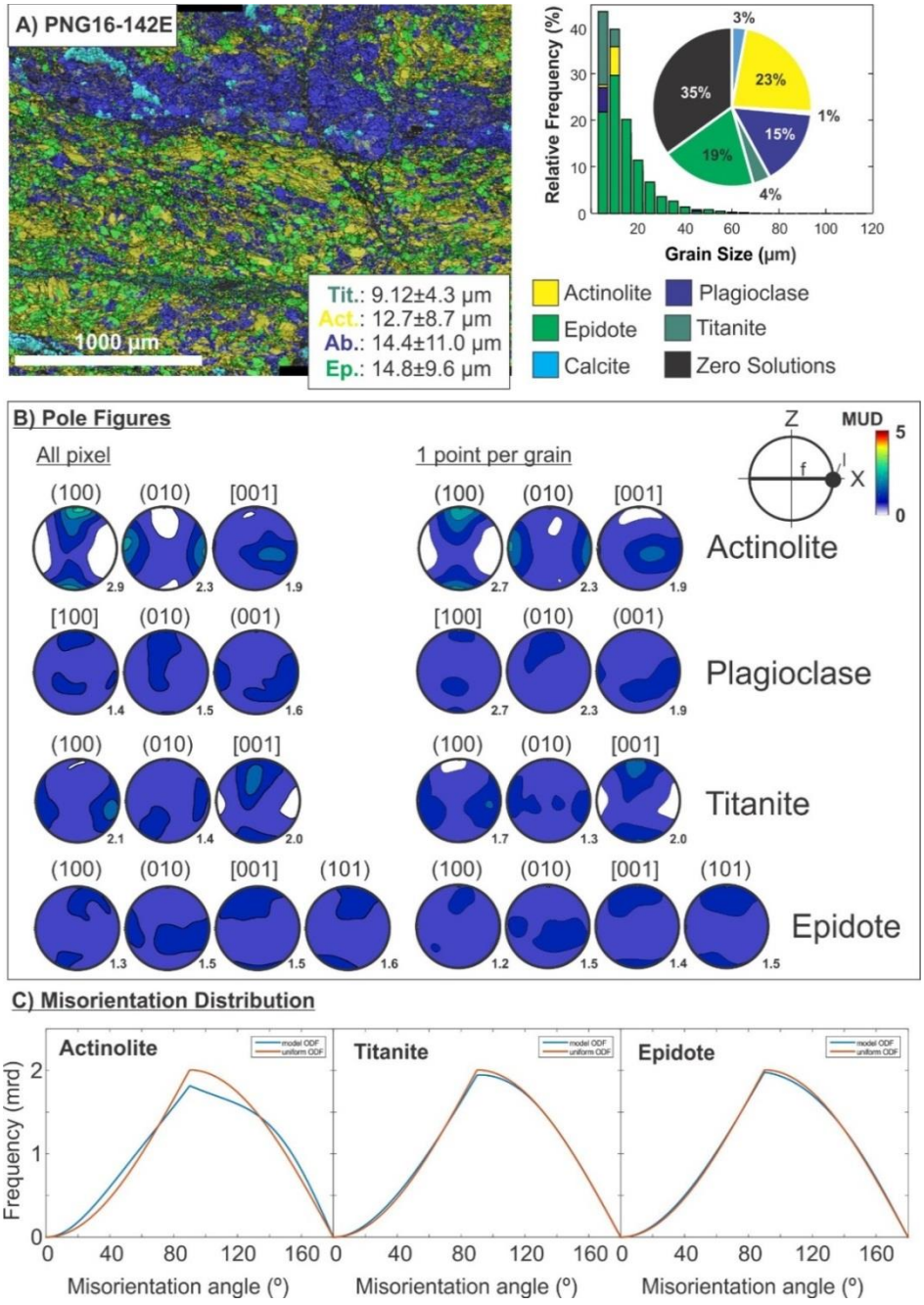

Figure S4.10. EBSD data for foliated cataclasite sample PNG16-142E (at active Mai'iu fault trace). A) EBSD-based phase map (2 µm step size) and average grain sizes of titanite, actinolite, epidote and albite (left-hand site); grain-size histogram (relative frequency[%] vs. grain size [µm]) and phase fraction (%; pie diagram) of selected minerals (right-hand side). B) Contoured pole figures of selected crystallographic axes and poles; left—based on all pixels; right—based on one point per grain. MUD—Multiples of uniform distribution; l—lineation; f—foliation. C) Misorientation distribution plot (misorientation angle versus frequency [mrd=multiples of random density]) of selected minerals for uncorrelated grains (blue curves), and a theoretical random distribution (red curves). ODF—Orientation density functions.

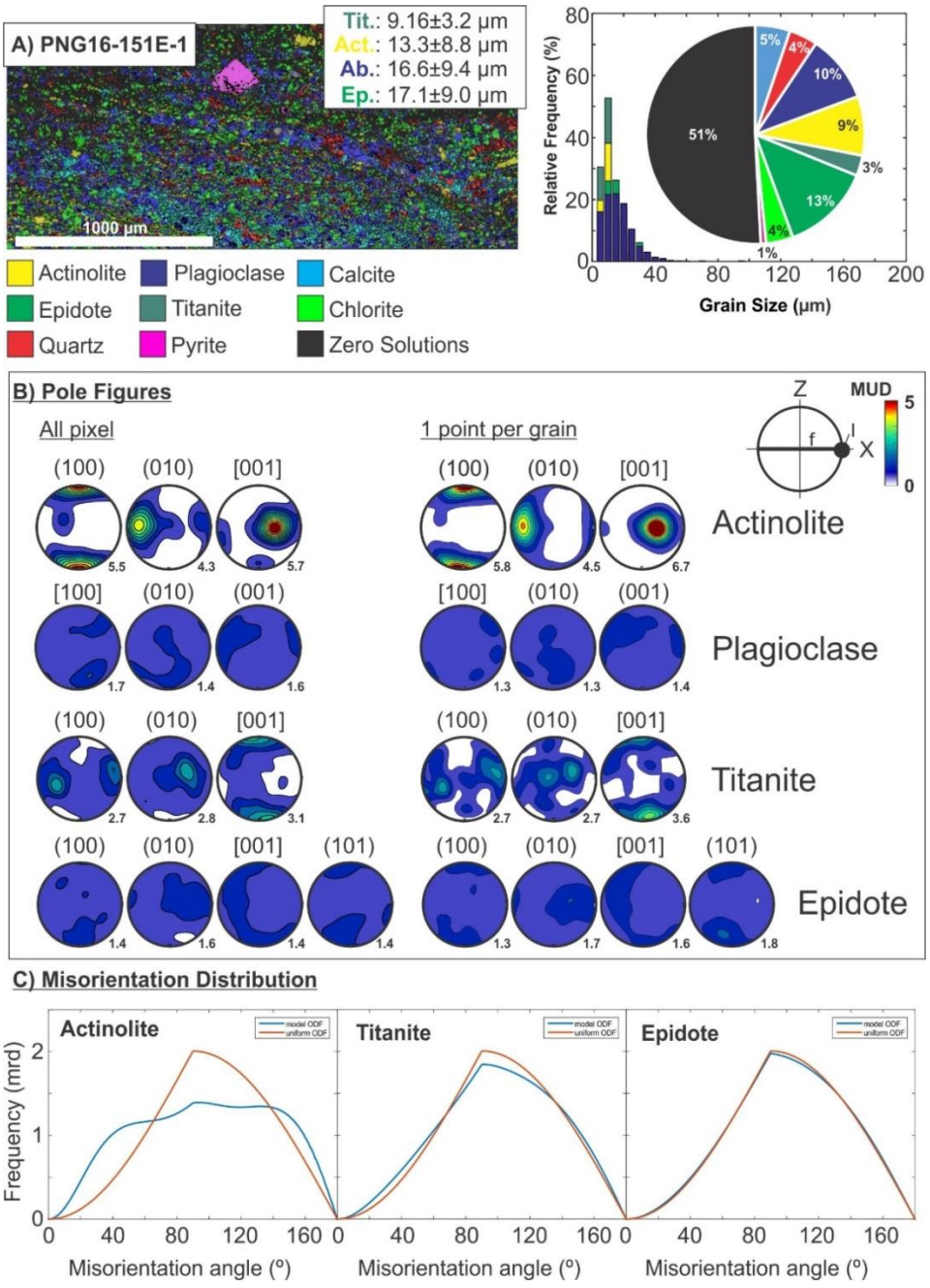

Figure S4.11. EBSD data for of foliated cataclasite sample PNG16-151E-1 (~2 m south of active Mai'iu fault trace). A) EBSD-based phase map (2 µm step size) and average grain sizes of titanite, actinolite, epidote and albite (left-hand site); grain-size histogram (relative frequency[%] vs. grain size [µm]) and phase fraction (%; pie diagram) of selected minerals (right-hand side). B) Contoured pole figures of selected crystallographic axes and poles; left—based on all pixels; right—based on one point per grain. MUD—Multiples of uniform distribution; l—lineation; f—foliation. C) Misorientation distribution plot (misorientation angle versus frequency [mrd=multiples of random density]) of selected minerals for uncorrelated grains (blue curves), and a theoretical random distribution (red curves). ODF—Orientation density functions.

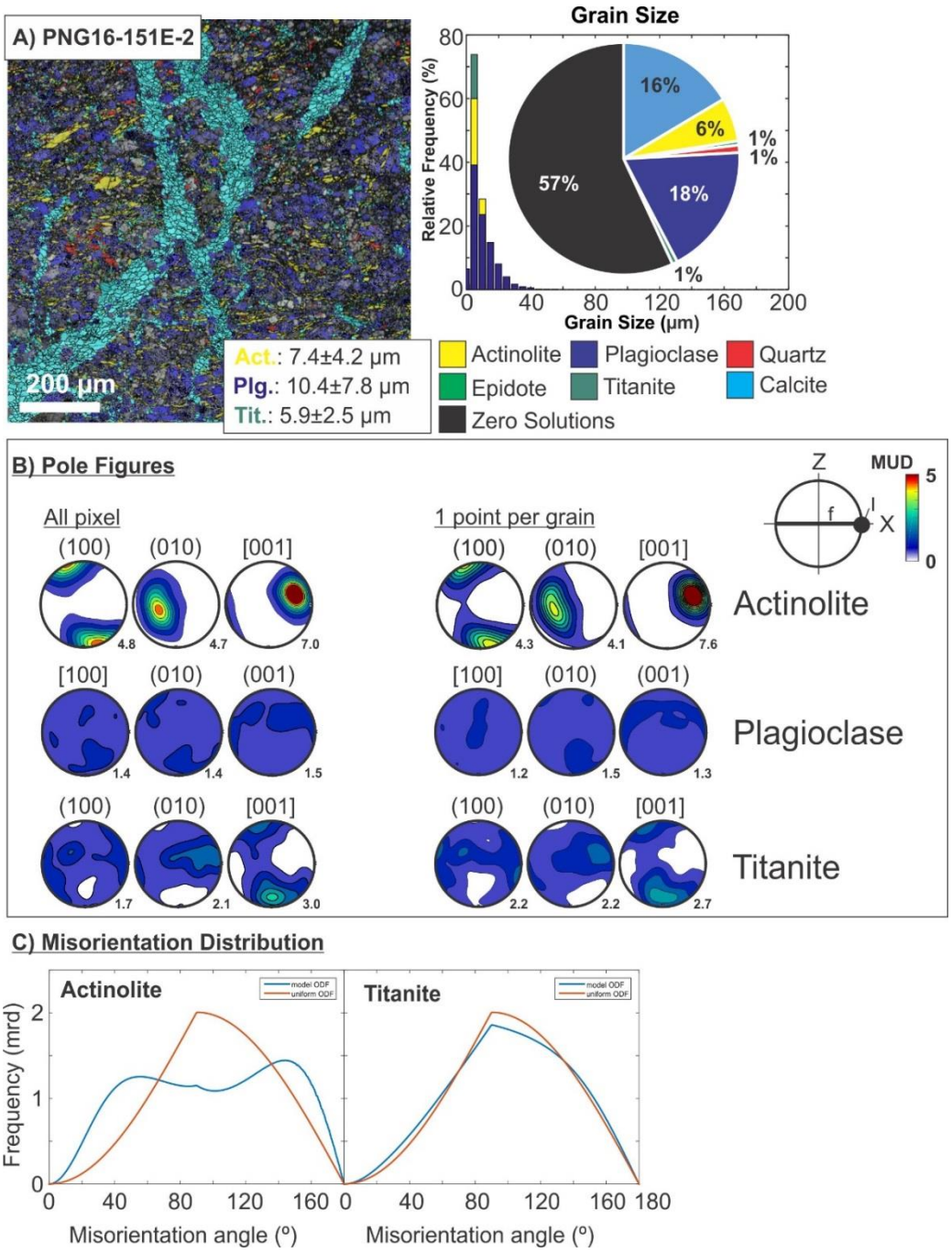

Figure S4.12. EBSD data for of foliated cataclasite sample PNG16-151E-2 (~2 m south of active Mai'iu fault trace). A) EBSD-based phase map (1 µm step size) and average grain sizes of titanite, actinolite and albite (left-hand site); grain-size histogram (relative frequency[%] vs. grain size [µm]) and phase fraction (%; pie diagram) of selected minerals (right-hand side). B) Contoured pole figures of selected crystallographic axes and poles; left—based on all pixels; right—based on one point per grain. MUD—Multiples of uniform distribution; l—lineation; f—foliation. C) Misorientation distribution plot (misorientation angle versus frequency [mrd=multiples of random density]) of selected minerals for uncorrelated grains (blue curves), and a theoretical random distribution (red curves). ODF—Orientation density functions.

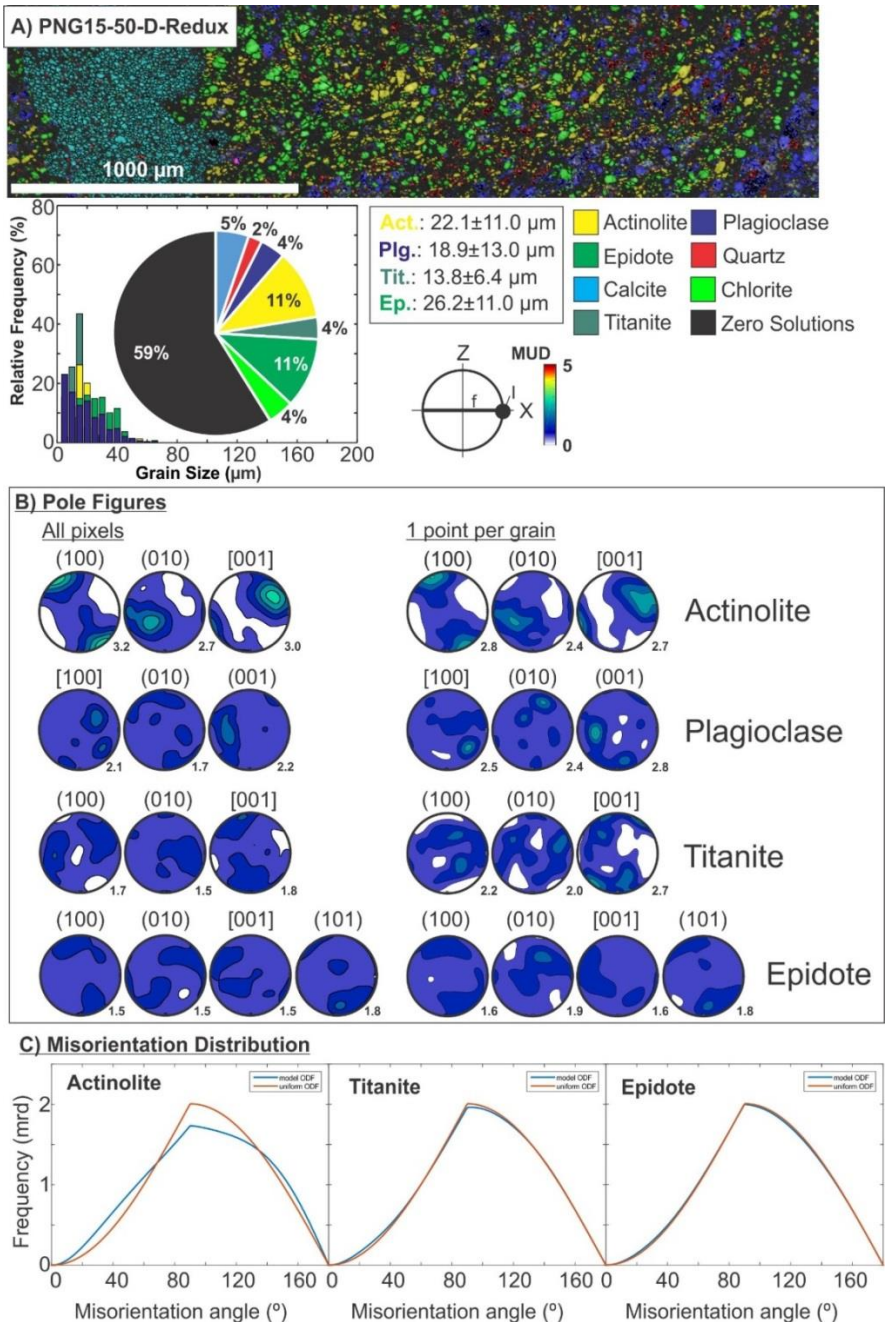

Figure S4.13. EBSD data for of foliated cataclasite sample PNG15-50D-Redux (~20 cm below ultracataclasite layer at active Mai'iu fault trace). A) EBSD-based phase map (2 µm step size; top); average grain sizes of titanite, actinolite, epidote and albite, grain-size histogram (relative frequency[%] vs. grain size [µm]) and phase fraction (%; pie diagram) of selected minerals (below phase map). B) Contoured pole figures of selected crystallographic axes and poles; left—based on all pixels; right—based on one point per grain. MUD—Multiples of uniform distribution; l—lineation; f—foliation. C) Misorientation distribution plot (misorientation angle versus frequency [mrd=multiples of random density]) of selected minerals for uncorrelated grains (blue curves), and a theoretical random distribution (red curves). ODF—Orientation density functions.

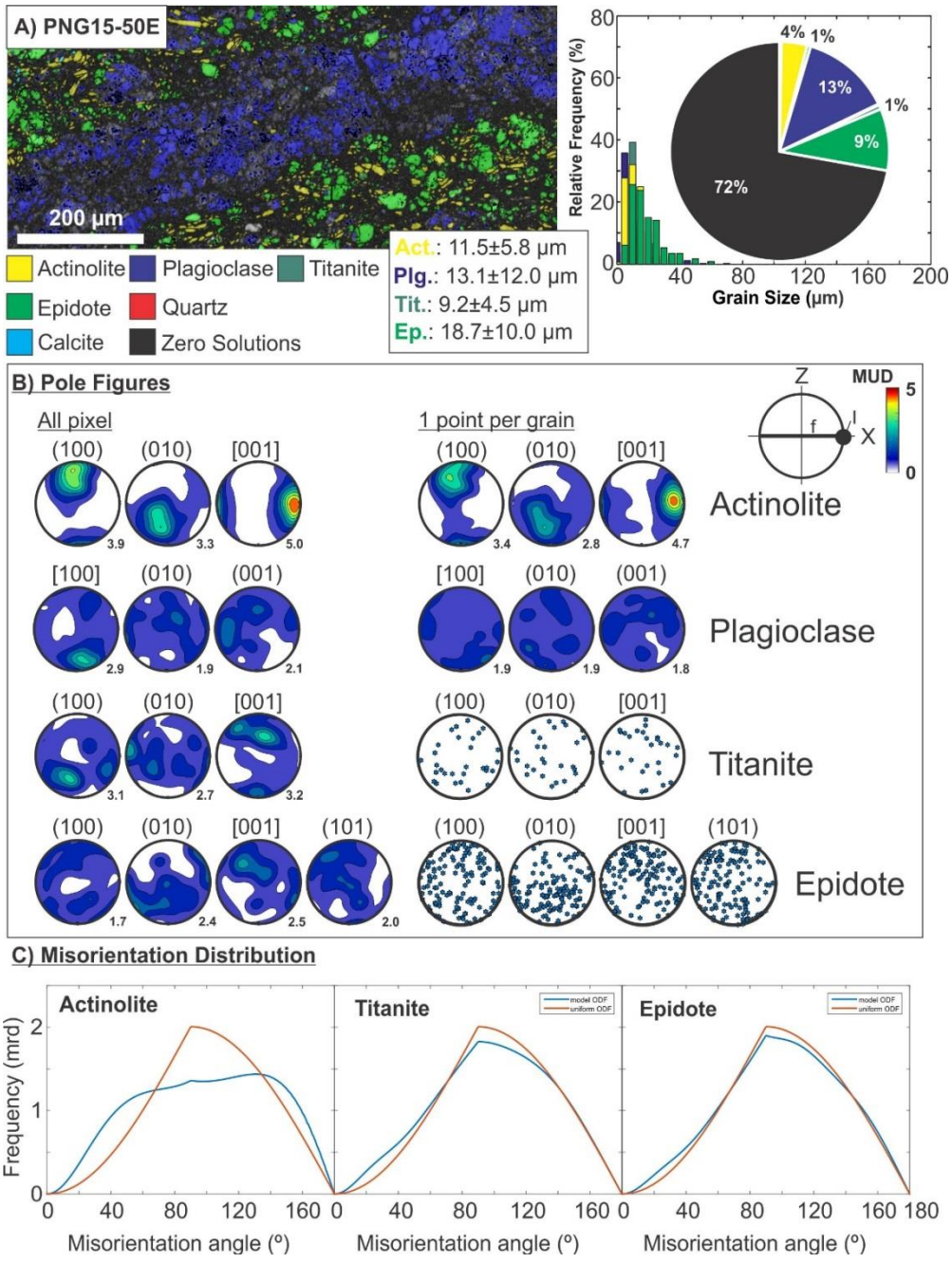

Figure S4.14. EBSD data for foliated cataclasite sample PNG15-50E (~20 cm below ultracataclasite layer at active Mai'iu fault trace). A) EBSD-based phase map (1 µm step size) and average grain sizes of titanite, actinolite, epidote and albite (left-hand site); grain-size histogram (relative frequency[%] vs. grain size [µm]) and phase fraction (%; pie diagram) of selected minerals (right-hand side). B) Contoured pole figures of selected crystallographic axes and poles; left—based on all pixels; right—based on one point per grain. MUD—Multiples of uniform distribution; l—lineation; f—foliation. C) Misorientation distribution plot (misorientation angle versus frequency [mrd=multiples of random density]) of selected minerals for uncorrelated grains (blue curves), and a theoretical random distribution (red curves). ODF—Orientation density functions.

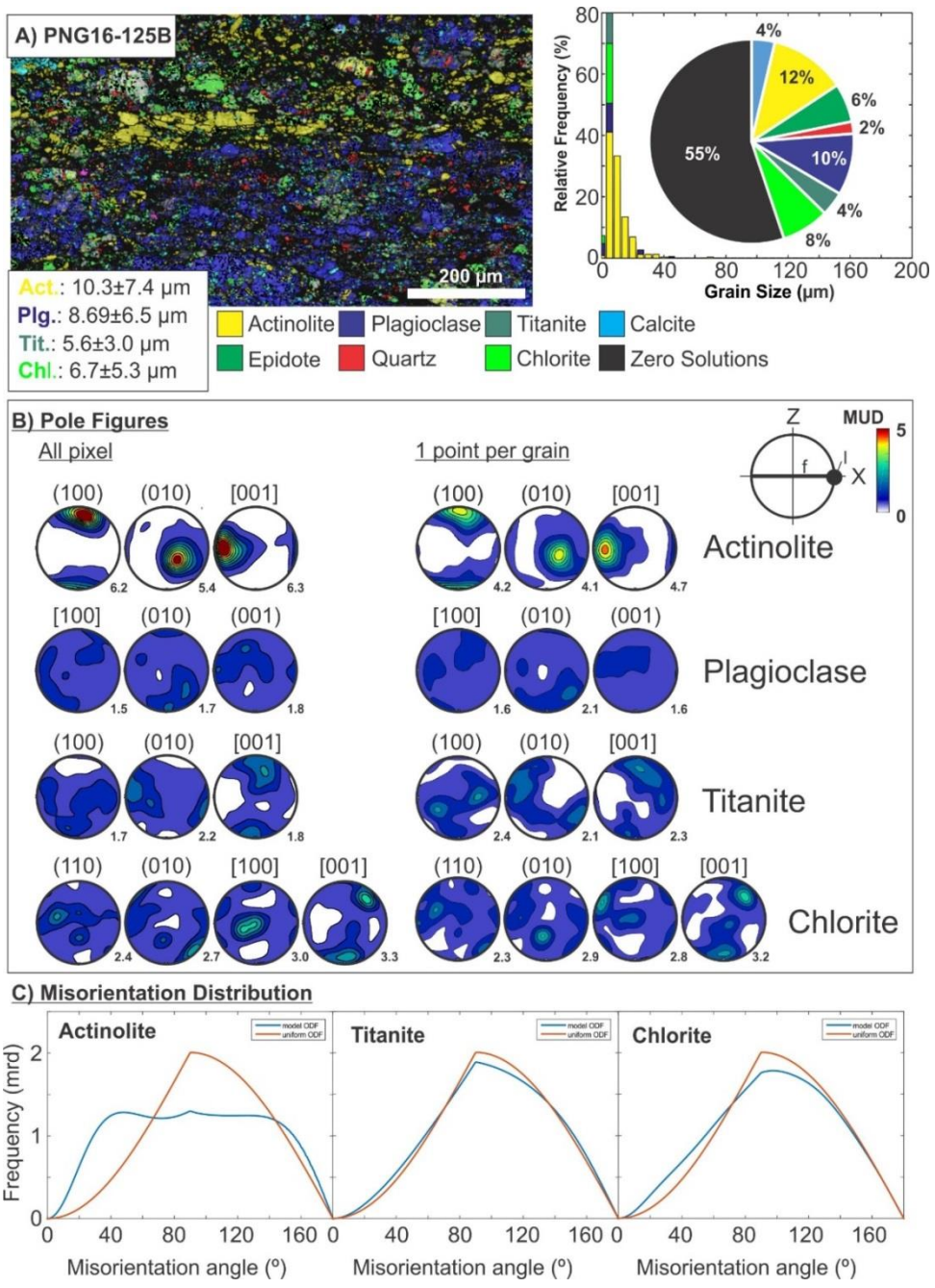

Figure S4.15. EBSD data for of cataclasite sample PNG16-125B (just south of active(?) Mai'iu fault trace, close to Gwoira fault). A) EBSD-based phase map (1 µm step size) and average grain sizes of titanite, actinolite, epidote and albite (left-hand site); grain-size histogram (relative frequency[%] vs. grain size [µm]) and phase fraction (%; pie diagram) of selected minerals (right-hand side). B) Contoured pole figures of selected crystallographic axes and poles; left—based on all pixels; right—based on one point per grain. MUD—Multiples of uniform distribution; l—lineation; f—foliation. C) Misorientation distribution plot (misorientation angle versus frequency [mrd=multiples of random density]) of selected minerals for uncorrelated grains (blue curves), and a theoretical random distribution (red curves). ODF—Orientation density functions.

Ultracataclasites:

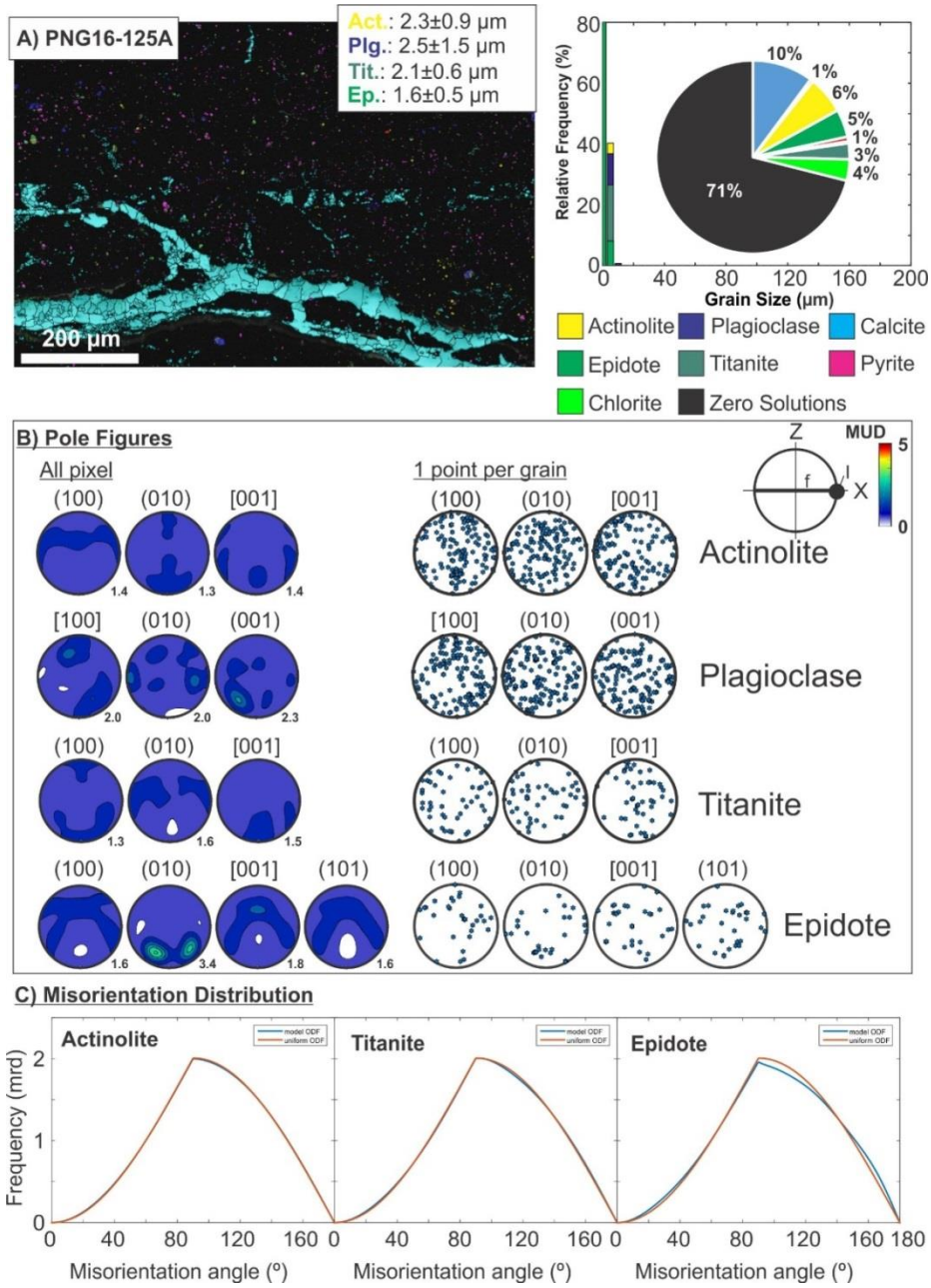

Figure S4.16. EBSD data for ultracataclasite sample PNG16-125A. A) EBSD-based phase map (0.5 µm step size) and average grain sizes of titanite, actinolite, epidote and albite (left-hand site); grain-size histogram (relative frequency[%] vs. grain size [µm]) and phase fraction (%; pie diagram) of selected minerals (right-hand side). B) Contoured pole figures of selected crystallographic axes and poles; left—based on all pixels; right—based on one point per grain. MUD—Multiples of uniform distribution; l—lineation; f—foliation. C) Misorientation distribution plot (misorientation angle versus frequency [mrd=multiples of random density]) of selected minerals for uncorrelated grains (blue curves), and a theoretical random distribution (red curves). ODF—Orientation density functions.

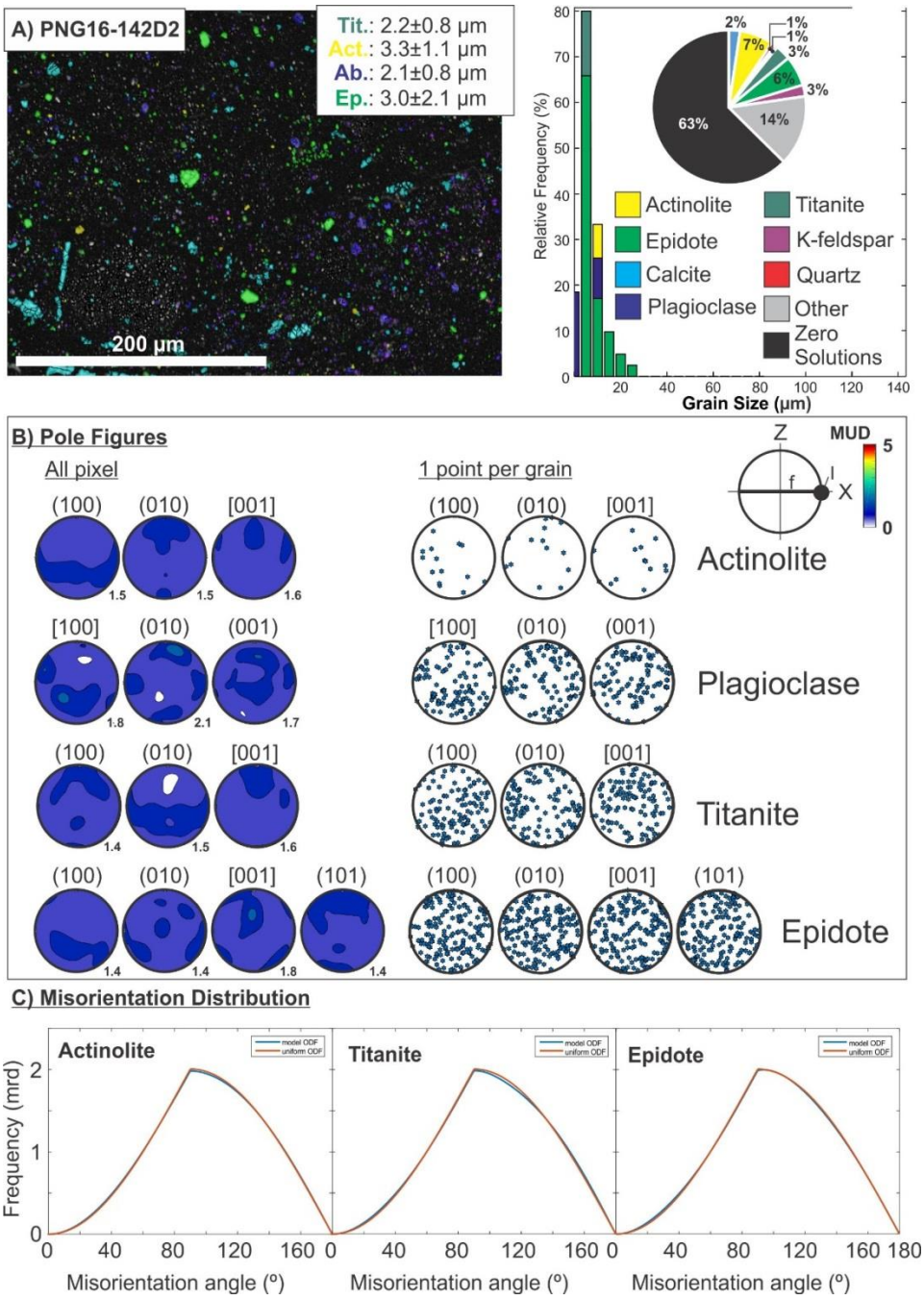

Figure S4.17. EBSD data for ultracataclasite sample PNG16-142D2. A) EBSD-based phase map (0.6 µm step size) and average grain sizes of titanite, actinolite, epidote and albite (left-hand site); grain-size histogram (relative frequency[%] vs. grain size [µm]) and phase fraction (%; pie diagram) of selected minerals (right-hand side). B) Contoured pole figures of selected crystallographic axes and poles; left—based on all pixels; right—based on one point per grain. MUD—Multiples of uniform distribution; l—lineation; f—foliation. C) Misorientation distribution plot (misorientation angle versus frequency [mrd=multiples of random density]) of selected minerals for uncorrelated grains (blue curves), and a theoretical random distribution (red curves). ODF—Orientation density functions.

Mafic Gouges:

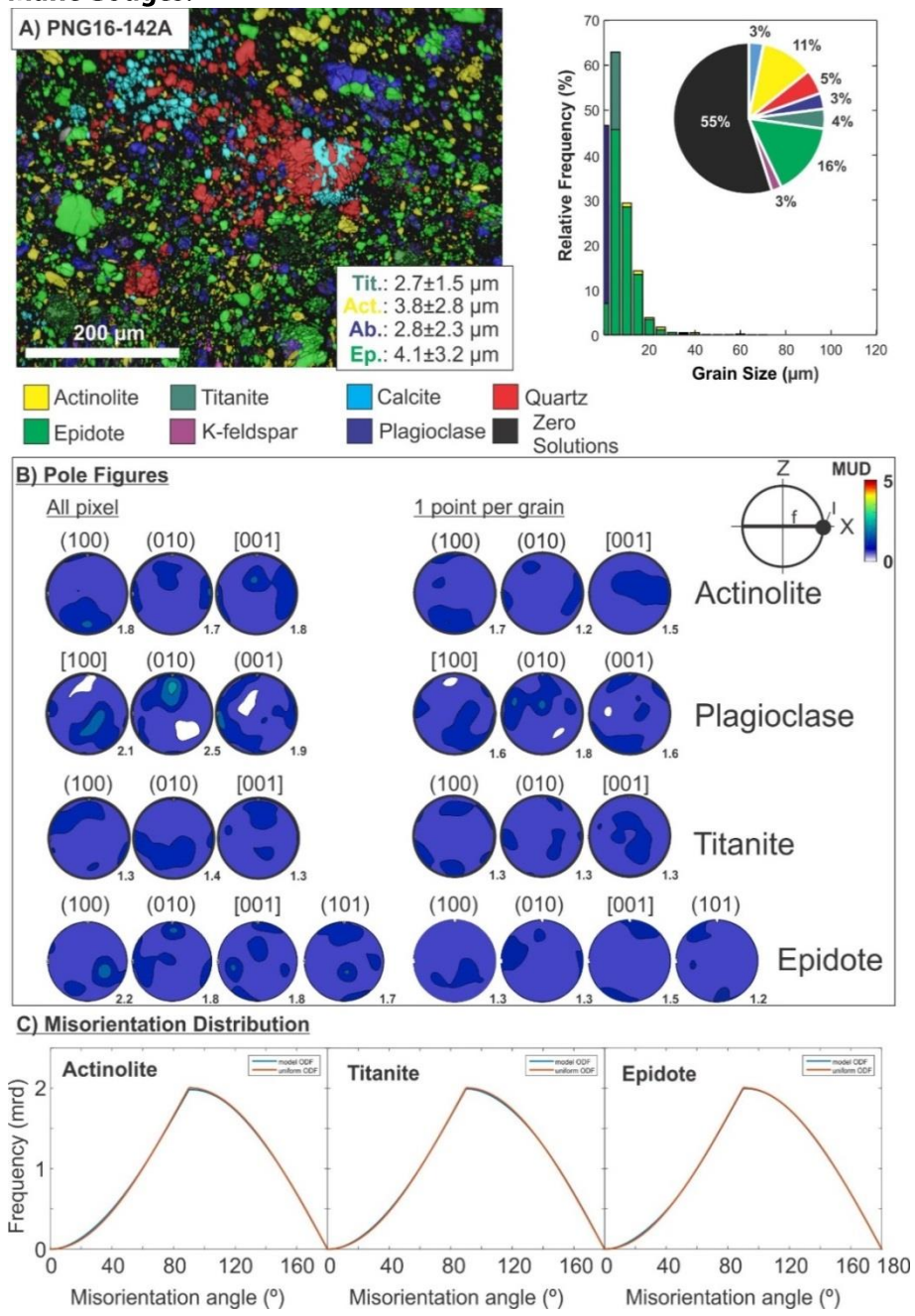

Figure S4.18. EBSD data for gouge sample PNG16-142A (active Mai'iu fault trace). A) EBSD-based phase map (0.5 µm step size) and average grain sizes of titanite, actinolite, epidote and albite (left-hand site); grain-size histogram (relative frequency[%] vs. grain size [µm]) and phase fraction (%; pie diagram) of selected minerals (right-hand side). B) Contoured pole figures of selected crystallographic axes and poles; left—based on all pixels; right—based on one point per grain. MUD—Multiples of uniform distribution; l—lineation; f—foliation. C) Misorientation distribution plot (misorientation angle versus frequency [mrd=multiples of random density]) of selected minerals for uncorrelated grains (blue curves), and a theoretical random distribution (red curves). ODF—Orientation density functions.

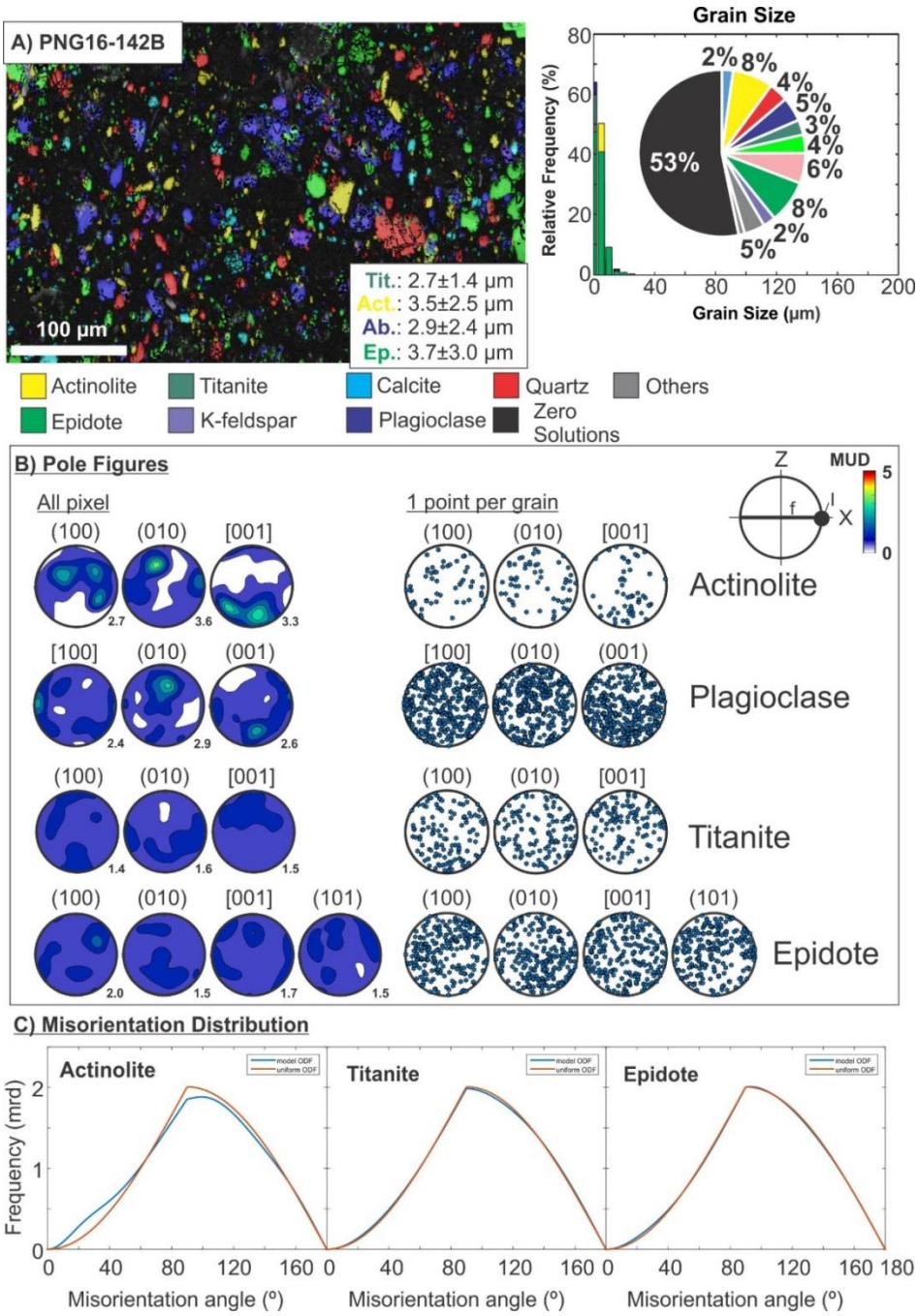

Figure S4.19. EBSD data for of gouge sample PNG16-142B (active Mai'iu fault trace). A) EBSD-based phase map (0.6 µm step size) and average grain sizes of titanite, actinolite, epidote and albite (left-hand site); grain-size histogram (relative frequency[%] vs. grain size [µm]) and phase fraction (%; pie diagram) of selected minerals (right-hand side). B) Contoured pole figures of selected crystallographic axes and poles; left—based on all pixels; right—based on one point per grain. MUD—Multiples of uniform distribution; l—lineation; f—foliation. C) Misorientation distribution plot (misorientation angle versus frequency [mrd=multiples of random density]) of selected minerals for uncorrelated grains (blue curves), and a theoretical random distribution (red curves). ODF—Orientation density functions.

Non-mylonitic mafic schist:

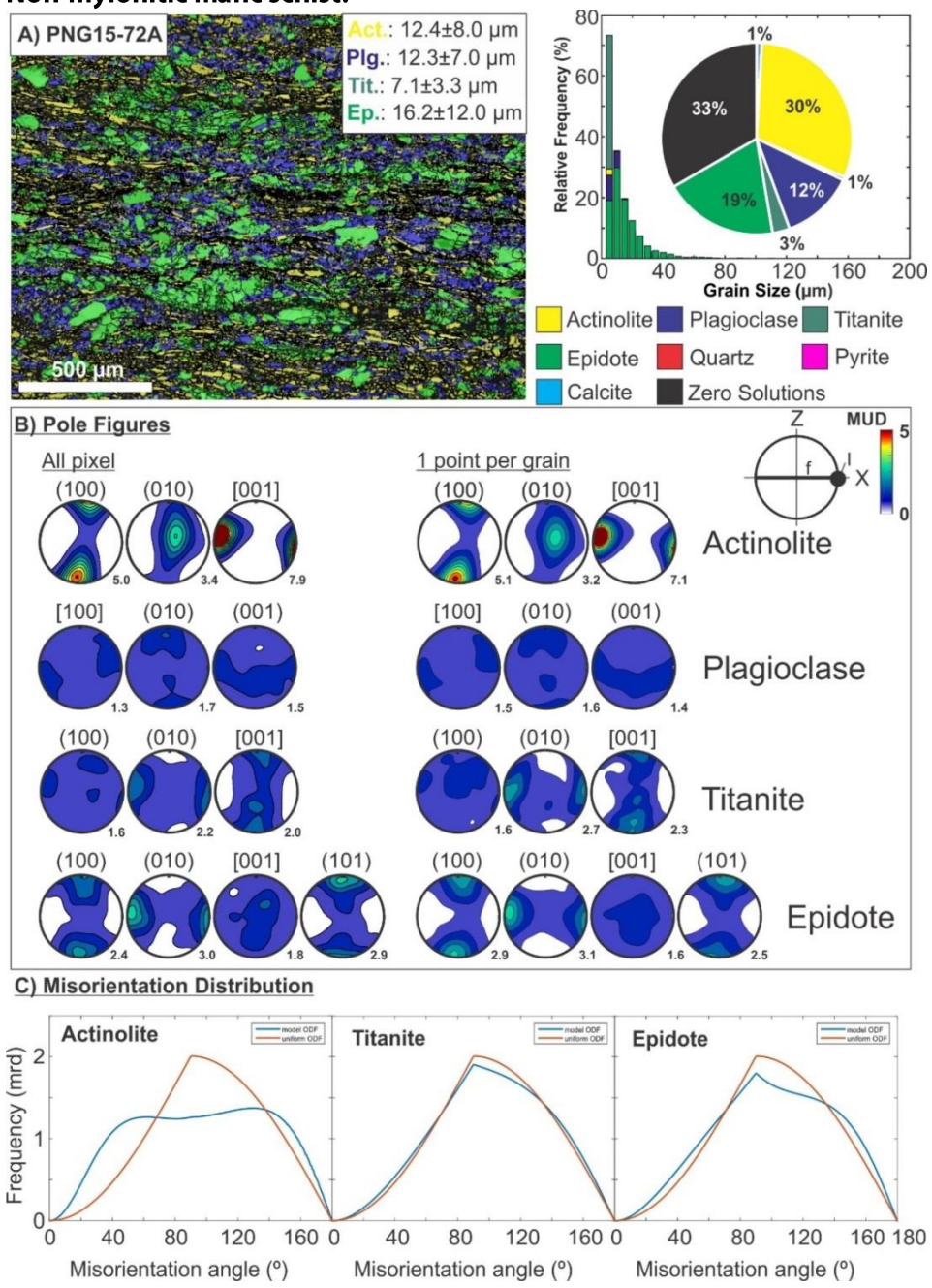

Figure S4.20. EBSD data for a non-mylonitic schist (PNG15-72A). A) EBSD-based phase map (2 µm step size) and average grain sizes of titanite, actinolite, epidote and albite (left-hand site); grain-size histogram (relative frequency[%] vs. grain size [µm]) and phase fraction (%; pie diagram) of selected minerals (right-hand side). B) Contoured pole figures of selected crystallographic axes and poles; left—based on all pixels; right—based on one point per grain. MUD—Multiples of uniform distribution; l—lineation; f—foliation. C) Misorientation distribution plot (misorientation angle versus frequency [mrd=multiples of random density]) of selected minerals for uncorrelated grains (blue curves), and a theoretical random distribution (red curves). ODF—Orientation density functions.

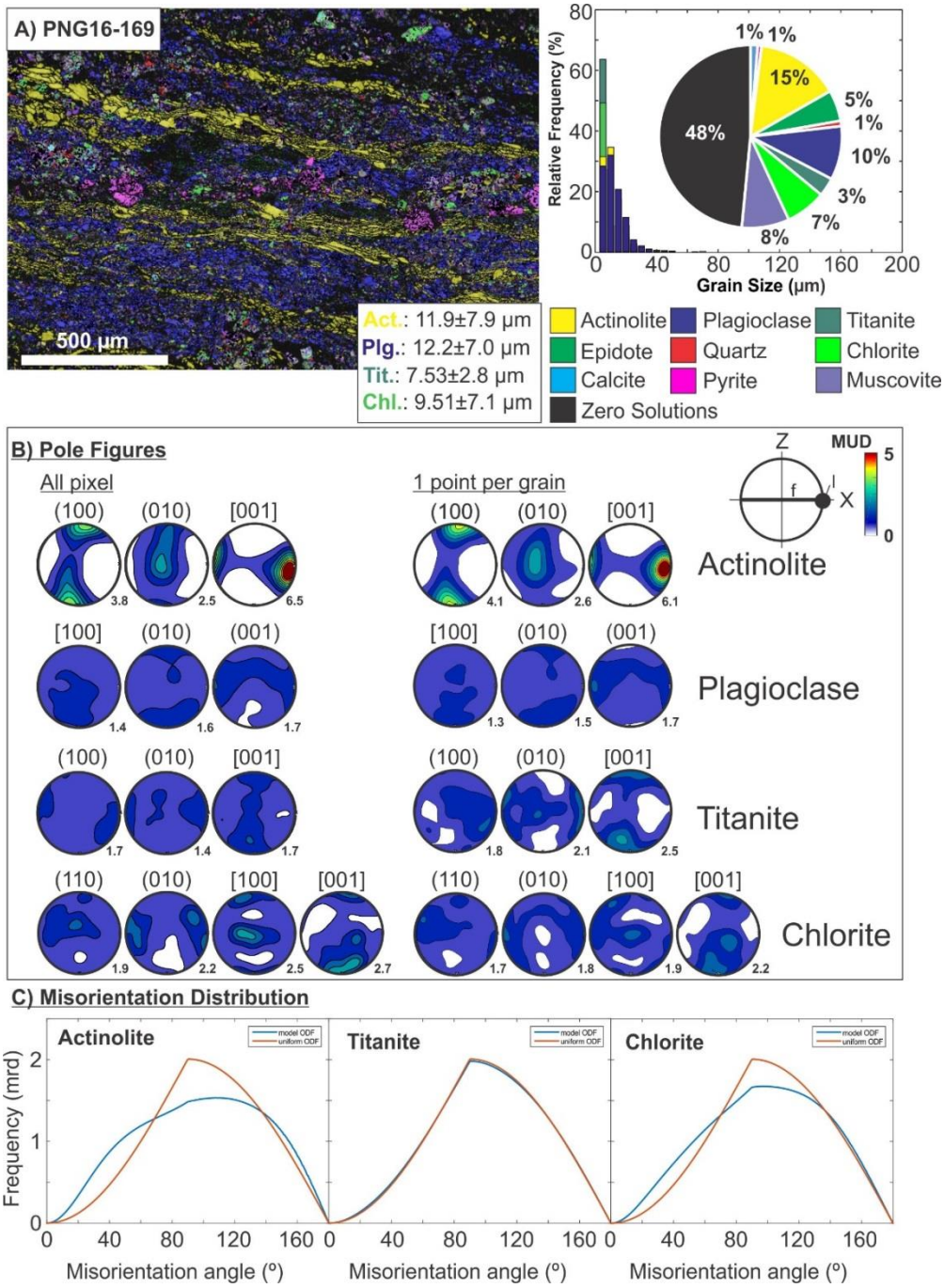

Figure S4.21. EBSD data for a non-mylonitic schist (~5.7 km south of the active Mai'iu fault trace; PNG16-169). A) EBSD-based phase map (1.5 µm step size) and average grain sizes of titanite, actinolite and albite (left-hand site); grain-size histogram (relative frequency[%] vs. grain size [µm]) and phase fraction (%; pie diagram) of selected minerals (right-hand side). B) Contoured pole figures of selected crystallographic axes and poles; left—based on all pixels; right—based on one point per grain. MUD—Multiples of uniform distribution; l—lineation; f—foliation. C) Misorientation distribution plot (misorientation angle versus frequency [mrd=multiples of random density]) of selected minerals for uncorrelated grains (blue curves), and a theoretical random distribution (red curves). ODF—Orientation density functions.

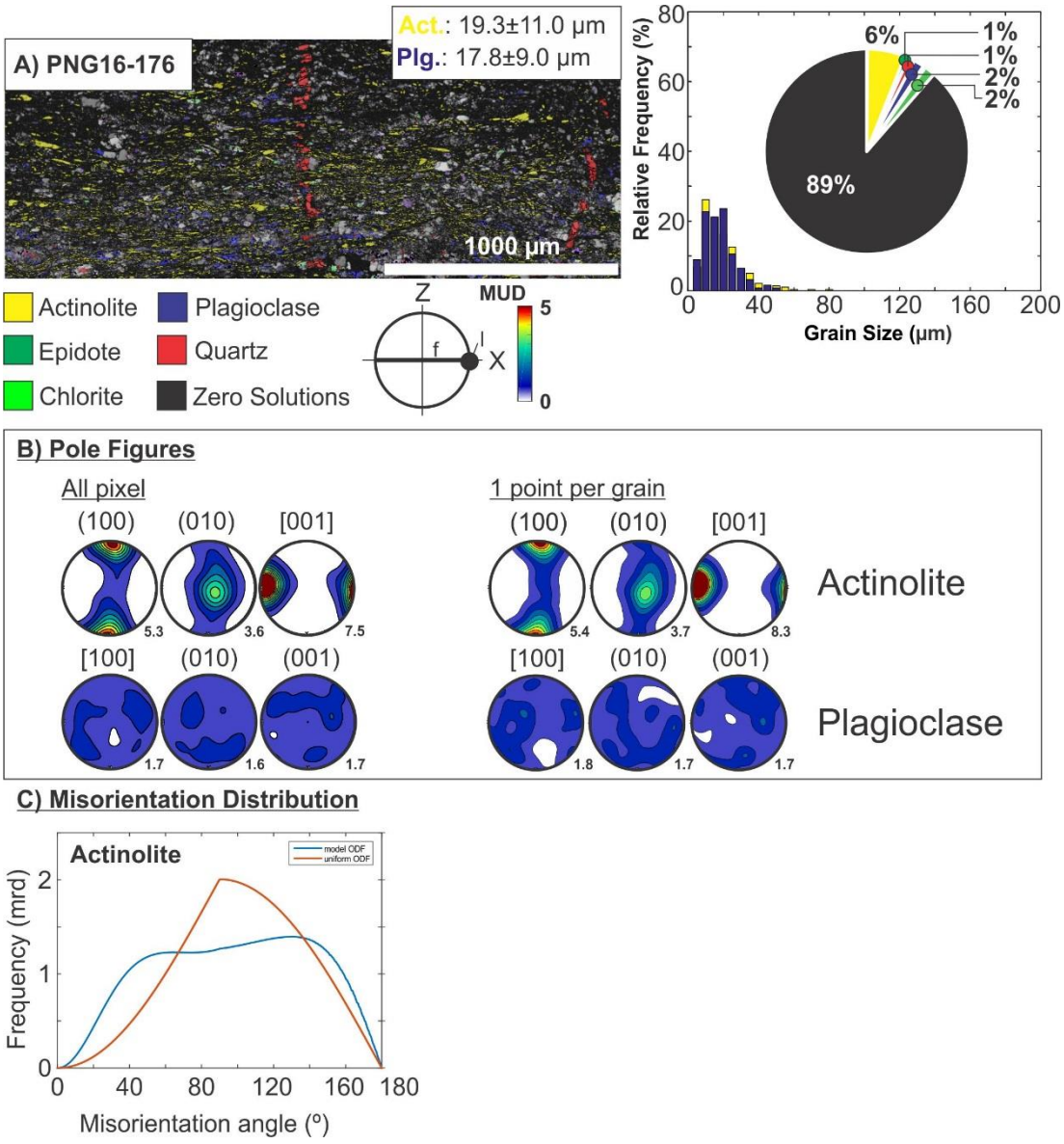

Figure S4.22. EBSD data for a non-mylonitic schist (~4.5 km south of the active Mai'iu fault trace; PNG16-176). A) EBSD-based phase map (2 µm step size) and average grain sizes of actinolite and albite (left-hand site); grain-size histogram (relative frequency[%] vs. grain size [µm]) and phase fraction (%; pie diagram) of selected minerals (right-hand side). B) Contoured pole figures of selected crystallographic axes and poles; left—based on all pixels; right—based on one point per grain. MUD—Multiples of uniform distribution; l—lineation; f—foliation. C) Misorientation distribution plot (misorientation angle versus frequency [mrd=multiples of random density]) of selected minerals for uncorrelated grains (blue curves), and a theoretical random distribution (red curves). ODF—Orientation density functions.

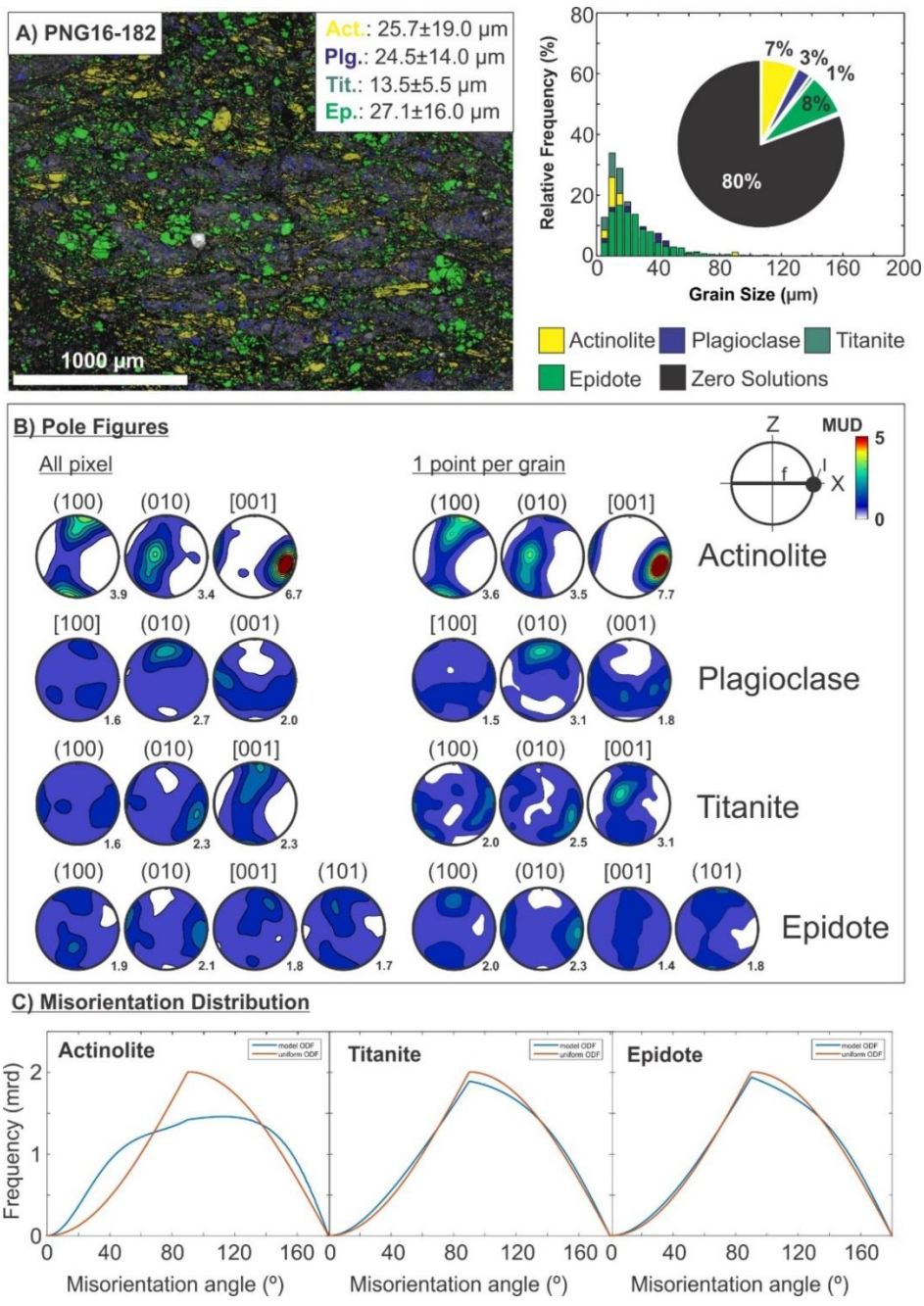

Figure S4.23. EBSD data for a non-mylonitic schist (~1.8 km south of the active Mai'iu fault trace; PNG16-182). A) EBSD-based phase map (2 µm step size) and average grain sizes of titanite, actinolite, epidote and albite (left-hand site); grain-size histogram (relative frequency[%] vs. grain size [µm]) and phase fraction (%; pie diagram) of selected minerals (right-hand side). B) Contoured pole figures of selected crystallographic axes and poles; left—based on all pixels; right—based on one point per grain. MUD—Multiples of uniform distribution; l—lineation; f—foliation. C) Misorientation distribution plot (misorientation angle versus frequency [mrd=multiples of random density]) of selected minerals for uncorrelated grains (blue curves), and a theoretical random distribution (red curves). ODF—Orientation density functions.

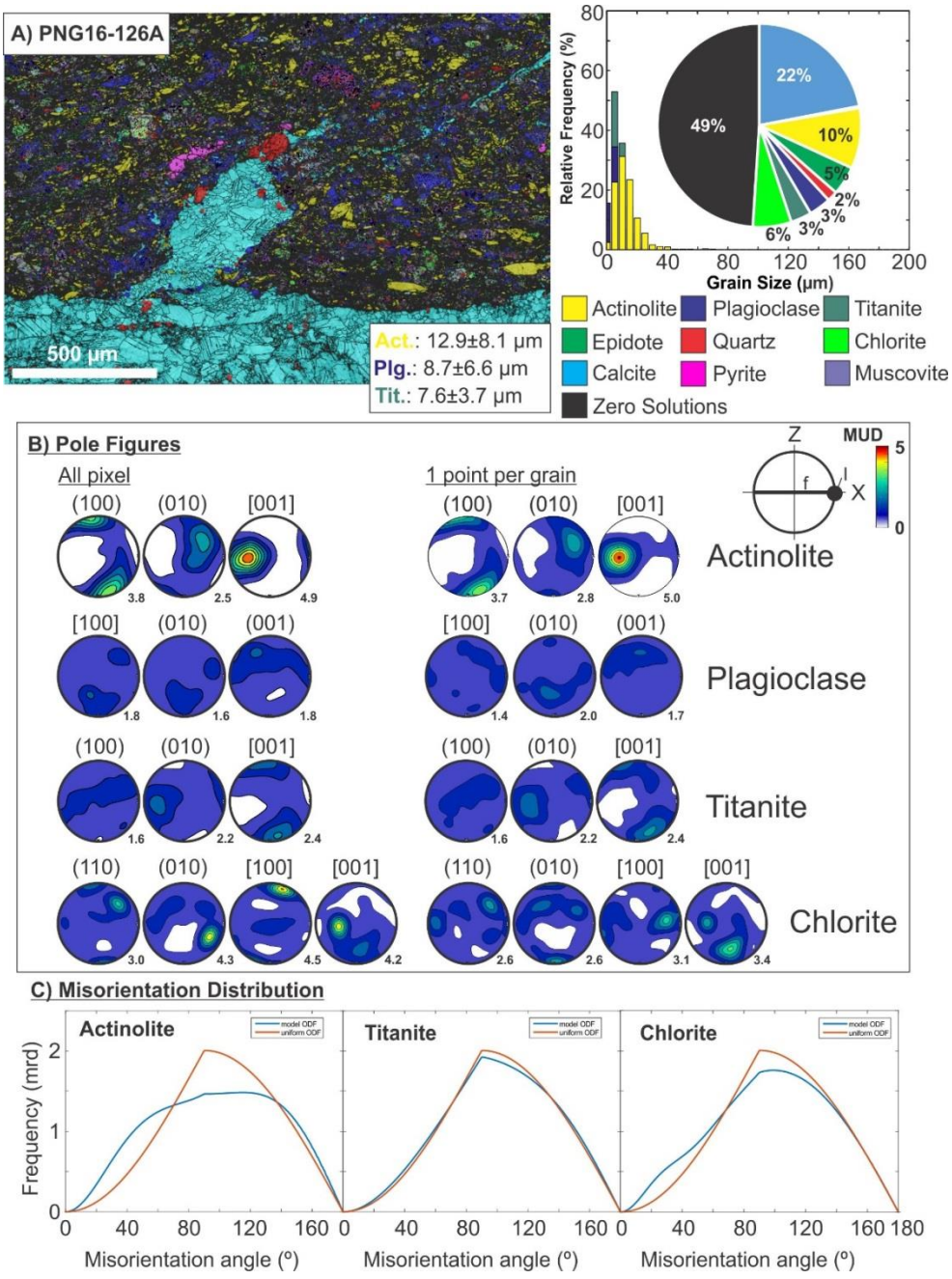

Figure S4.24. EBSD data for of a non-mylonitic schist (just south of active(?) Mai'iu fault trace, close to Gwoira fault; PNG16-126A). A) EBSD-based phase map (0.75 µm step size) and average grain sizes of titanite, actinolite and albite (left-hand site); grain-size histogram (relative frequency[%] vs. grain size [µm]) and phase fraction (%; pie diagram) of selected minerals (right-hand side). B) Contoured pole figures of selected crystallographic axes and poles; left—based on all pixels; right—based on one point per grain. MUD—Multiples of uniform distribution; l—lineation; f—foliation. C) Misorientation distribution plot (misorientation angle versus frequency [mrd=multiples of random density]) of selected minerals for uncorrelated grains (blue curves), and a theoretical random distribution (red curves). ODF—Orientation density functions.

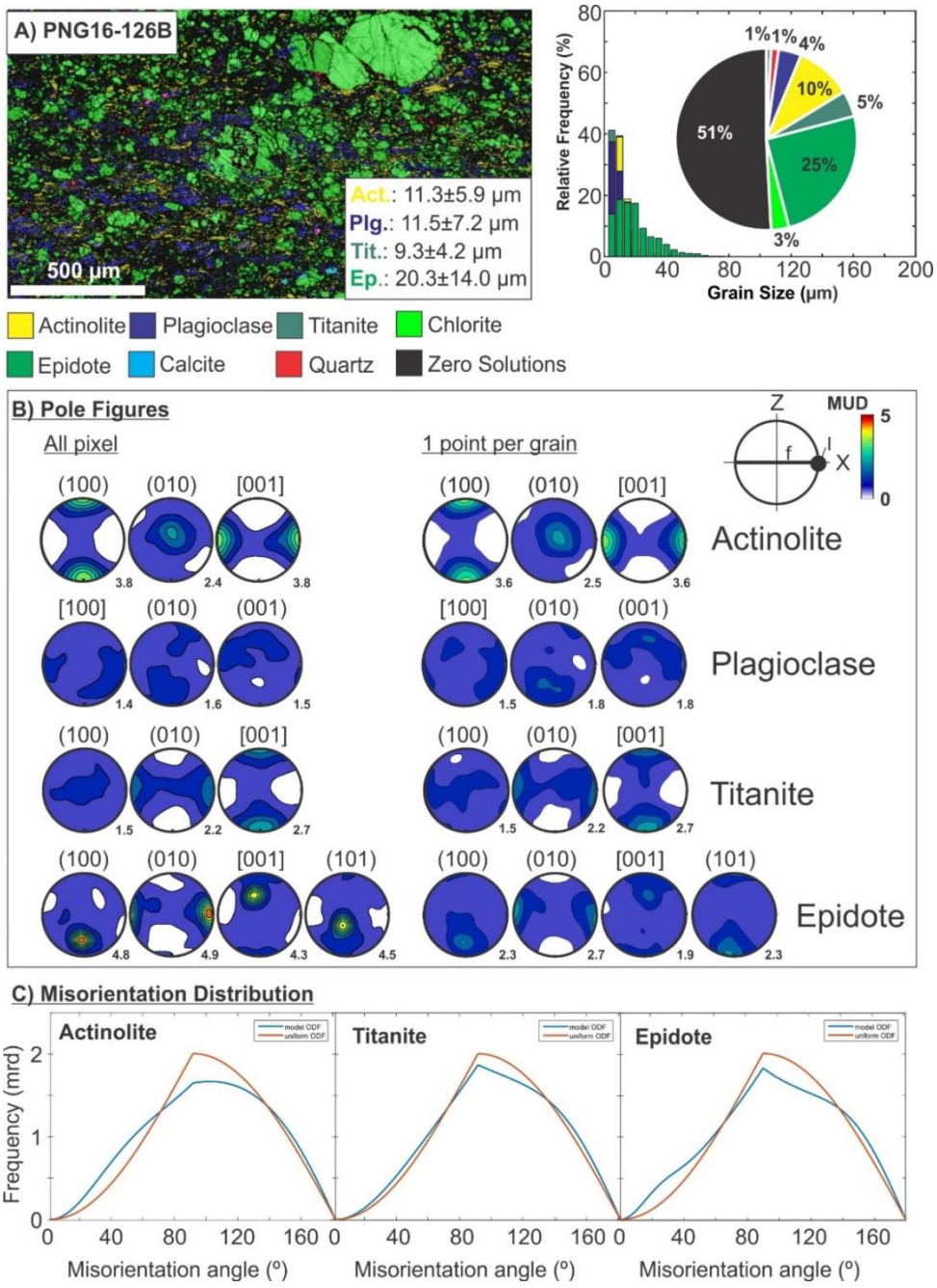

Figure S4.25. EBSD data for a non-mylonitic schist (just south of active(?) Mai'iu fault trace, close to Gwoira fault; PNG16-126B). A) EBSD-based phase map (1. 5 µm step size) and average grain sizes of titanite, actinolite, epidote and albite (left-hand site); grain-size histogram (relative frequency[%] vs. grain size [µm]) and phase fraction (%; pie diagram) of selected minerals (right-hand side). B) Contoured pole figures of selected crystallographic axes and poles; left—based on all pixels; right—based on one point per grain. MUD—Multiples of uniform distribution; l—lineation; f—foliation. C) Misorientation distribution plot (misorientation angle versus frequency [mrd=multiples of random density]) of selected minerals for uncorrelated grains (blue curves), and a theoretical random distribution (red curves). ODF—Orientation density functions.

Text S5. Temperature-Dependent Magnetic Susceptibility Experiment on Ultracataclasite

Temperature-dependent magnetic susceptibility experiments were conducted on the ultracataclasite sample PNG16-142D on a Bartington MS2 furnace system at the paleomagnetic laboratory at the School of Chemical and Physical Sciences, Victoria University of Wellington, in order to determine the Curie temperature(s) of the constituent ferromagnetic/ferrimagnetic phase(s) and therefore the magnetic mineralogy of this sample. We crushed the sample to a fine powder with mortar and pestle and extracted ~3.5 g of material for the sample holder. The extracted material was heated and cooled and its magnetic susceptibility was monitored throughout this process. The magnetic susceptibility was measured once the material in the sample holder reached 40°C, with measurements taken every 10°C. A peak temperature of 700°C was set for the experiment, before cooling back to 40°C. The results of this experiment are shown in Figure S5.1 and additional SEM back-scatter images and EDS analyses of the ultracataclasite (PNG16-142D) and magnetite-bearing veins and clasts in Figure S5.2, Figure S5.3, Figure S5.4 and Figure S5.5.

The thermomagnetic curves of the ultracataclasite sample at pressures of 1 atm are nearly reversible suggesting that up to temperatures of 700°C, no alteration occurred to the magnetic mineralogy during the experiment and none of the paramagnetic phases altered to ferromagnetic/ferromagnetic ones (Figure S5.1). During heating we observe an almost linear increase in magnetic susceptibility up to 380°C, above where the magnetic susceptibility shows a sharp linear increase up to 480°C. A peak with little variation of magnetic susceptibility is evident between 490 and 520°C just below the magnetite Curie point (Hopkinson peak). The susceptibility curve shows a strong drop from ~540°C down to 580°C and shallows to a Curie temperature of ~620–640°C close to the one of maghemite (TC≈645°C; Özdemir, 1990; Dunlop & Özdemir, 1997). The cooling run is below the heating run and shows a sharp increase in magnetic susceptibility from ~600°C to 500°C and reaches a plateau at ~480°C. The susceptibility drops again at ~450°C and the curve starts to flatten around ~300°C. We infer from this experiment that the principal magnetic mineral in the ultracataclasite is a stable (reversible heating and cooling curves), single domain (fine grained) magnetite. The observed Curie temperature above 580°C and below 645°C indicates cation deficient magnetite, slightly oxidized to maghemite (Özdemir & Banerjee, 1984; Dunlop & Özdemir, 1997).

SEM-EDS analyses show that opaque minerals occur as veins and coatings of and/or swirled into rounded fragments of ultracataclasite in the ultracataclasite matrix (Figure S5.2). Single, µm-sized opaque grains are rare in the ultracataclasites. Elemental analyses by EDS of the fine-grained opaque veins show high concentrations of Fe and small amounts of Ti, Si, K, Al and Mg (Figure S5.3, Figure S5.4). While the mineralogy of the opaque veins cannot be unambiguously identified using EDS, we infer that magnetite in the veins is too fine-grained (<1 µm diameter) to be imaged using that method; moreover, it has probably been in part oxidized to maghemite and intermingled with the ultra-fine grained, smectite-rich ultracataclasite matrix.

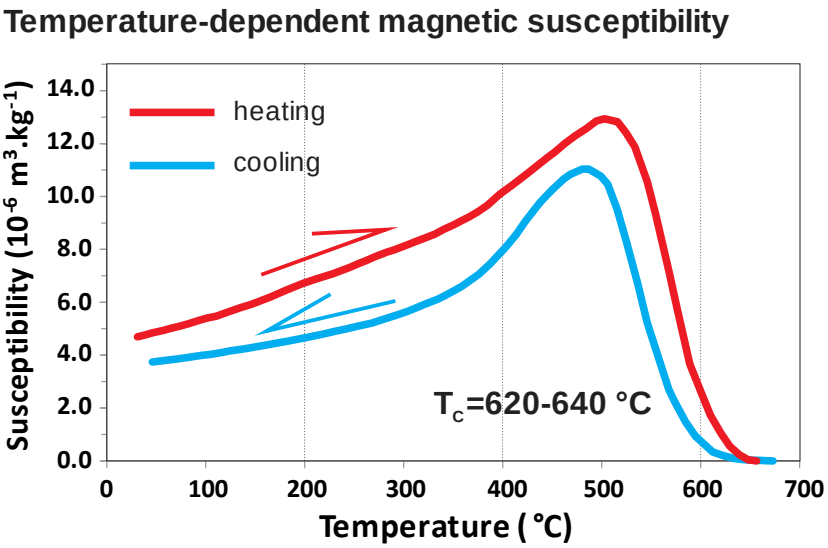

Figure S5.1. Curves of temperature versus magnetic susceptibility for sample PNG16-142D (ultracataclasite). The red and blue lines denote heating and cooling, respectively, from 40°C to 700°C and vice versa. T_C refers to the Curie temperature.

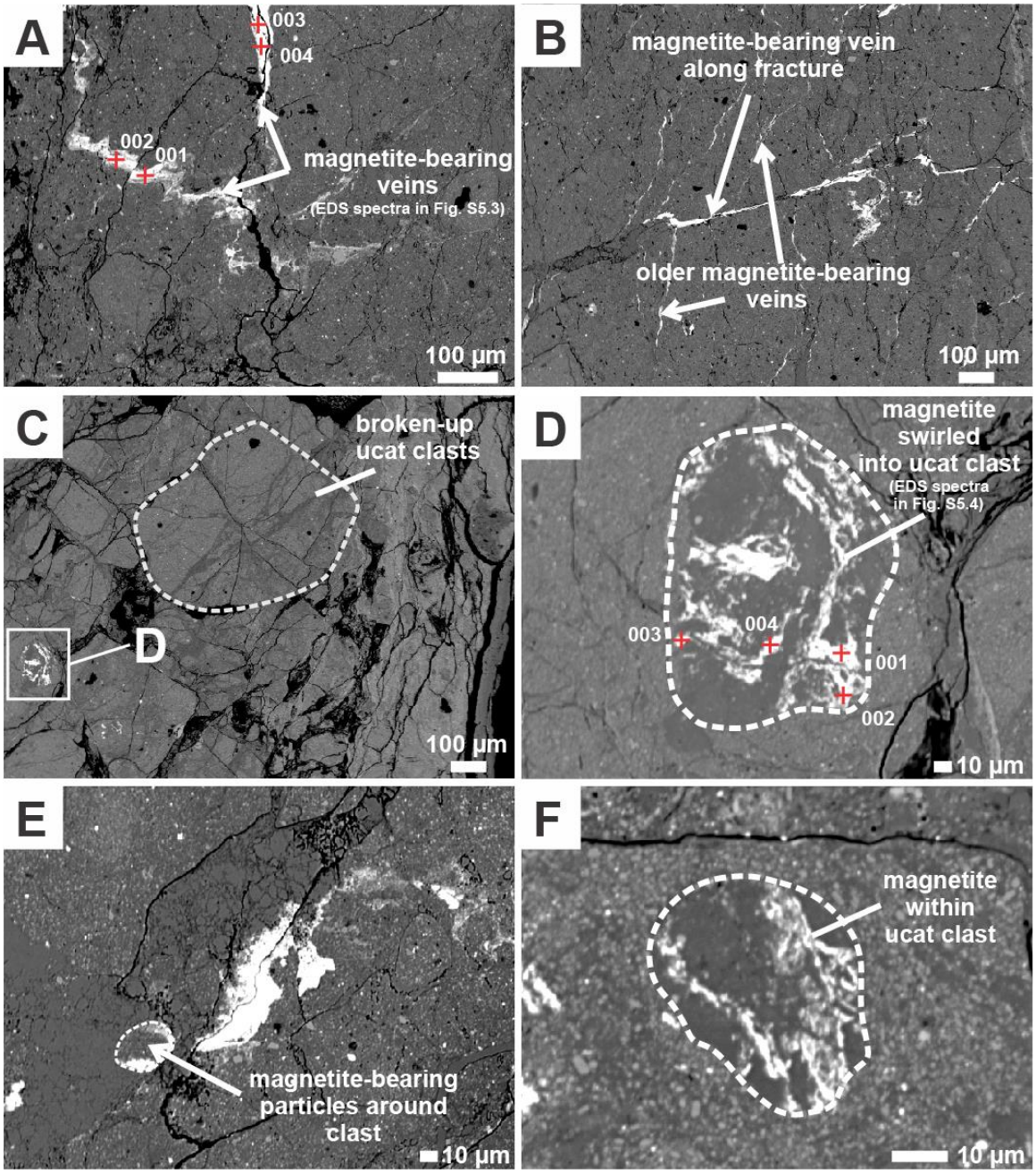

Figure S5.2. Backscatter electron images of magnetite-bearing veins and clasts in ultracataclasite (PNG16-142D). Magnetite appears white on the images. A) Magnetite in veins in association with fractured ultracataclasite and within the non-fractured ultracataclasite. Sample spots for the EDS analysis are indicated by red crosses. The spectra can be seen in Figure S5.3. B) Magnetite-bearing veins along fractures in the ultracataclasite. C) Broken ultracataclasites clast and an older, reworked clast with magnetite-bearing veins. D) Close up of C. This close-up shows the magnetite-bearing veins are folded ('swirled') within the clast. Sample spots for the EDS analysis in Figure S5.4 are indicated by red crosses. E) Magnetite-bearing particles surround a small clast.

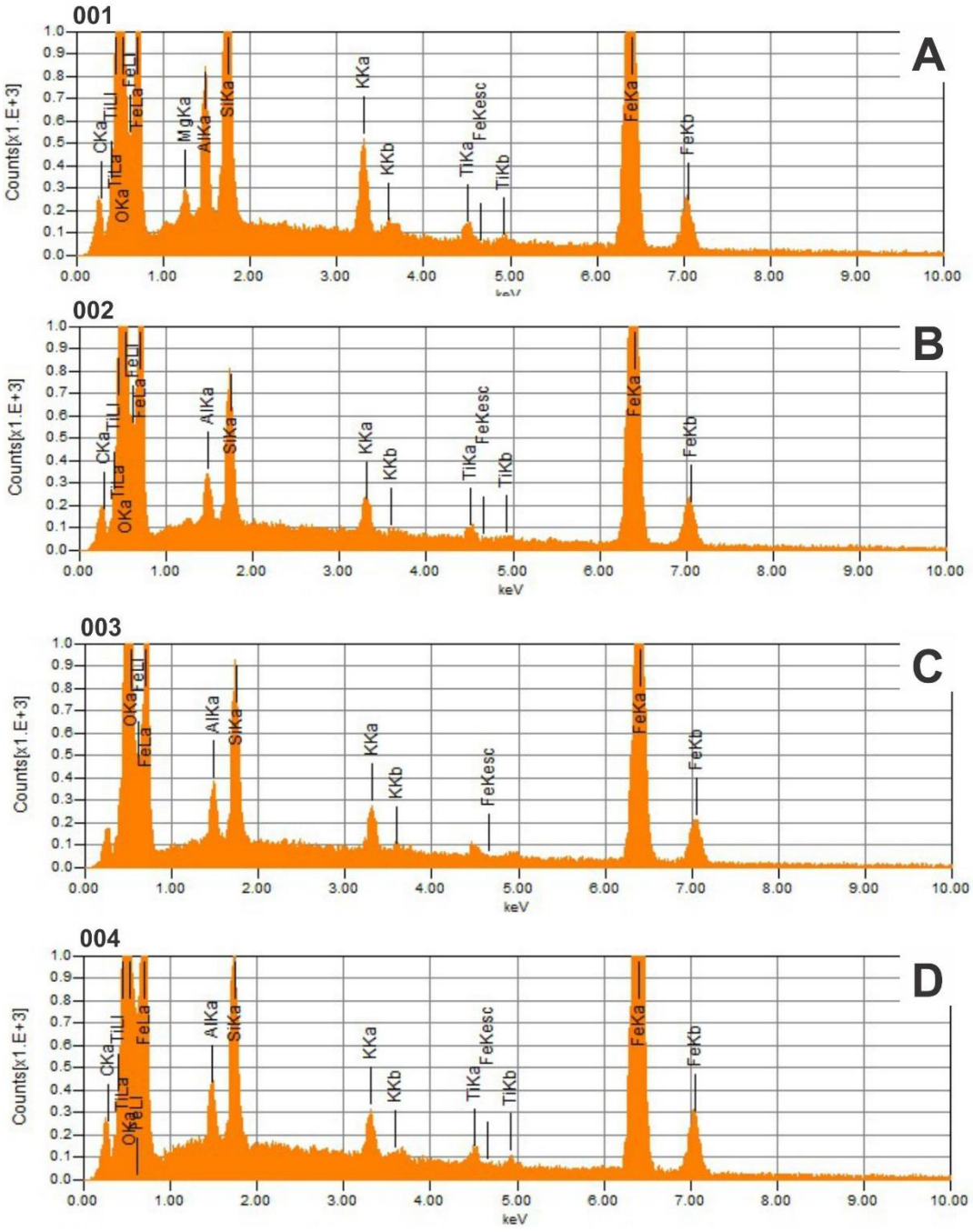

Figure S5.3. EDS-spectra of magnetite-bearing veins in Figure 5.2A (PNG16-142D).

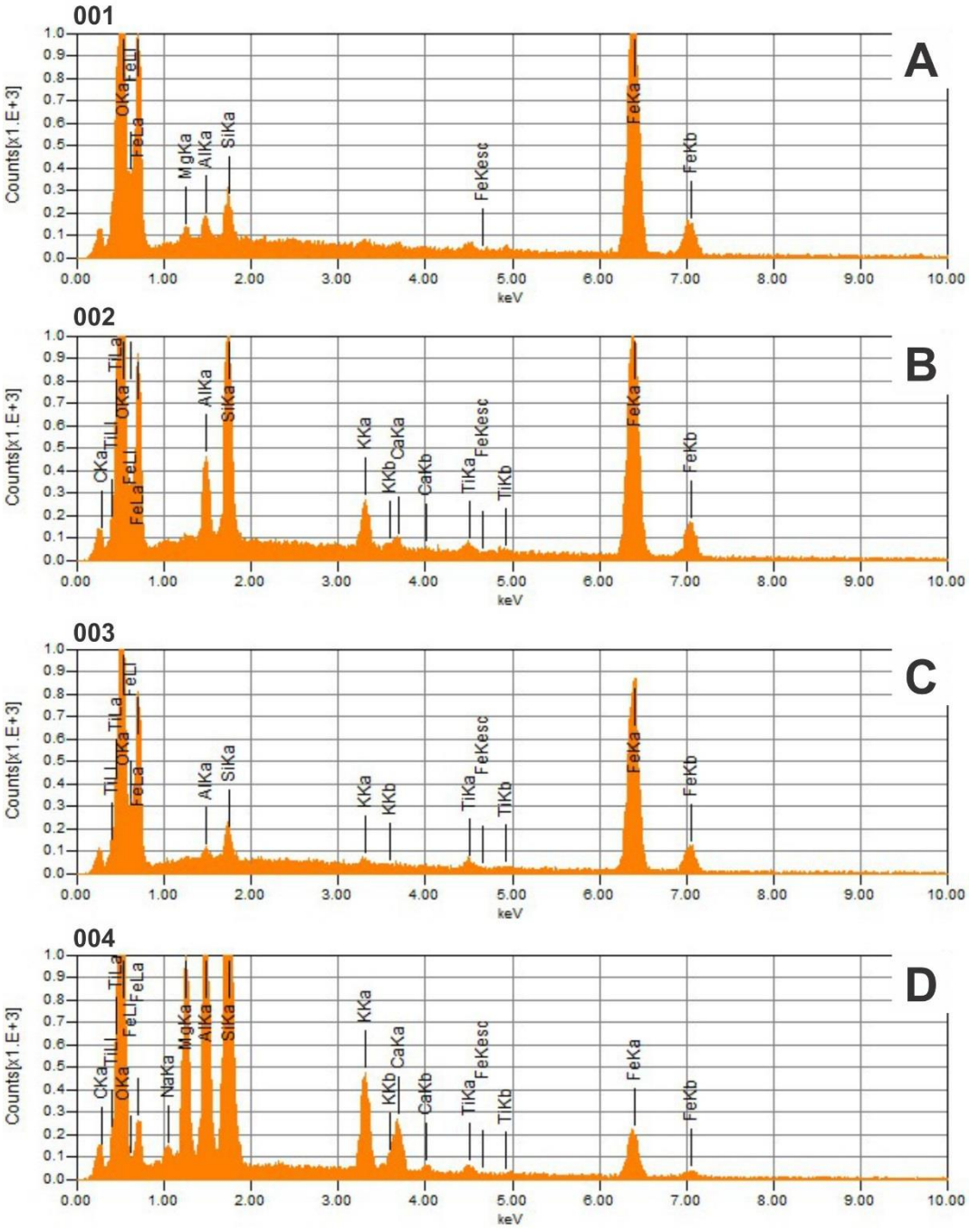

Figure S5.4. EDS-spectra of a magnetite-bearing clast in Figure S5.2D (PNG16-142D).

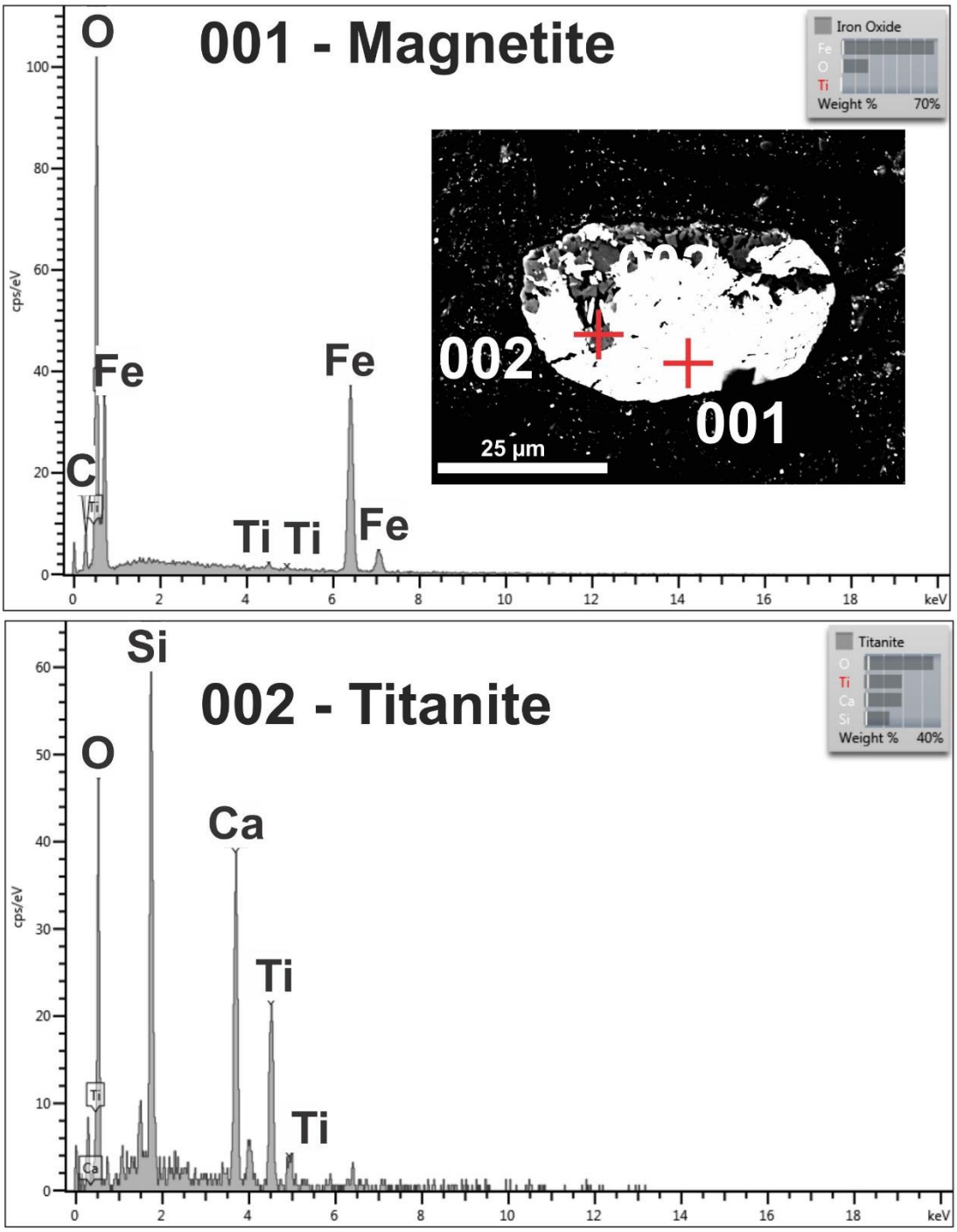

Figure S5.5. EDS analysis of a single magnetite grain in the ultracataclasite matrix (PNG16-142D).

Text S6. TEM Analysis of a Mirror-like Facet on Gabbroic Clast

The hangingwall contact atop the Mai'iu fault truncates cm- to dm-sized pebbles and cobbles in the Gwoira Conglomerate. We analyzed the mirror polish of one fault-truncated dolerite cobble with TEM in order to describe the composition, thickness and grain-size of the shiny, fault-truncated surface, and the origin of striation on these surfaces. A TEM foil was cut perpendicular to the shiny surface and was prepared using a FEI Quanta 3D FEG-SEM with focused ion beam (FIB) at University of Vienna, Department of Lithospheric Research. TEM used a JEOL 2011 STEM equipped with a double-tilt analytical holder and a Gatan MSC digital camera for imaging at the University of New Brunswick, Microscopy and Microanalysis Facility. The results of this method are presented in the main manuscript.

Text S7. Identification of Mineral Phases in Representative Mai'iu Fault Rocks using XRD

A collection of 15 fault rock samples of ultracataclasites, gouges and serpentinite schist were analysed with X-Ray Diffraction by Mark Raven at CSIRO Land and Water Flagship, Mineral Resources Flagship, at the Centre for Australian Forensic Soil Science (CAFSS), in Urrbrae, South Australia. For these, 1.5 g sub-samples were ground for 10 minutes in a McCrone micronizing mill under ethanol. The resulting slurries were oven dried at 60°C then thoroughly mixed in an agate mortar and pestle before being lightly pressed into aluminium sample holders for X-ray diffraction analysis. XRD patterns from the micronized materials showed variable hydration of the interlayer which causes problems with quantification. As the samples did not appear to contain any water soluble phases they were calcium saturated and the data re-analysed. XRD patterns were recorded with a PANalytical X'Pert Pro Multi-purpose Diffractometer using Fe filtered Co Ka radiation, auto divergence slit, 2° anti-scatter slit and fast X'Celerator Si strip detector. The diffraction patterns were recorded in steps of 0.016° 2 theta with a 0.4 second counting time per step, and logged to data files for analysis. Table S7.1 (below) lists the phases that were identified in each sample. These XRD-results are also published in Little et al. (2019).

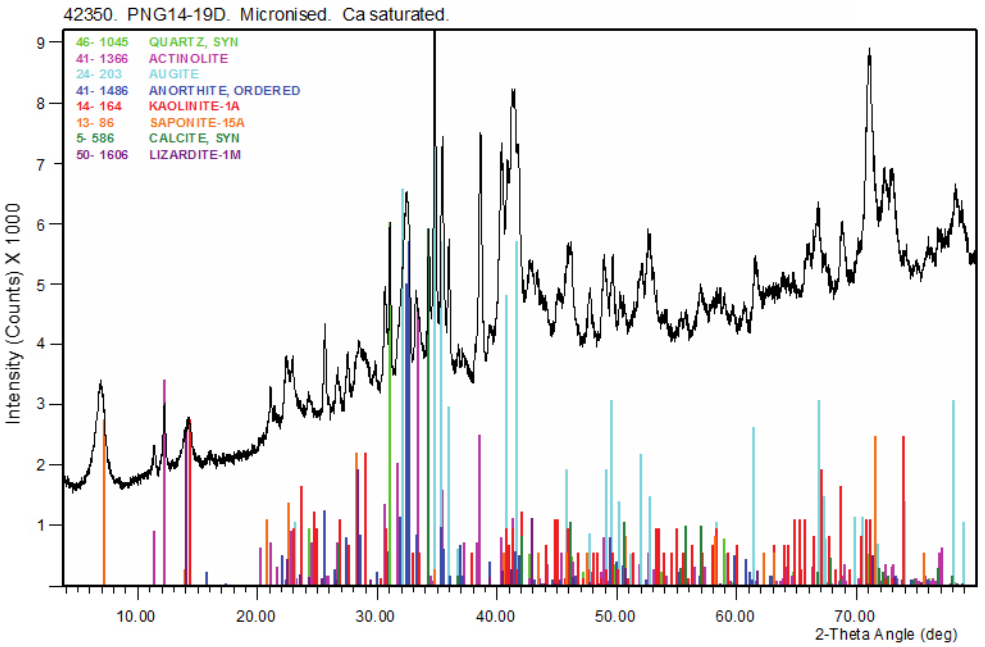
42350. PNG14-19D. Micronised. Ca saturated.
46- 1045 QUARTZ, SYN
41- 1366 ACTINOLITE
24- 203 AUGITE
41- 1486 ANORTHITE, ORDERED
14- 164 KAOLINITE-1A
13- 86 SAPONITE-15A
5- 586 CALCITE, SYN
50- 1606 LIZARDITE-1M
Intensity (Counts) X 1000
2-Theta Angle (deg)

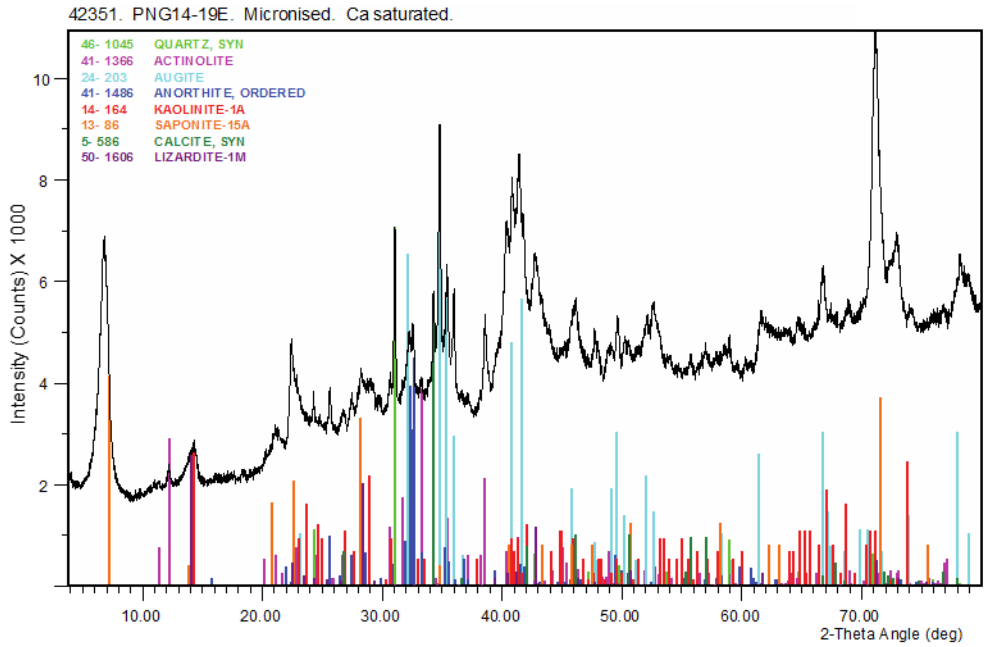
42351. PNG14-19E. Micronised. Ca saturated.
46- 1045 QUARTZ, SYN
41- 1366 ACTINOLITE
24- 203 AUGITE
41- 1486 ANORTHITE, ORDERED
14- 164 KAOLINITE-1A
13- 86 SAPONITE-15A
5- 586 CALCITE, SYN
50- 1606 LIZARDITE-1M
Intensity (Counts) X 1000
2-Theta Angle (deg)

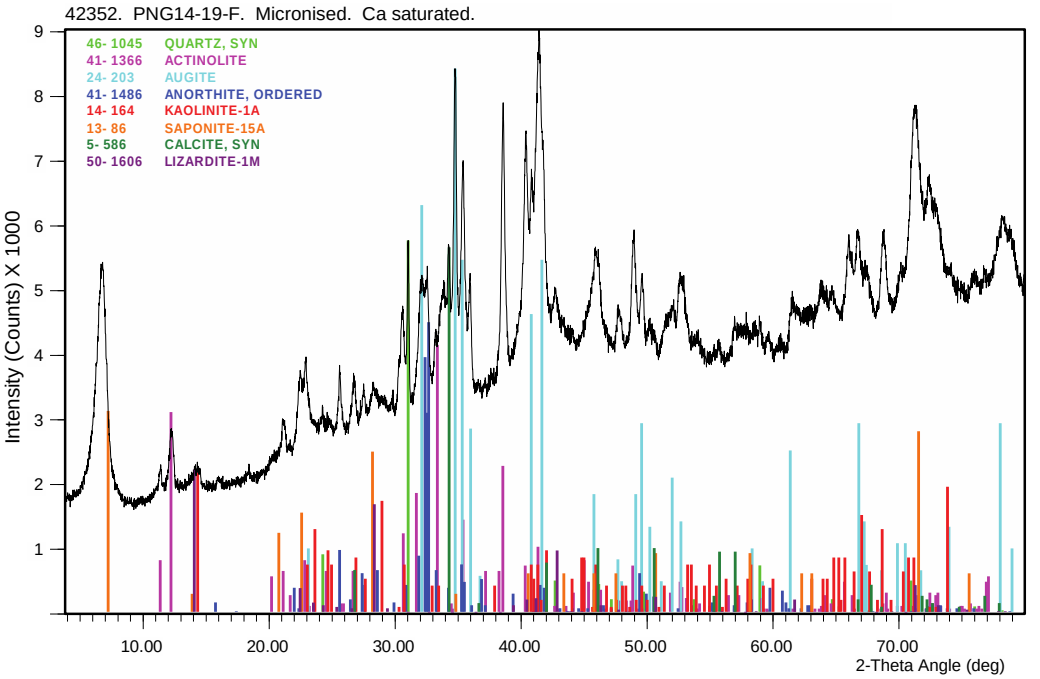
42352. PNG14-19-F. Micronised. Ca saturated.
46- 1045 QUARTZ, SYN
41- 1366 ACTINOLITE
24- 203 AUGITE
41- 1486 ANORTHITE, ORDERED
14- 164 KAOLINITE-1A
13- 86 SAPONITE-15A
5- 586 CALCITE, SYN
50- 1606 LIZARDITE-1M
Intensity (Counts) X 1000
2-Theta Angle (deg)

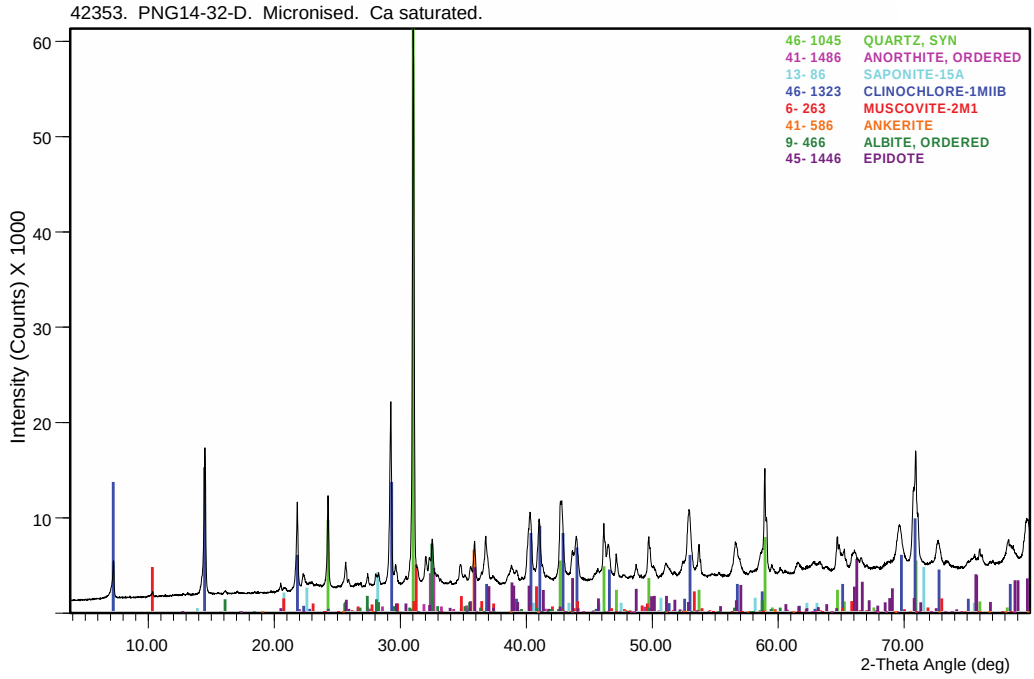
42353. PNG14-32-D. Micronised. Ca saturated.
46- 1045 QUARTZ, SYN
41- 1486 ANORTHITE, ORDERED
13- 86 SAPONITE-15A
46- 1323 CLINOCHLORE-1MIIB
6- 263 MUSCOVITE-2M1
41- 586 ANKERITE
9- 466 ALBITE, ORDERED
45- 1446 EPIDOTE
Intensity (Counts) X 1000
2-Theta Angle (deg)

42354. PNG14-32-E Green. Micronised. Ca saturated.

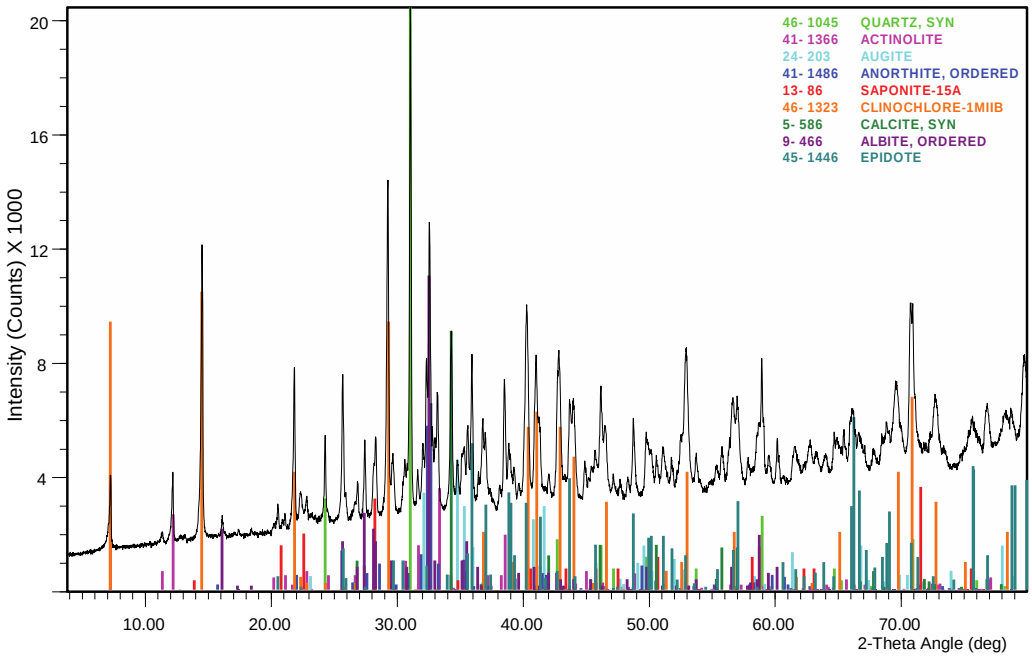

42355. PNG14-32-E Red. Micronised. Ca saturated.

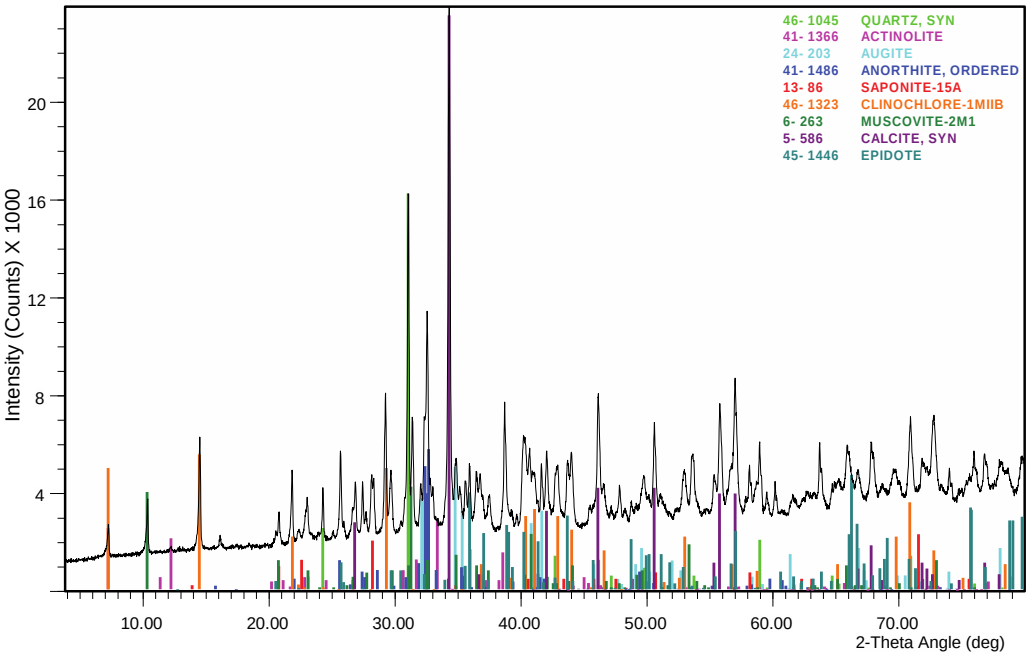

42356. PNG14-32-F. Micronised. Ca saturated.

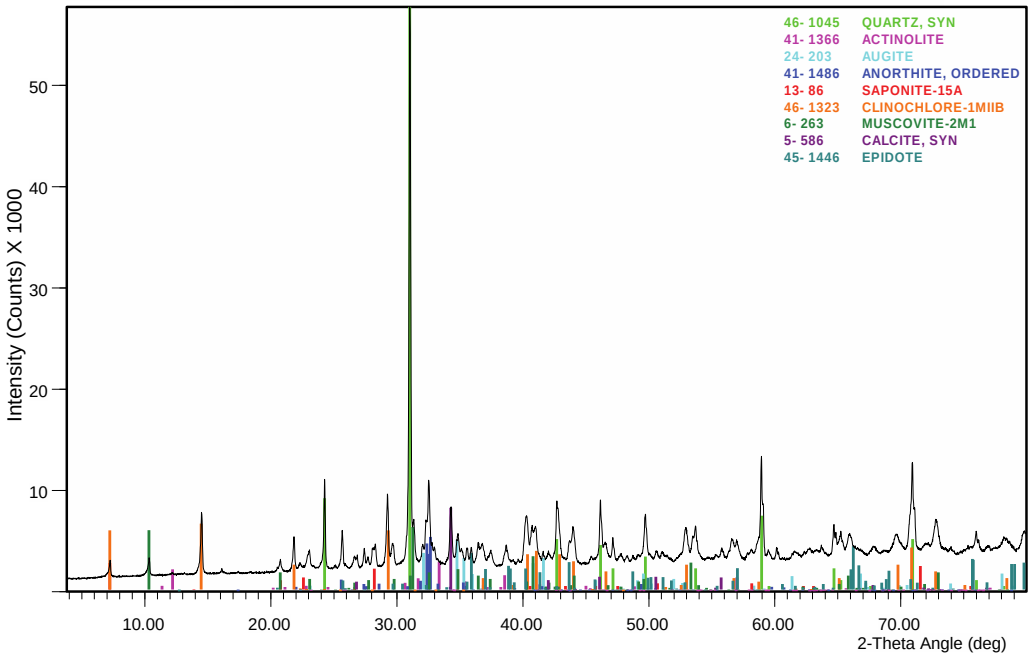

42357. PNG14-33-A. Micronised. Ca saturated.

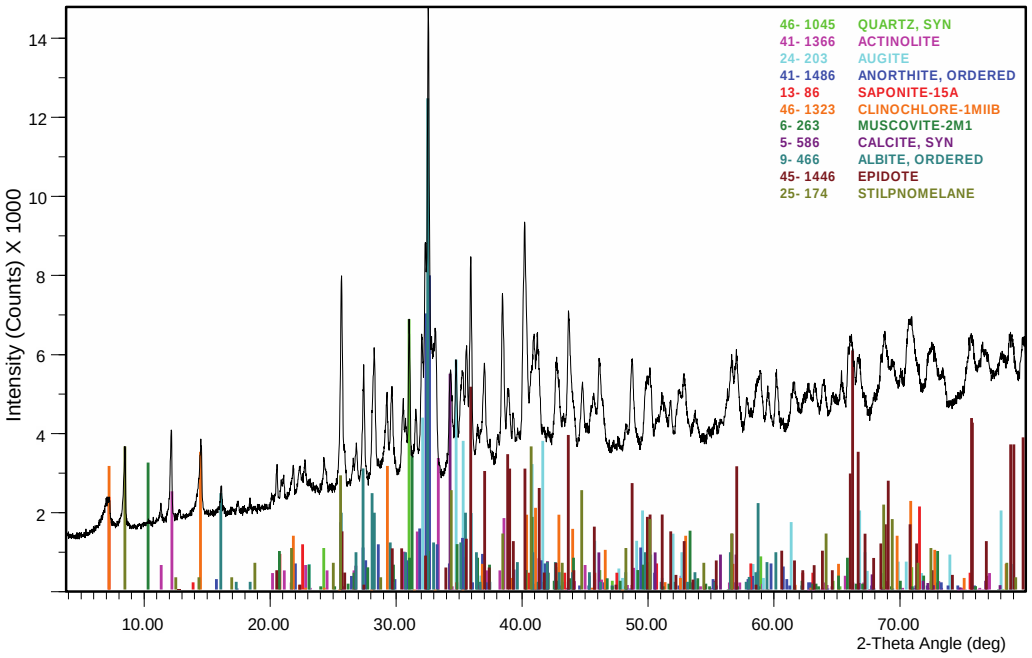

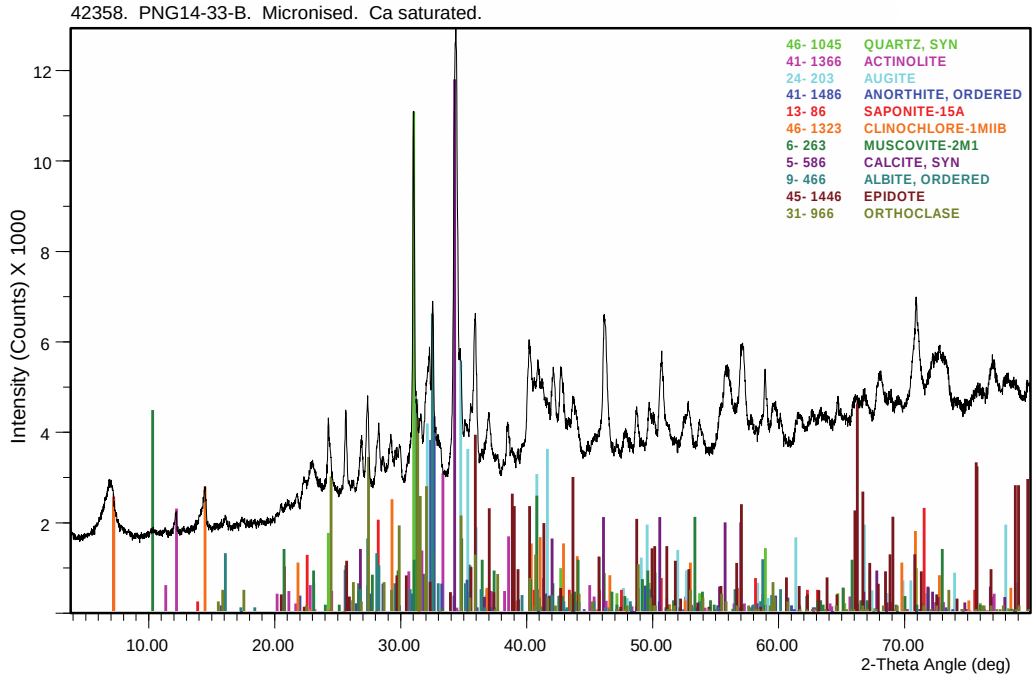
42358. PNG14-33-B. Micronised. Ca saturated.
46- 1045 QUARTZ, SYN
41- 1366 ACTINOLITE
24- 203 AUGITE
41- 1486 ANORTHITE, ORDERED
13- 86 SAPONITE-15A
46- 1323 CLINOCHLORE-1MIIB
6- 263 MUSCOVITE-2M1
5- 586 CALCITE, SYN
9- 466 ALBITE, ORDERED
45- 1446 EPIDOTE
31- 966 ORTHOCLASE
Intensity (Counts) X 1000
2-Theta Angle (deg)

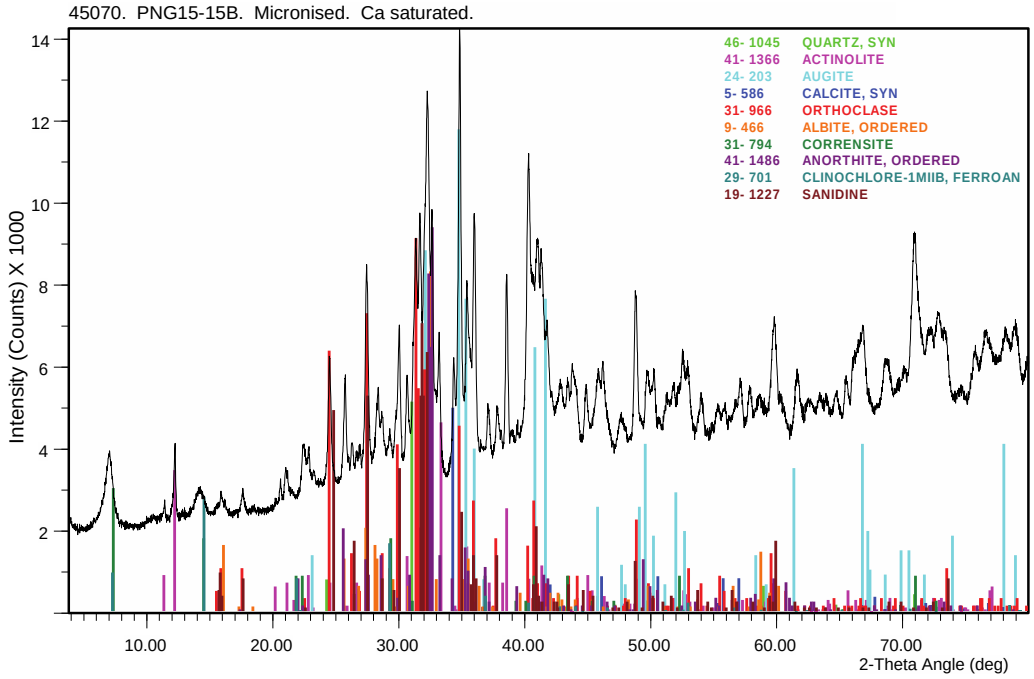
45070. PNG15-15B. Micronised. Ca saturated.
46- 1045 QUARTZ, SYN
41- 1366 ACTINOLITE
24- 203 AUGITE
5- 586 CALCITE, SYN
31- 966 ORTHOCLASE
9- 466 ALBITE, ORDERED
31- 794 CORRENSITE
41- 1486 ANORTHITE, ORDERED
29- 701 CLINOCHLORE-1MIIB, FERROAN
19- 1227 SANIDINE
Intensity (Counts) X 1000
2-Theta Angle (deg)

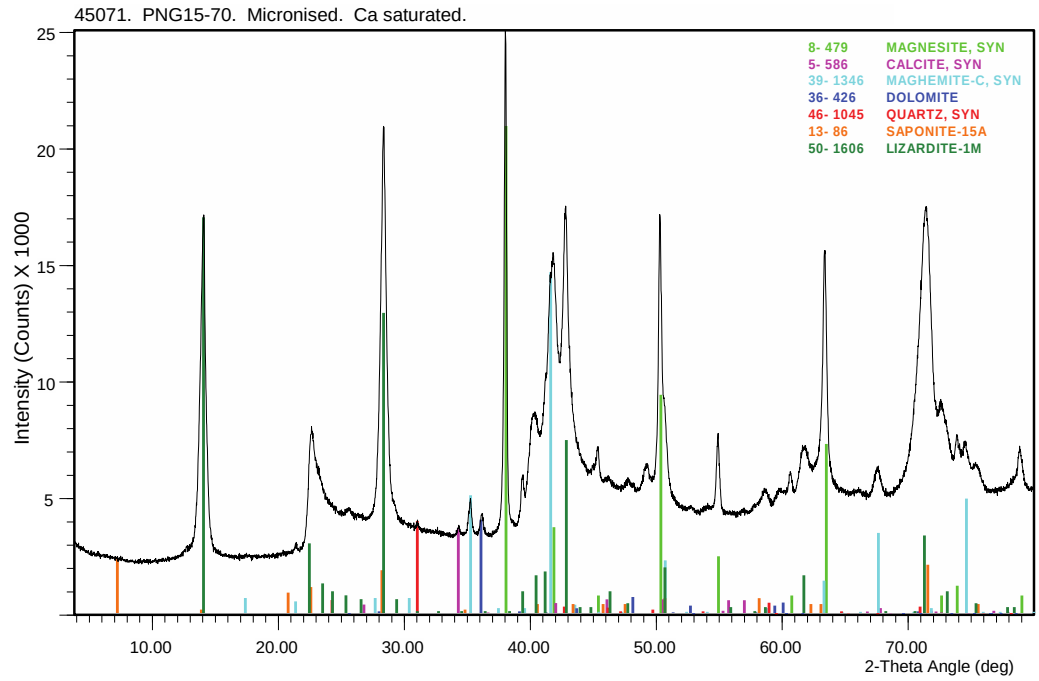
45071. PNG15-70. Micronised. Ca saturated.
8- 479 MAGNESITE, SYN
5- 586 CALCITE, SYN
39- 1346 MAGHEMITE-C, SYN
36- 426 DOLOMITE
46- 1045 QUARTZ, SYN
13- 86 SAPONITE-15A
50- 1606 LIZARDITE-1M
Intensity (Counts) X 1000
2-Theta Angle (deg)

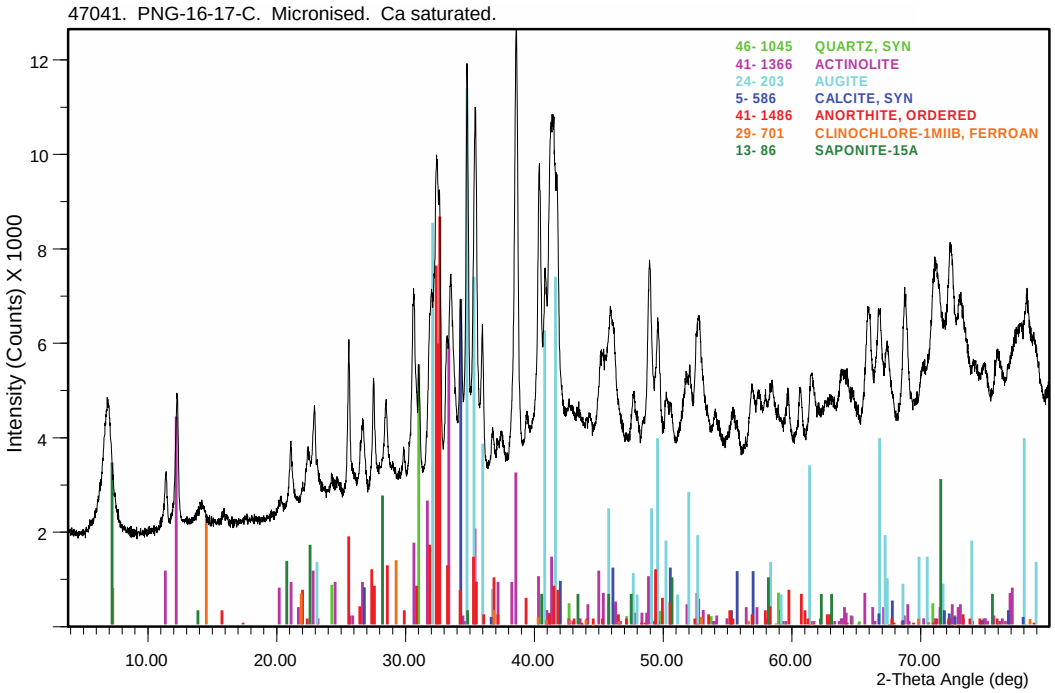
47041. PNG-16-17-C. Micronised. Ca saturated.
46- 1045 QUARTZ, SYN
41- 1366 ACTINOLITE
24- 203 AUGITE
5- 586 CALCITE, SYN
41- 1486 ANORTHITE, ORDERED
29- 701 CLINOCHLORE-1MIIB, FERROAN
13- 86 SAPONITE-15A
Intensity (Counts) X 1000
2-Theta Angle (deg)

47042. PNG-16-30-B. Micronised. Ca saturated.

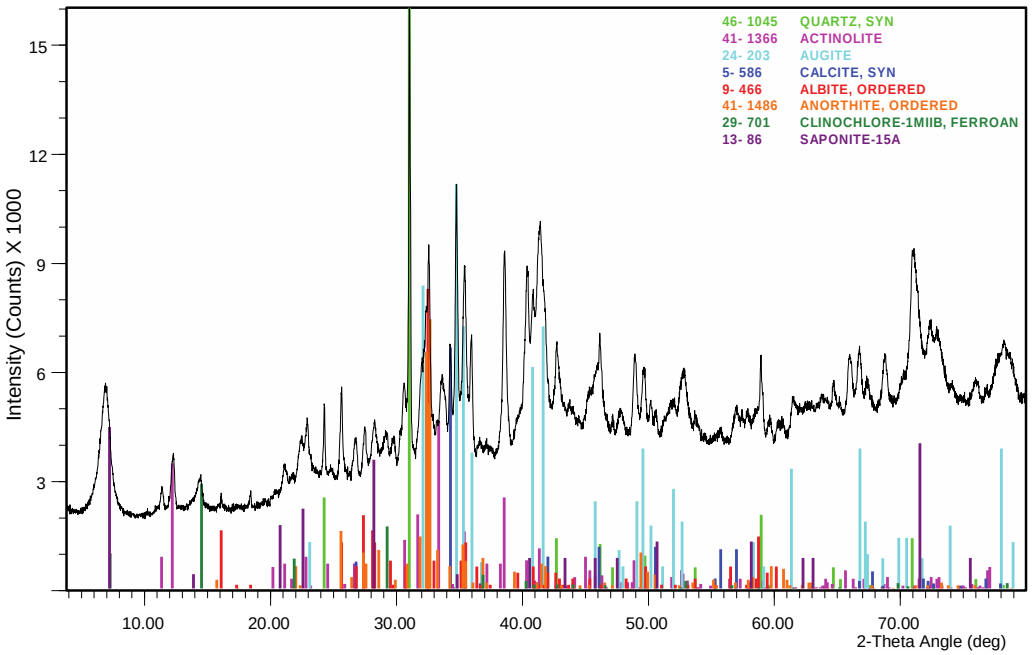

47043. PNG-16-108-G. Micronised. Ca saturated.

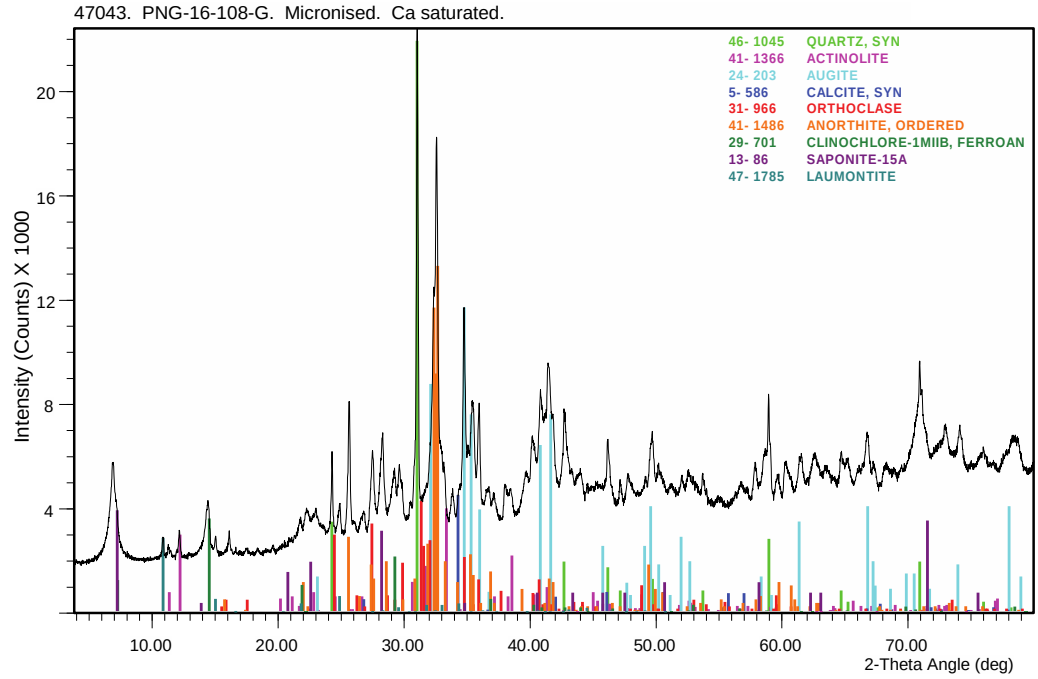

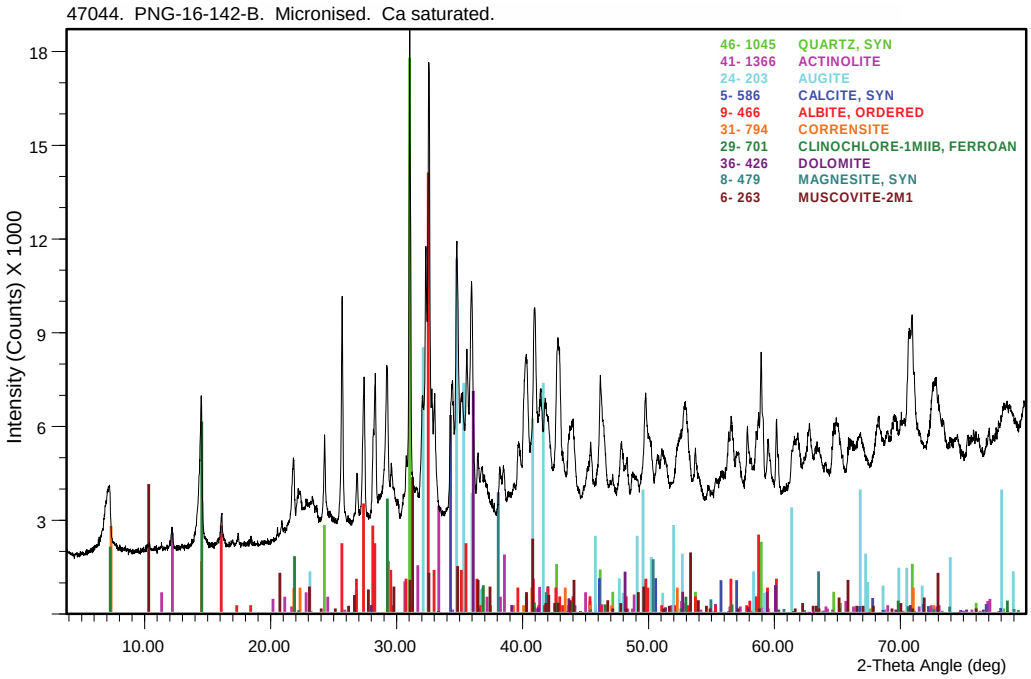

Figure S7.1. Whole rock, Ca-saturated X-ray diffraction patterns.

CSIRO ID	Field Sample No.	Fault Rock Unit	Fault	Degrees South (WGS84) Latitude	Degrees East (WGS84) Longitude
42350	PNG-14-19-D	ultracataclasite	inactive Mai'iu F.	149.44082	-9.82862
42351	PNG14-19-E	gouge	inactive Mai'iu F.	149.44082	-9.82862
42352	PNG-14-19-F	gouge	inactive Mai'iu F.	149.44082	-9.82862
42353	PNG-14-32-D	gouge	Biniguni Splay F.	149.38230	-9.67883
42354	PNG-14-32-E-g	gouge	Biniguni Splay F.	149.38230	-9.67883
42355	PNG-14-32-E-r	gouge	Biniguni Splay F.	149.38230	-9.67883
42356	PNG-14-32-F	gouge	Biniguni Splay F.	149.38230	-9.67883
42357	PNG-14-33-A	gouge	active Mai'iu F.	149.35904	-9.67726
42358	PNG-14-33-B	gouge	active Mai'iu F.	149.35904	-9.67726
45070	PNG-15-50-B	ultracataclasite	active Mai'iu F.	149.28669	-9.67778
45071	PNG-15-70	serpentininite	active Mai'iu F.	149.61246	-9.82863
47041	PNG-16-17-C	ultracataclasite	inactive Mai'iu F.	149.44028	-9.82967
47042	PNG-16-30-B	gouge	inactive Mai'iu F.	149.44059	-9.82499
47043	PNG-16-108-G	gouge	active Gwoira F.	149.46712	-9.77150
47044	PNG-16-142-B	gouge	active Mai'iu F.	149.35913	-9.67729

CSIRO ID	Notes
42350	Near lower transition into foliated cataclasite unit
42351	Upper of two gouge layers. Light grey, 1.5 cm thick
42352	Lower of of two gouge layers. Dark grey, 17 cm thick
42353	Porphyroclastic gouge layer 1m thick. Greenish grey.
42354	Green-colored gouge in variegated gouge layer >1 m thick
42355	Maroon-colored gouge in variegated gouge layer >1 m thick
42356	White-colored gouge in variegated gouge layer >1 m thick
42357	Lower of two gouge layers. Green, 10 cm thick.
42358	Upper of two gouge layers. Grey, 5 cm thick.
45070	Exhumed pavement surface at base of scarp
45071	Serpentinite fault slice structurally atop exhumed Mai'iu fault near Mt Masasoru
47041	Same fault outcrop as location PNG-14-19
47042	Upper gouge layer. Grey, 2 cm thick.
47043	Collected 21 cm below PDS
47044	Upper of two gouge layers. Purple-grey, 5 cm thick. Same as PNG-14-33-B

CSIRO ID	Whole Rock Mineralogy
42350	Corrensite/Saponite, Augite, Amphibole, Plagioclase, Kaolin, Calcite, Quartz
42351	Corrensite/Saponite, Augite, Amphibole, Plagioclase, Kaolin, Calcite, Quartz
42352	Corrensite/Saponite, Augite, Amphibole, Plagioclase, Kaolin, Calcite, Quartz
42353	Chlorite, Quartz, Epidote, Plagioclase, Mica, Titanite
42354	Chlorite, Plagioclase, Amphibole, Epidote, Quartz, Calcite, Titanite
42355	Calcite, Mica, Plagioclase, Epidote, Chlorite, Quartz, Titanite, Hematite, Amphibole
42356	Quartz, Chlorite, Mica, Plagioclase, Calcite, Epidote, Titanite, Amphibole, Hematite
42357	Plagioclase, Epidote, Amphibole, Corrensite/Saponite, Chlorite, Stilpnomelane, Titanite, Calcite, Quartz, K-feldspar
42358	Corrensite/Saponite, Calcite, Montmorillonite, Plagioclase, Epidote, K-feldspar, Amphibole, Quartz, Dolomite/Ankerite, Chlorite, Mica
45070	Corrensite, K-feldspar, Plagioclase, Amphibole, Augite, Chlorite, Calcite, Quartz
45071	Serpentine (Lizardite), Magnesite, Saponite, Quartz, Calcite, Dolomite/Ankerite, Maghemite
47041	Saponite, Amphibole, Plagioclase, Augite, Calcite, Chlorite, Quartz
47042	Saponite, Amphibole, Plagioclase, Augite, Calcite, Chlorite, Quartz
47043	Saponite, Amphibole, Plagioclase, Augite, Quartz, Chlorite, K-feldspar, Laumontite, Calcite, Magnesite
47044	Saponite, Plagioclase, Augite, Amphibole, Chlorite/Corrensite, Dolomite/Ankerite, Quartz, Calcite, Mica, Magnesite

Table S7.1. Mineral Phases in Mai'iu fault rocks determined by X-Ray Diffraction.

Text S8. Bulk Whole rock Major Element Compositions of Mafic Fault Rocks Using XRF

Whole rock major element concentrations (Table S8.1) were determined based on X-ray fluorescence (XRF) spectrometry with a SPECTRO X-LAB 2000 at the Department of Earth & Ocean Sciences, University of Waikato, on fused glass disks cast using a 10:1 flux ratio in lithium borate flux. Trace element concentrations were measured with a Thermo-Scientific Element2 sector-field inductively coupled plasma mass spectrometry (ICP-MS) at the School of Geography, Environment and Earth Sciences, Victoria University Wellington. A gravimetric multi-element synthetic mixture was employed to calibrate the unknowns and to monitor for drift. The accuracy of the unknowns was determined with a secondary reference material (AGV-2).

Sample#	PNG-16-17_2D	PNG-16-17z	PNG-14-19e	PNG-14-19F
Formation	Goropu Metabasalt	Goropu Metabasalt	Goropu Metabasalt	Goropu Metabasalt
Sequence	Non-Mylonitic	Mafic Mylonite	Gouge	Gouge
wt.%				
SiO2	45.56	48.84	42.93	43.80
TiO2	1.33	1.63	0.86	0.81
Al2O3	14.74	12.32	11.45	11.16
Fe2O3	11.45	11.95	11.23	10.84
MnO	0.19	0.22	0.22	0.23
MgO	7.60	6.75	16.80	16.58
CaO	11.49	9.37	7.54	8.40
Na2O	2.08	2.96	0.94	0.90
K2O	0.14	0.04	0.08	0.03
P2O5	0.14	0.19	0.11	0.11
SO3	0.07	0.17	0.07	0.13
SrO (Sr - PPM)	82.00	271.00	53.00	71.00
BaO (Ba - PPM)	94.00	81.00	42.00	45.00
CO2 (%)	4.24	4.91	7.04	6.27
Total (%)	99.04	99.38	99.28	99.26
ppm				
Cr	309.38	200.54	1303.54	1346.79
Ni	67.49	51.19	709.16	758.27
Cs	0.05	0.03	0.17	0.10
Ba	17.30	21.11	23.80	16.47
Rb	2.86	0.27	1.69	0.48
Sr	140.70	267.79	96.00	112.01
Pb	0.28	1.01	2.08	2.28
Th	0.21	0.56	0.79	0.75
U	0.10	0.18	0.21	0.20
Zr	162.60	103.73	127.05	123.87
Nb	4.80	6.65	2.35	2.27
Hf	2.16	2.81	1.72	1.67
Ta	0.45	0.63	0.28	0.26
Y	22.08	23.65	17.23	17.11
V	308.84	290.29	207.72	197.23
Sc	41.95	33.89	29.47	29.54
Co	51.98	36.24	72.64	74.47
Cu	107.17	99.43	93.24	95.15
Zn	92.07	172.19	74.86	76.38
Ga	19.17	16.57	13.00	12.10
La	4.67	6.19	4.64	4.54
Ce	11.89	15.77	10.93	10.66
Pr	1.79	2.34	1.54	1.51
Nd	9.34	11.42	7.71	7.50
Sm	3.04	3.36	2.28	2.32
Eu	2.29	1.26	1.59	1.57
Gd	3.66	4.03	2.75	2.77
Tb	0.68	0.79	0.52	0.52
Dy	4.41	4.89	3.42	3.38
Ho	0.91	1.02	0.72	0.71
Er	2.67	2.98	2.12	2.14
Tm	0.38	0.42	0.31	0.31
Yb	2.34	2.67	1.93	1.94
Lu	0.37	0.41	0.29	0.30
Au	0.22	0.36	0.13	0.16

Table S8.1. Chemical analyses of Mai'iu fault rock samples comprising a non-mylonitic, almost undeformed Goropu Metabasalt, a mylonite and two gouge samples. Note, the increase in Cr and Ni in the gouge sample relative to the other samples (highlighted in yellow). Also compare with Smith (2013).

Text S9. Chlorite and Albite Compositions Using EPMA

Wavelength dispersive analysis of chlorite and albite was carried out on a JEOL electron microprobe at the School of Geography, Environmental and Earth Science, Victoria University of Wellington. We used an acceleration voltage of 15 kV and a sample current of 12 nA. Synthetic and natural mineral standards were used for calibration comprising the elements Si, Al, Mg, Mn, Fe, Zn, Ni, Cr, Na, K and Ca for chlorite and Si, Al, Mg, Mn, Fe, Ni, Ti, Na, K and Ca for plagioclase (albite). Errors in the raw data were reduced by ZAF correction. The results from this analysis can be found in Table S9.1 ('Albite_EPMA_Data.xlsx') and Table S9.2 ('Chlorite_EPMA_data.xlsx') that are uploaded as separate files. The former shows the results for albite; and latter shows the results of all analysed chlorite grains in the mafic mylonites, foliated cataclasites and chlorite veins.

Table S9.1 (Albite_EPMA_Data.xlsx). Feldspar compositions in mafic mylonites and foliated cataclasites.

Table S9.2 (Chlorite_EPMA_data.xlsx). Chlorite compositions, calculated temperatures and proportions of chlorite to swelling component (X) in analysed mylonite, foliated cataclasites and chlorite veins.